DESIGN AND DEVELOPMENT OF EFFICIENT SOLID-STATE DYE-SENSITIZED SOLAR CELLS

By

Wen Yuan

A DISSERTATION

Submitted to
Michigan State University
in partial fulfillment of the requirements
for the degree of

Chemistry – Doctor of Philosophy

2013

ABSTRACT

DESIGN AND DEVELOPMENT OF EFFICIENT SOLID-STATE DYE-SENSITIZED SOLAR CELLS

By

Wen Yuan

Organic photovoltaic cell is the most promising one in the third generation solar cell. Considering the materials used for fabricating devices, it generally can be classified as two sorts. One is called full organic solar cell, which is all made by organic or polymeric molecules. The examples of this type of solar cell includes bulk heterojunction solar cell (BHJ solar cell). Another one is organic/inorganic hybrid solar cell, and most of them are composed of organic-inorganic blends. For instance, solid state dye sensitized solar cell (ss-DSSC) is made by porous dye-coated inorganic semiconductor and then infiltrating organic conductor into it. One of the most commonly-used organic hole conductor is spiro-MeOTAD (2, 2', 7, 7' –tetrakis (N, N-di-p-methoxyphenylamine) 9, 9'-spirobifluorene). The ss-DSSC made by spiro-MeOTAD already reached an average power conversion efficiency around 3-4% and a record efficiency of 7.2% from Gratzel's group. However it is still below a desired level for manufacturing usage.

This dissertation presents three approaches to optimize the ss-DSSC: Increasing fill factor in ss-DSSC, enhancement of light harvesting and

In the first part, we first provide an overview of doping in organic or polymeric materials. Subsequently, we discuss the prior literature on p-dopants and additives incorporated into ss-DSSCs. Finally we present our data that suggests the primary role of Lithium salts is to stabilize the oxidized state of the hole conductor

In the second part, we use surface-initiated polymerization to anchor hole conducting polymers onto silica nanoparticles. We argue that the formation of silica/polymer composites serve as a light scattering layer on the top of photoanode, raising the short circuit current by 26% over conventional spiro-MeOTAD ss-DSSCs

Finally, a simple strategy is presented which effectively increases the pore-filling fraction of spiro-MeOTAD into photoanode. Heating the cell during the fabrication process lowers the electrolyte viscosity and surface tension, enabling an 86% increase in cell efficiency over cells without heat treatment.

To my family

ACKNOWLEDGEMENTS

I would like to sincerely thank my advisor, Dr. Gregory Baker for his guidance, attention, and encouragement in all these years. I would also like to thank my committee members, Dr. William Wulff, Dr. Keith Promislow, Dr. Mitch Smith, Dr. Greg Swain and Dr. Larry Drzal for their guidance and helpful suggestions.

My thanks go to all previous and current Baker group members: Qin, Sampa, Tom, Hui, Gina, Quanxuan, Heyi, Yiding, Zhe, Greg, Salinda and all my friends at Michigan State University. Thanks to Dan Holmes, Kathy Severin, Baokang Bi and Mike Rich for their help on various instruments.

Finally I would like to thank my parents for always supporting me and my wife, Chunjuan, for her love.

TABLE OF CONTENTS

LIST OF TABLES

LIST OF FIGURES

LIST OF SCHEMES

Chapter 1. Introduction

Background

Since the 1970s oil crisis caused by the Arab Oil Embargo of OAPEC, the world has been faced with the reality of a limited supply of petroleum and a dramatically increasing rate of global energy. During the most recent half century, the term "renewable energy" has come to represent a sustainable energy future. As he International Energy Agency explains[1], "Renewable energy is derived from natural processes that are replenished constantly. In its various forms, it derives directly from the sun, or from heat generated deep within the earth. Included in the definition is electricity and heat generated from solar, wind, ocean, hydropower, biomass, geothermal resources, and bio fuels and hydrogen derived from renewable resources." Due to the digious amount of solar energy continuously striking the surface of the earth, solar energy is deemed to be the renewable energy resource with the greatest potential human needs.

A solar cell is an electrical device that converts photons from sunlight directly into electricity via the photovoltaic effect. The first solar cell was built by Charles Fritts[2] in 1883; he coated a semiconductor comprised of selenium with an ultra thin layer of gold to generate a heterojunction. His device achieved an efficiency of 1%. Later in 1950s, a group at Bell labs[3] built the first practical solar cell based on silicon p-n junctions, typically referred to now as the 1st generation solar cell. To this date, photovoltaic technology was mostly been dominated by 1stgeneration, single-crystal silicon solar cells. However the penetration of this technology into the market is strongly limited by the high cost of purifying the crystalline silicon, particularly by the high energy requirements of the manufacturing process. The goal of 2nd generation solar cells is to produce a cheaper solar cell, particularly as measured by energy cost of production, by applying thin-film technology, including amorphous silicon[4] (a-Si), cadmium telluride (CdTe) and copper indium gallium selenide (CIGS). These thin-film technologies, which use micrometers of material, can substantially lower the energy requirements, and hence the manufacturing cost. However the 2nd generation solar cells have significant limitations, including lower overall efficiency compared to 1st generation and the toxicity of the component materials used. These limitations have inspired researchers to investigate a 3rd generation of solar cell, focusing on cheaper organic and polymer materials with substantially lower manufacturing costs, greater flexibility, and ultimately, higher efficiency.

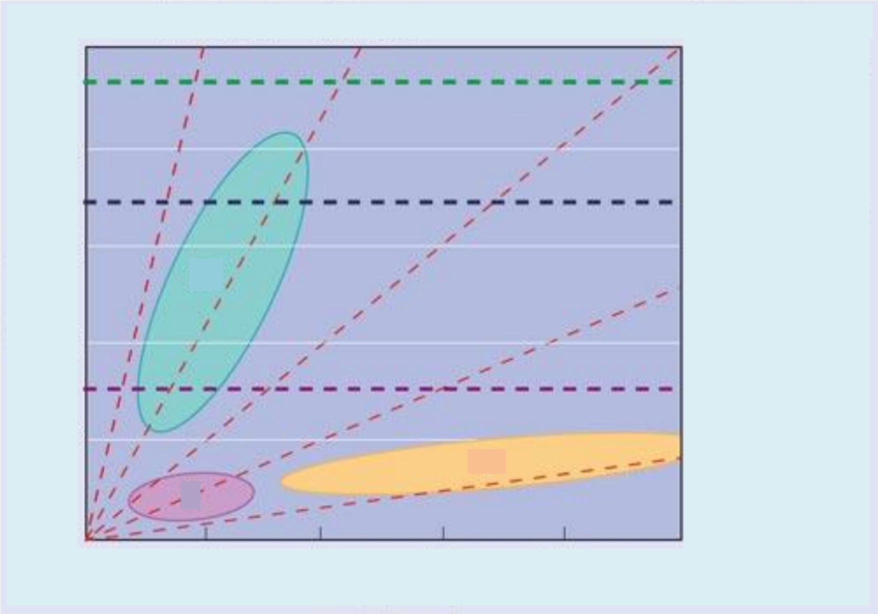

Figure 1.1 Cost and efficiency of 1st, 2nd, and 3rd generation solar cells. (For interpretation of the references to color in this and all other figures, the reader is referred to the electronic version of this dissertation.)

The organic photovoltaic cell (OPVC) is one of the most promising members of the family of 3rd generation solar cells, which are typically classified into two groups based upon the materials used for their fabrication. The first group is called a full organic solar cell, and is made entirely from organic or polymeric molecules. The prototypical examples of this first type of solar cell includes the bulk heterojunction solar cell[5] (BHJ solar cell) and the organic/inorganic hybrid solar cell. Most cells in this group are composed of organic-inorganic blends. In particular the solid-state dye sensitized solar cell (ss-DSSC) is fabricated by infiltrating organic conductor into a porous dye-coated inorganic semiconductor. Other hybrid-3rd generation solar cells incorporate a combination of inorganic semiconductors, quantum dots, and polymer co-joined molecular. In this chapter, We will give a detailed overview of the fabrication and properties of DSSC and ss-DSSC solar cells related to my thesis as well as a brief introduction of other OPVC.

Dye sensitized solar cells

In 1991, O' Regan and Grätzel,[6] from the Ecole Polytechnique Federale de Lausanne (EPFL), first demonstrated an electrochemical solar cell ~~which~~ based upon a meso-porous nano-crystalline titanium oxide anode coated with a Ru dye as a photon absorber. The intellectual breakthrough was the small-scale morphology of the photoanode, with inter-percolating domains of electrolyte and semi-conductor interfacing through the thin layer of dye. This seminal solar cell assembly, often called a Grätzel or dye-sensitized solar cell, reached an energy efficiency of 7% with a large current density 12 mA/cm^2. After two decades of primarily incremental improvement, the efficiency has climbed to over 12%[7] through the introduction of novel materials. Typically, dye sensitized solar cells are built from cheap and abundant metal oxides, such as the titanium oxide (TiO_2) semiconductor, with surface-rich structure. The choice of absorber is predicated upon the visible light spectrum available, and the absorbers band-gap structure, which modulates its rate and energy loss when injecting electrons into the semi-conductor. The light absorber is typically a metal complex with a strong anchoring group connecting it to the surface of TiO_2. To efficiently complete the charge transport, while preventing a short circuit, a redox couple (eg. I^-/I_3^- or Co^{2+}/Co^{3+}) or a hole transport material (HTM) is sandwiched between the photoanode and counter electrode. The device assembly is completed with a highly transparent conductive glass on the photon incident-side (anode) and a reflective backside at the counter. The components of a typical DSSC are shown in Figure 1.2, the working mechanisms of the DSSC are discussed later of this chapter.

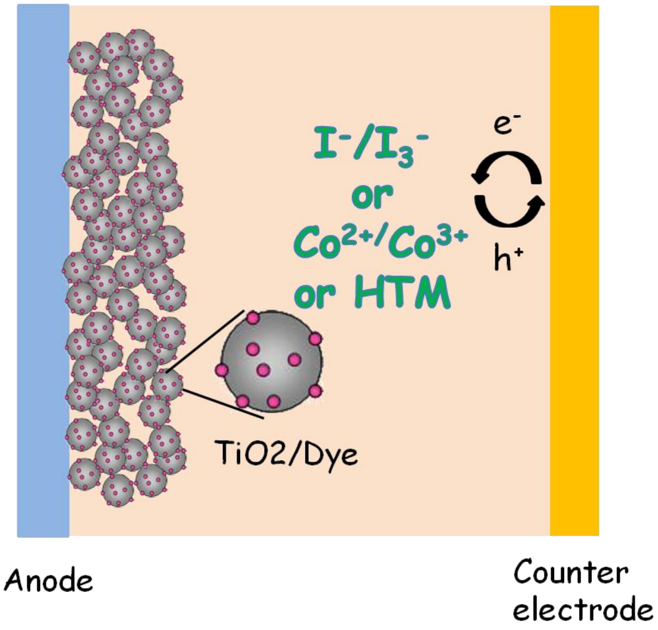

Figure 1.2 A scheme presenting the dye sensitized solar cell and its components.

Solid-state dye sensitized solar cell

Roughly 80% of papers in the scientific literature about DSSC consider the classical liquid based DSSC. Here “liquid” refers to an electrolyte that is dissolved in a solvent, such as acetonitrile (MeCN).While liquid electrolytes are efficient, they have significant limitations. Acetonitrile is a volatile, flammable and corrosive liquid electrolyte that leads to significant longevity problems, culminating in the cell’s loss of efficiency over time. A second major problem is that liquid electrolyte may leak from the device even after careful sealing. Additional sealing issues arise in the use of MeCN or other common solvents, since water and oxygen must be mostly sealed out to prevent oxidation and other contamination.

Quasi solid-state electrolytes (quasi ss-DSSC) including polymeric ionic gel and ionic liquid electrolytes (see Figure 1.3) have been developed as alternatives to liquid electrolytes. These avoid the sealing and corrosion issues, while offering high ionic conductivity. For polymeric ionic gels, several polymer matrices are commonly used, such as poly (ethylene oxide) (PEO). In 1999, De Paoli and coworkers[8] reported the first DSSC assembled with a polymer electrolyte. Their device was assembled with poly(o-methoxyaniline) as the sensitizer and an electrolyte formed from a copolymer of PEO containing NaI/I_2. De Paoli obtained a substantially lower efficiency (less than 1%). Later, Fang[9] developed a novel necklace-like polymer gel electrolyte consisting of polypyridyl-pendant poly(amidoamine) dendritic derivatives and $I(CH_2CH_2O)nCH_2CH_2I$ as latent chemically cross-linked gel electrolyte precursors. Their assembled quasi ss-DSSC exhibited a conversion efficiency of 7.7%.

Polyethylene oxide (PEO)

1-Propyl-3-methylimidazolium iodide

Figure 1.3 Examples of polymeric ionic gel and ionic liquid used in DSSCs.

Ionic liquids have many advantages, such as non-volatility, chemical and thermal stability, mid-level ionic conductivity and non-flammability that make them promising candidates for the electrolyte of a DSSC[10]. The imidazolium iodide-based ionic liquid[11] have been broadly used in DSSC. However, the viscosity of the iodide melts should be as low as possible to avoid mass transport limitations in the photocurrent and the associated loss of fill factor. Grätzel and Wang introduced the idea of using eutectic melts to reduce the viscosity of the electrolyte thereby enhance the ionic conductivity. In this manner they achieved an efficiency of 7.4%[12] and 8.2%[13]. As an additional means to lower the viscosity, Hu from our group recently has tried to decrease the glass transition temperature (T_g) of the poly-ionic liquid electrolyte by exchanging the halide anion of imidazolium to TFSI anion after polymerization, or by tethering longer PEO or alky chains onto the monomer before polymerization. The resulting more than 50 degree reduction of T_g, yielded a polyelectrolyte with a solid-like form with lower viscosity and a higher ionic conductivity of 1 mS/cm. However, quasi ss-DSSCs are not a real substitute for an ss-DSSC. The quasi-solid state cells still require a redox couple in a liquid solvent; volatility issues may be reduced, but are not eliminated. Indeed, the term "solid state" refers exclusively to the family of DSSCs that use hole transport materials (HTM) as the charge transfer mechanism between the photo-anode and the counter-electrode. This group includes organic and inorganic hole conductors. The most widely used HTM is 2, 2', 7, 7' -tetrakis (N, N-di-p-methoxyphenylamine) 9, 9'-spirobifluorene, also known as spiro-MeOTAD. In 1998, the first ss-DSSC was reported by Udo Bach, a former graduate student from Grätzel's group at EPFL[14].

Working principle of ss-DSSC

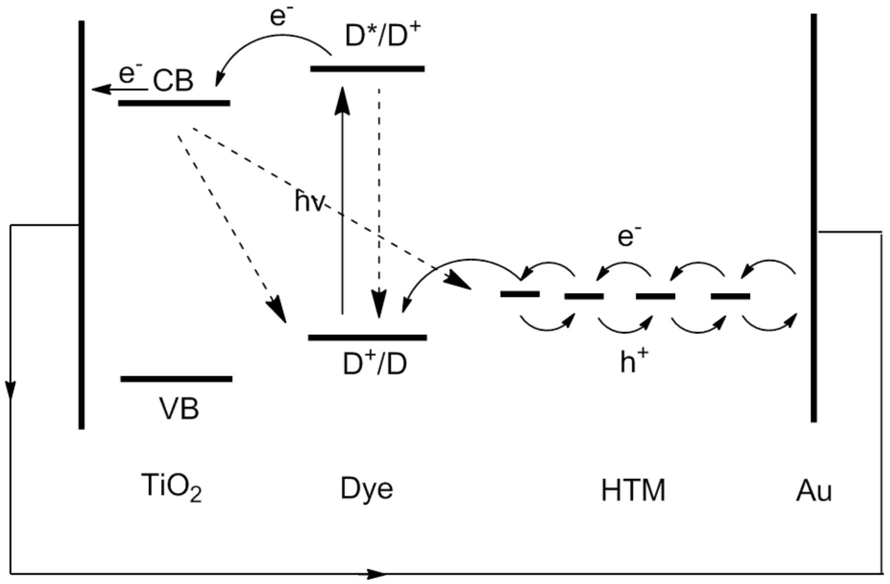

Figure 1.4 Schematic illustration of the working principle of DSSC.

An outline of the working principles of ass-DSSC are depicted in Figure 1.4.Incident photons (hv) are absorbed by the dye molecule which is physically tethered to the TiO_2 semiconductor, the photon absorption excites the dye molecule from its ground state (D) into its excited state (D*), from which an energetic electron is rapidly injected into the conduction band (CB) of the TiO_2. A continuous conduction path leads the electrons to the Au cathode from the anode through the external circuit. Concurrently, the HTM regenerates the reduced state D* back to D and the HTM transferring the electron hole to the Au electrode through a hopping mechanism. The major difference between the liquid-based DSSC and ss-DSSC, is that the charge transfer in the liquid-based DSSC occurs through the ionic diffusion of the redox couple while an ss-DSSC effects the charge transfer through the hole transporting. In addition to these necessary charge transport processes, also called forward reactions, there also exist undesirable back reactions, including the spontaneous decay of excited dyes and charge recombination between the injected electrons and the dye or the HTM. These back reactions play a fundamental role in overall cell efficiency and limiting performance.

Solar cell characterization and performance evaluation

The current-voltage (I-V) relation is a key diagnostic used to evaluate solar cell performance. It is performed either under illumination or in the dark, however the standard irradiance condition, the Air Mass 1.5 Global (AM 1.5G) illumination, has an incident power density 100 mW/cm^{2}at 25 ℃. The Air Mass (AM) here indicates the ratio of the path length of the sun's rays through the atmosphere when the sun is at a certain angle θ to the zenith, to the path length when the sun is at its zenith. The relation can be approximated by:

$$AM = \frac{1}{\cos\theta}$$

Therefore, the AM 1.5 corresponds to a solar incident angle of 48.2°relative to the surface normal.

The features of typical I-V curves are well described by the Shottky equation:

$$I(V) = I_{ph} - I_0(e^{\frac{eV}{nkT}-1}) - \frac{V + IR_S}{R_P}$$

Where I_{ph} is the photo current, I_0 is the saturation current of the diode, n is the ideality factor, k is the Boltzmann constant, and T is the cell temperature, R_S is the series resistance, and R_p the shunt resistance. Areal solar cell, especially ss-DSSC, can exhibit substantially more complicated behavior than that affored by this idealized relation, however the simple Shottky equation is helpful to provide a crude justification for the shape of the I-V curves, and to relate the shape back to the basic processes occurring within the cell. There are four basic parameters that may be identified from a typical I-V curve:

Short-circuit current (I_{SC}): solar cell photocurrent measured at standard illumination and an applied potential of 0V – that is, a short circuit between the cell's anode and cathode. I_{SC} is a function of the illumination intensity, but affords a measurement of the cell's internal resistance, the density and absorption properties of the dye, and facility of the electrolyte or HTM to regenerate the dye. The short circuit current density (J_{SC}) is the short circuit current divided by the illuminated active area of the cell.

Open circuit voltage (V_{OC}): under standard illumination, the voltage produced by the cell when the anode and cathode are not electrically connected; equivalently, the imposed potential at which the cell produces zero current. In DSSCs, V_{OC} can be roughly estimated by the difference of redox potential and Fermi level of TiO_2. A lower V_{OC} is strongly suggestive of an elevated rate of charge recombination.

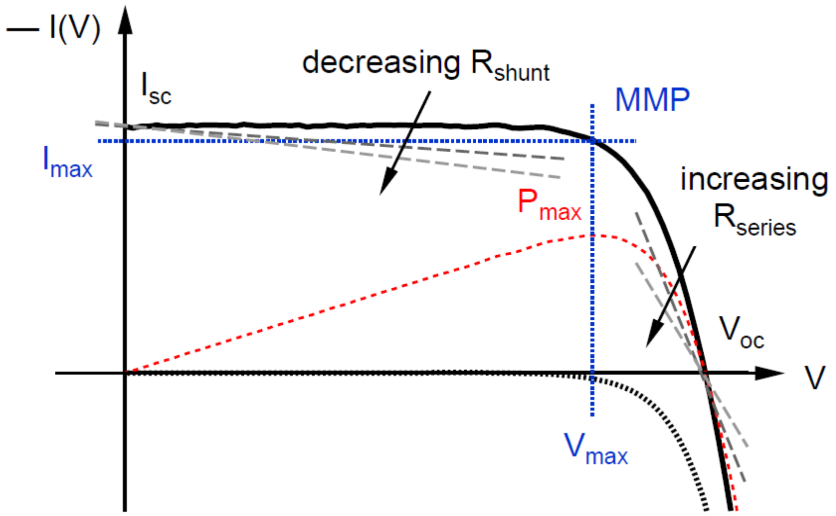

Figure 1.5 I-V curve of a typical solar cell under illumination (bold dark curve) and in the dark (dotted dark curve). Further indicated are the power curve (red), the maximum powerpoint (MMP, blue) conditions, and the effect of the series and shunt resistance.

Fill factor (FF): The FF is the ratio of the maximum power the cell can provide to the theoretical power that would be obtained if the short-circuit current could be achieved at the open-circuit voltage:

$$FF = \frac{P_{\max}}{I_{sc}V_{oc}} = \frac{I_{\max}V_{\max}}{I_{sc}V_{oc}}$$

Here P_{max} is the maximum power found on the I-V curve with the corresponded I_{max} and V_{max}. The FF ranges between 0 and 1, with a value of 1 corresponding to zero internal cell resistance. The higher the value of the FF derived from I-V curve, the better the internal transport is within the fabricated cell. The FF is influenced by R_S from the internal resistance (eg. interface contact, material defects and material resistance) and R_p from the loss of current (eg. charge recombination), although this latter effect is partially subsumed within the open-circuit voltage. To obtain high FF, R_s needs to be small, while R_p should be as large as possible.

Power conversion efficiency (η): The ratio of the maximum cell power, P_{max}, to the incident radiation power, P_{in}; equivalently, the percentage of incident power harnessed by the cell. The power conversion efficiency is dependent upon J_{sc}, V_{oc} and FF from device fabricated, taking the simple algebraic form

$$\eta = \frac{P_{\mathrm{max}}}{P_{\mathrm{in}}} = \frac{J_{sc} V_{oc} FF}{P_{\mathrm{in}}}$$

Components of a ss-DSSC

A typical ss-DSSC is comprised of up of six distinct components, arranged in a layered structure. As shown in Figure 1.6 these include (from bottom to top): transparent conducting glass (FTO glass), the TiO_2 compact layer, the nanocrystalline TiO_2 (nc-TiO_2) layer, a photon absorbing dye, HTM, and metal electrode. Each component plays an essential role, and the performance of the ss-DSSC is sensitive to each. In the following sections the required properties and roles of each component is discussed in turn.

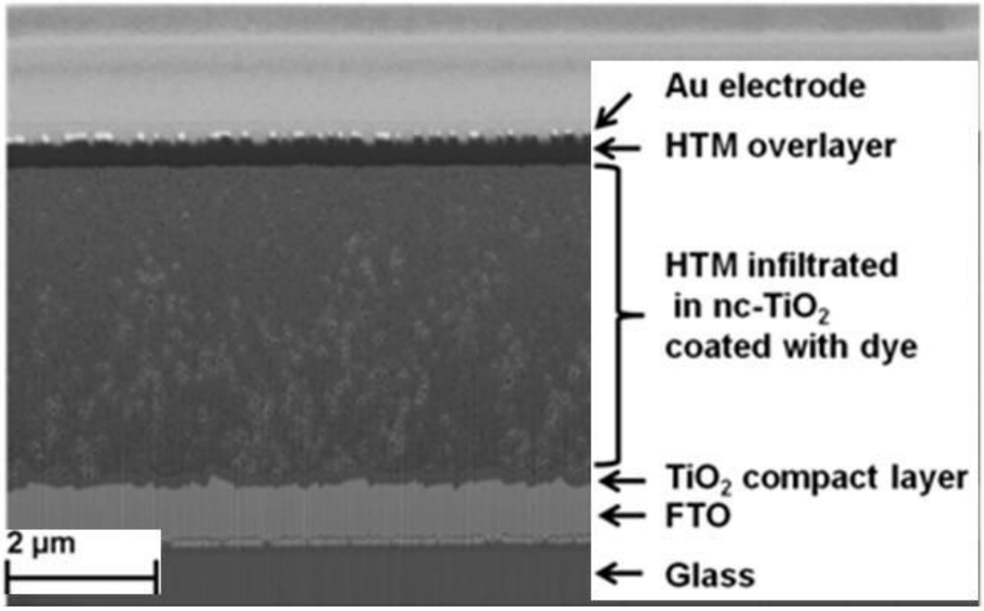

Figure 1.6 Cross-sectional SEM image of an ss-DSSC (Obtained by Wen Yuan).

Transparent conducting glass

The transparent conducting glass must be highly electrically conductive and highly transparent, with sufficient thermal stability to serve as the substrate for subsequent deposition and sintering of the TiO_2 paste. FTO glass, made by fluorine-doped tin oxide (FTO) coated on glass, is a widely used choice for the transparent conducting glass. In the Baker lab, we use a commercial TEC 8 or TEC 15 FTO glass, the value of 8 or 15 refers to the its sheet resistance, purchased directly from Pilkington and post-cut it to small pieces (1×0.75 in). The sheet resistance is about 8-15 Ω/square with a transmittance of 80-85% in the visible region. Since the bulk device's resistance is much larger than these numbers[15], the additional 7 Ω/square resistance in difference is negligible between TEC 8 and TEC 15. The surface morphology of FTO glass is crucial as well: the roughness of the FTO glass and geometry of FTO grain may affect the adhesion and uniformity of the TiO_2 compact layer when it is spread onto the FTO glass. The compact layer has a typical thickness of 50-200nm, so that extensive surface roughness of the FTO could cause it to perforate the compact layer. We used Atomic Force Microscopy (AFM) to compare the TEC 8 and TEC 15 surface morphologies (Figureure 1.7). TEC 8 has a roughness of 27 nm, which is twice as large as the 13 nm roughness of TEC 15. Also TEC 8 apparently is comprised of bigger particles than TEC 15. This has significance for the transparency since Rayleigh's scattering formula:

$$I = I_0 \frac{1+\cos^2\theta}{2R^2}\left(\frac{2\pi}{\lambda}\right)^4\left(\frac{n^2-1}{n^2+2}\right)^2\left(\frac{d}{2}\right)^6$$

relates the intensity I of scattered light to I_0, the intensity of incident light, θ, the scattering angle, R, the distance to the particle, λ, the wavelength of incident light, n, the refractive index, and d, the particle diameter. Clearly smaller particles enhance the transparency since the intensity of scattered light falls off with the sixth power of particle diameter. This is consistent with the observation that TEC 15 is more transparent than TEC 8.

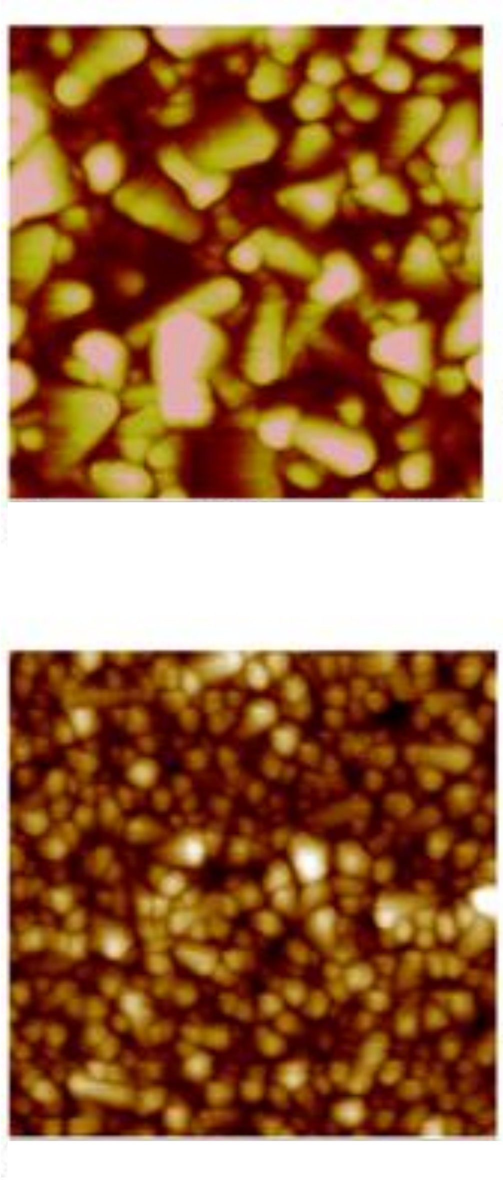

Figure 1.7 AFM image of TEC 8 (Left up) and TEC 15 (Left bottom) FTO glass and their corresponded 3D view. The scale is 2×2 μm with a ±50 nm scale bar. (Images obtained by Wen Yuan)

There are other choices for the transparent conducting. Compared to FTO glass, indium tin oxide (ITO) glass has better transparency and less surface roughness. However, ITO experiences significant losses of conductivity after high temperature baking, and is considerably more expensive than FTO. A graphene ultrathin film spray-deposited on transparent glass can be used to replace the FTO glass. These films exhibit a high conductivity, around 550 S/cm, and a somewhat lower transparency of 50-60% (Figureure 1.8) in the visible spectrum. An ss-DSSC assembly has achieved an efficiency of 0.3%[16].

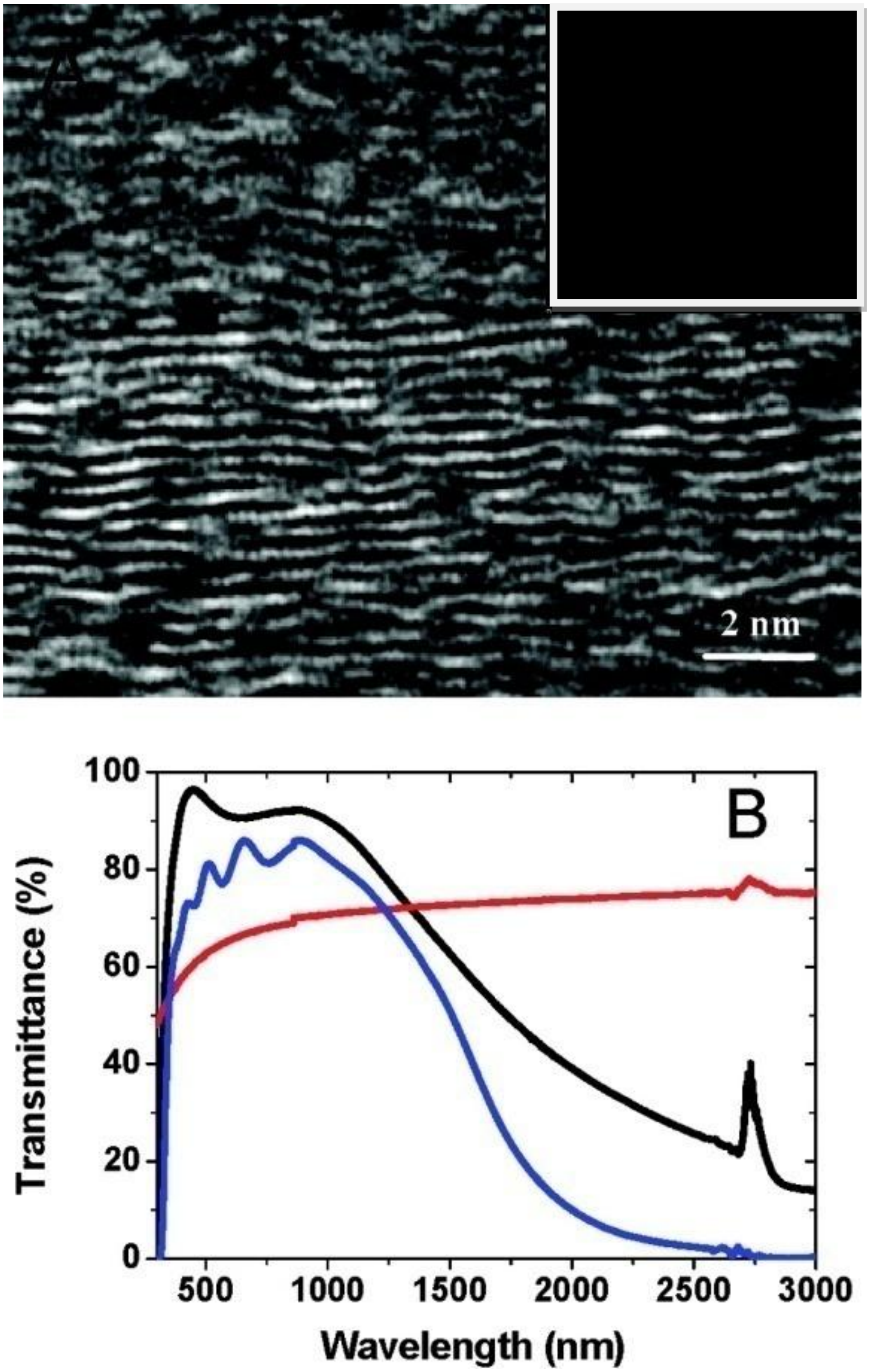

Figure 1.8 Structure and transmittance of graphene films. (A) HRTEM image of graphene films with corresponding SAED pattern (inset). (B) Transmittance of a ca. 10 nm thick graphene film (red), in comparison with that of ITO (black) and FTO (blue).

TiO_2 compact layer

The TiO_2 compact layer (also called TiO_2 blocking layer or TiO_2 dense layer) is the first layer coated onto the FTO glass. It is used to block direct contact between the FTO and the HTM. HTMs, like spiro-MeOTAD, exhibit an ohmic-contact resistance at junctions with a metal like FTO glass. The FTO-HTM contact can also lead to increased charge recombination in a buck device that serves to lower the open-circuit voltage and hence the overall cell efficiency. To address these problems, a pin-hole free thin TiO_2 layer is deposited on the FTO before applying the nc-TiO_2 layer. Several deposition methods for TiO_2 compact layer have been investigated, including reactive sputtering[17], spray pyrolysis[17], MOCVD[17], dip-coating[18], spin-coating[19] and ALD[20]. A commonly used titanium precursor is a diluted titanium bis(acetoacetonato)-di(isopropanoxylate)ethanol solution. In the Baker lab, we currently use spray pyrolysis based upon a procedure developed by Grätzel's group[17,21]. A set-up of spray pyrolysis is shown in Figure 1.9. Spray cycles, air flow, precursor's concentration, and the distance from the FTO to the sprayer all impact the thickness and uniformity of the compact layer.

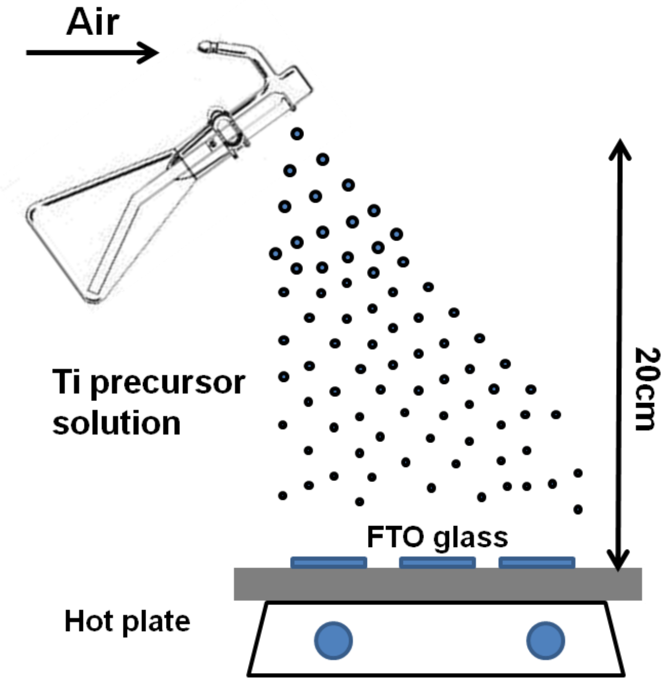

Figure 1.9 Spray pyrolysis set-up with a TLC chromatography sprayer in our lab

In 2004[22] Peng's group observed a linear increase in TiO_2 thickness with the number of spray cycles, with an optimal performance at a thickness of 150nm. In addition to the thickness of compact layer, the surface properties also affect the quality of the resulting ss-DSSC. Based on microscope imaging in Figure 1.10, the compact layer roughness fell to 10 nm from original 13 nm of a bared FTO glass, which resulted from uniformly smaller TiO_2 particles deposited.

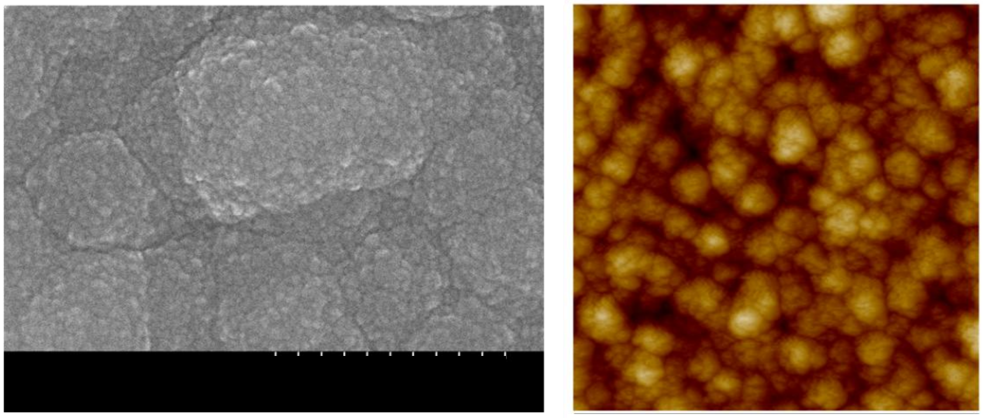

Figure 1.10 SEM image (Left) & AFM image (Right) of TiO_2 compact layer on FTO glass. The scale bar of SEM is 300nm, and scale bar of AFM is±50nm. (Images obtained by Wen Yuan)

Nanocrystalline TiO_2 (nc-TiO_2)

The nanocrystalline TiO_2 (nc-TiO_2) layer collects the injected charge from the excited dye and provides a conduction path to the FTO glass. It typically has a porous structure with a particle size around 10-30 nm in diameter. The pore-rich structure provides a large surface area covered with hydroxyl group that provide natural sites to absorb dye molecules through chemical bonding. Also the void space within the nc-TiO_2 allows an interpenetrated mixing with either a liquid or a solid-state electrolyte. The interpenetration of the nc-TiO_2 with an electrolyte is required to achieve the dye regeneration following electron injection into the nc-TiO_2; however the high nc-TiO_2/electrolyte surface area also raises the possibility of parasitic charge recombination.

The nc-TiO_2 film can be adhered to the compact TiO_2 substrate in several manners, including: doctor-blading, dip-coating, screen-printing, or spin-coating. However, since a DSSC typically requires a micrometer level thickness of nc-TiO_2 film, dip-coating or spin-coating techniques are not suitable to obtain a thicker layer.

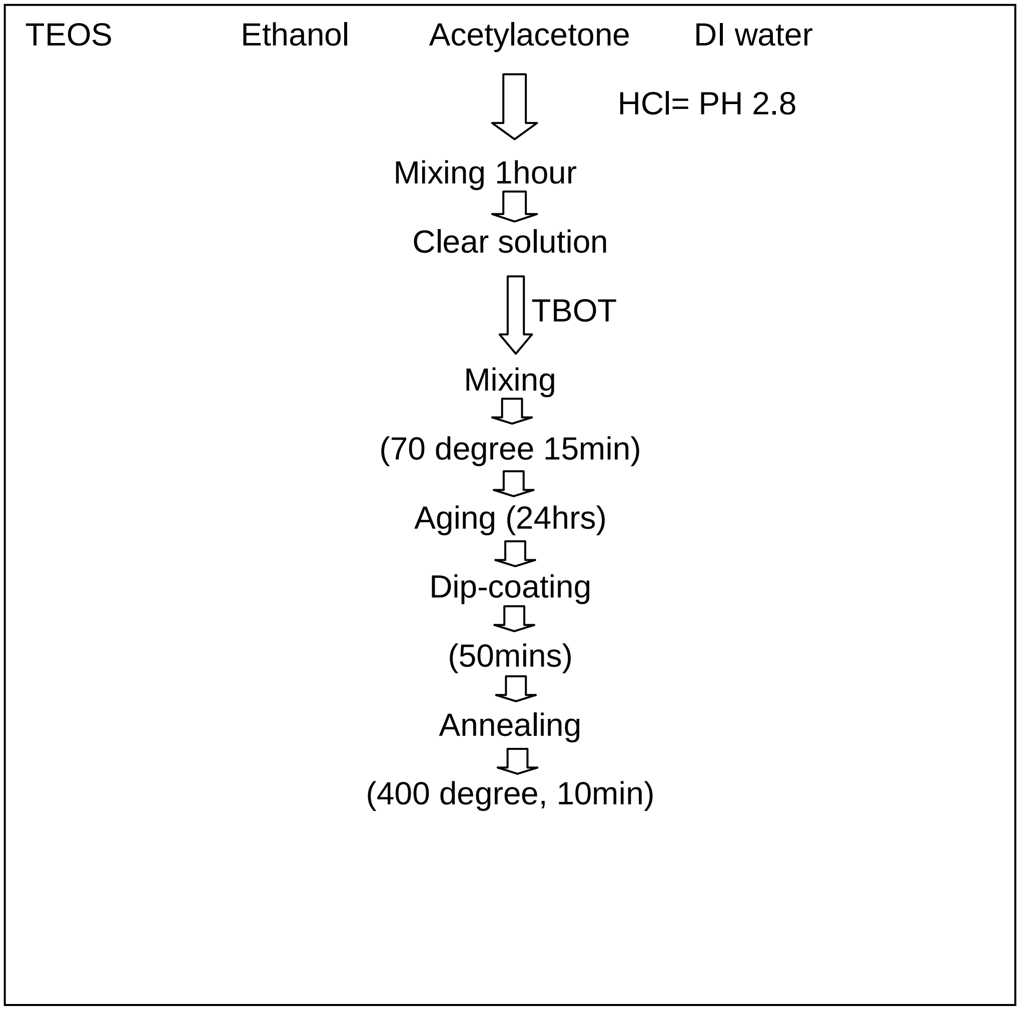

Figure 1.11 Diagram illustratingthe preparation of TiO_2 paste and its film deposition

For the doctor-blading technique, one applied a TiO_2 paste consisting of TiO_2 nanoparticles, organic binder or templates, and solvent. The TiO_2 nanoparticles can either be from commercially available stock, such as P25[24,25] from Degussa or made by precursor through a hydrothermal method[23,26] (seen in Figure 1.12A & B), mixing with organic binder (such as ethyl cellulose) and a blend of solvents such as terpineol or ethanol. Many home-made recipes of TiO_2 paste have been developed, each with different advantages. There are also a couple of commercial choices such as Solaronix SA and Dyesol. The most often used paste in the Baker lab is Ti-Nanoixde T purchased from Solaronix SA (seen in Figure 1.12C & D). With this paste we can consistently achieve a 2.5 μm thick layer through doctor-blading with a Scotch tape spacer (60 μm, 3M Company).

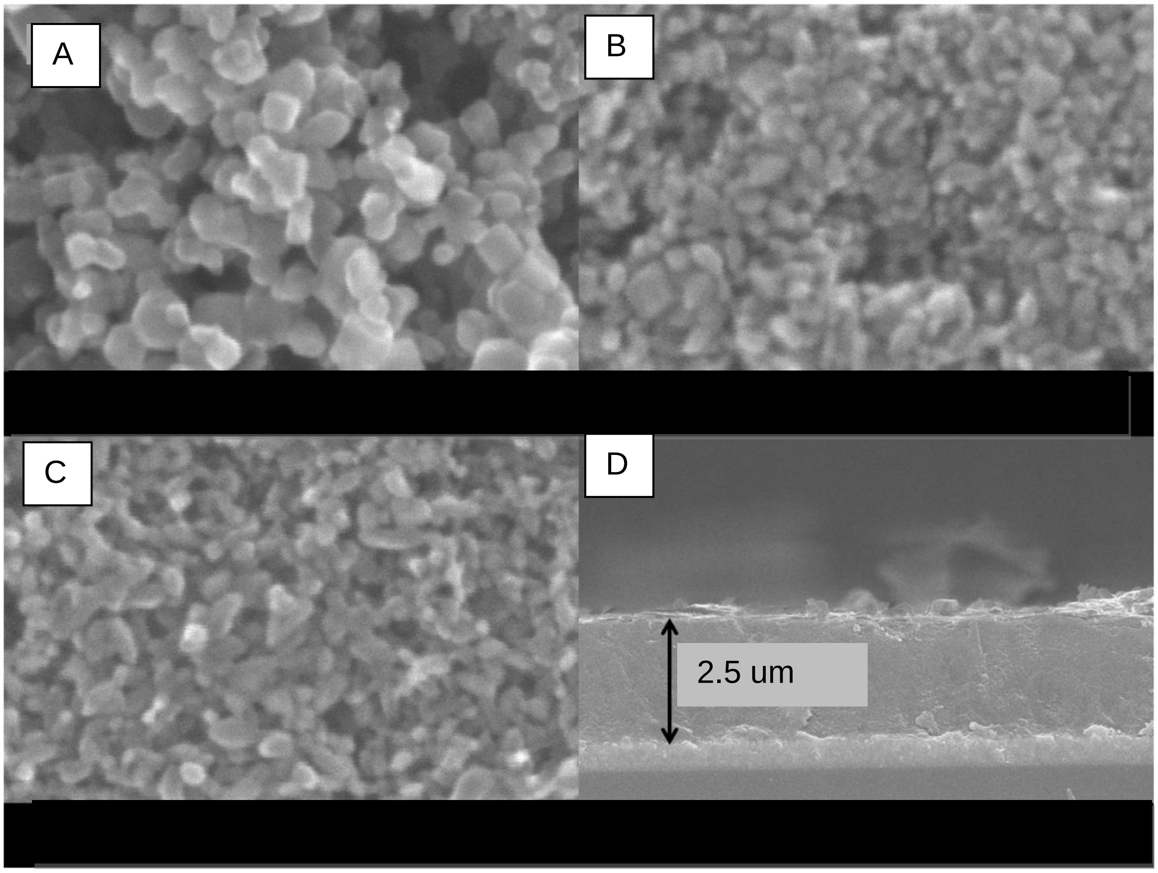

Figure 1.12 SEM images of nc-TiO_2 film: from (A), a home-made TiO_2 paste based on P25; (B), a home-made TiO_2 paste prepared through a hydrothermal method; (C) Ti-Nanoixde T purchased from Solaronix SA; and (D) its corresponding cross sectional structure. (Images obtained by Wen Yuan)

In addition to regular mesoporous nc-TiO_2, ss-DSSCs incorporated with TiO_2 nanotubes[28] or nanorods[29] recently have also been synthesized with the aim to enhance electron transport through well-aligned pathways. However, efficiency obtained by these methods does not compete with nc-TiO_2 based ss-DSSC since due to a poorer dye loading arising from a loss of semi-conductor/electrolyte surface area.

An alternate approach to regulating the morphology of the TiO_2/electrolyte mixture is through phase-separation of polymer-templated with a TiO_2 precursor. The templates chosen are typically block copolymers with hydrophobic and hydrophilic domain, like Pluronic 123 (poly (ethylene oxide-b-propylene oxide-b-ethylene oxide) (PEO-PPO-PEO)[30,31], poly (isoprene-b-ethylene oxide) (PI-PEO)[32-34]. By controlling the ratio of the two different blocks, an ordered, tunable mesoporous structure could be produced in-situ during the annealing[32]. Recent work from Dr.Snaith[34] demonstratesss-DSSCs up to 5% of efficiency using atriblockterpolymer poly (isoprene-b-styrene-b-ethylene oxide)(PI-PS-PEO) resulting in a highly porous TiO_2 structure.

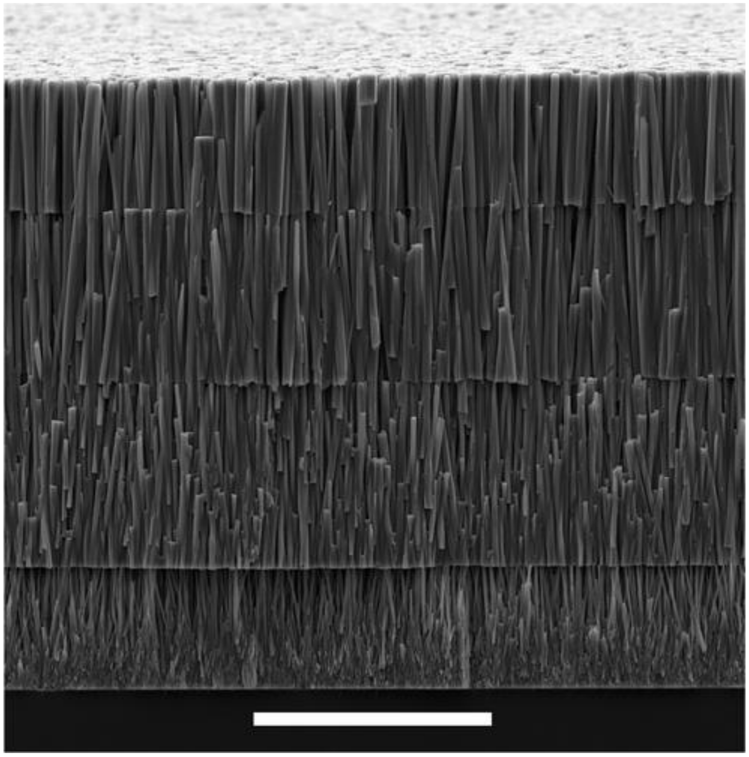

Figure 1.13 SEM image of a four-layer ZnO nanowire array. [Scale bar, 20 μm]

Other non-TiO_2 metal oxide electrodes, Zinc Oxide (ZnO)[35-38]and Tin Oxide (SnO_2), have also been employed in ss-DSSC design. Gao's group used multilayer TiO_2-coated ZnO nanowire arrays (50 μm) as the photoanode in ss-DSSC to achieve an efficiency over 5%. A well-oriented ZnO nanowire without any collapse was grown on FTO substrate (Figure 1.13), which could absorb more dye than usual and further generate more photocurrent. Also a TiO_2 embedded with ZnO nanowire helped improve the photovoltaic performance[37]. SnO_2 based ss-DSSC was first explored by Snaith's group[39], whose SnO_2

–based devices with a MgO coating and an Al_2O_3 interlayer yielded an efficiency over 1% -- thereby breaking the monopoly of TiO_2 and ZnO over DSSC assemblies.

The light absorber (dye)

A working photoanode includes an nc-TiO_2 film and a light absorber (dye). The dye molecules are coated onto the nc-TiO_2 film by immersing the porous film in a dye solution. In order to maximize the injection of excited electrons from the dye into the conduction band of TiO_2, the dye molecules should be strongly bonded and uniformly coat the surface of nc-TiO_2. The most common anchoring group for the dye is a carboxylic group (-COOH), which reacts with the hydroxyl groups on the nc-TiO_2 surface, forming a strong covalent bond.

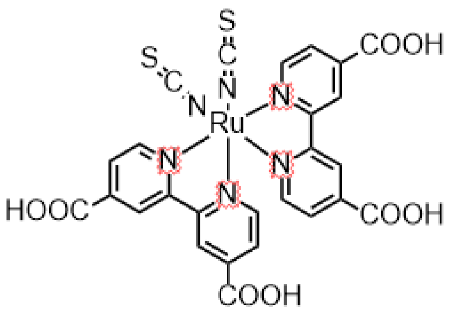

N3 Dye

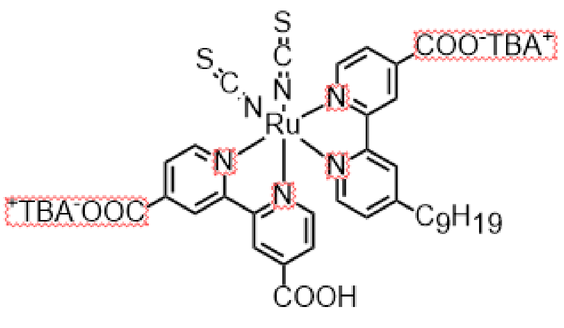

N719 Dye

Figure 1.14 (cont'd) Ruthenium Dye in DSSC: N3 Dye (left) and N719 Dye (right)

Three different types of light absorbers are used in DSSCs. They are metal complex dyes, metal-free organic dyes and quantum dots. Ruthenium complexes absorb light throughout the visible spectrum and were first developed for DSSCs[40]. At present, the ruthenium (II)–polypyridyl complex is widely used as dye molecule (see Figure 1.14), indeed the efficiency record for a DSSC with a ruthenium dye is over 11%[41]. However, ruthenium has a significant draw-back: being a rare-earth element, it is quite expensive. Consequently, other metal complexes have been studied[42], such as iron, copper, osmium, and zinc complexes. Indeed, a zinc-porphyrin system incorporated within a DSSC has demonstrated the highest recorded energy conversion efficiency, 12%, of DSSC to date[7]. Unlike ruthenium systems, the porphyrin exhibits strong absorption in the near-IR region due to an additional Q-band in the 500-700 nm region with good stability. The asymmetric porphyrin dye (YD2-o-C8) was synthesized by introducing triarylamine as electron donor and carboxylic acid as acceptor. By co-sensitizing the zinc-porphyrin complex with an Y123 Dye (Figure 1.15) from Grätzel's group, the visible spectrum from 400 nm to 700 nm can be covered entirely[7].

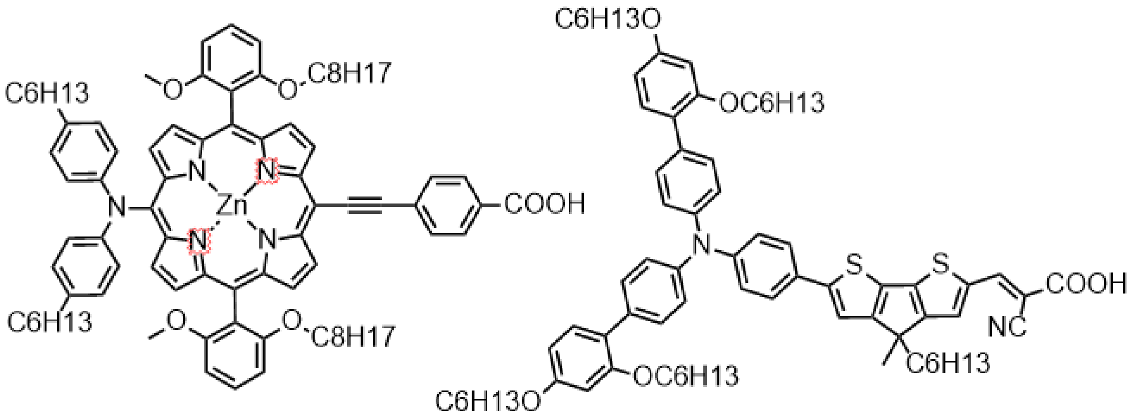

YD2-o-C8 Dye

Y123 Dye

Figure 1.15 Zinc porphyrin complex (YD2-o-C8 Dye) with organic dye (Y123 Dye)

Metal-free organic dyes[42,43] are an alternative to the metal complexes dye with many advantages: (1) The molar extinction coefficient of organic dye is much higher than that of metal complex, making it attractive for thin film ss-DSSC. (2) The substantially lower cost of synthetic starting materials makes organic dye preferable. (3) The organic dye can be easily designed and synthesized. Generally, donor-π-bridge-acceptor (D-π-A) structures (see Figure 1.16) area common characteristic of organic dyes. By altering the different blocks in the architecture, the absorption spectra can be extended to the near-IR region. As well, control of the HOMO and LUMO levels and can enhance the intramolecular charge separation. Many organic dyes have already been produced and some of them have even been commercialized. Particularly well-known organic dyes employed in ss-DSSC fabrication include indoline-based dye (D149 Dye[44]), carbazole-based dye (MK-2 Dye[45]), squaraine-based dye (SQ-2 Dye[46]), triarylamine-based dye (Y123 Dye[47], C220 Dye[48]), see Figure 1.17.

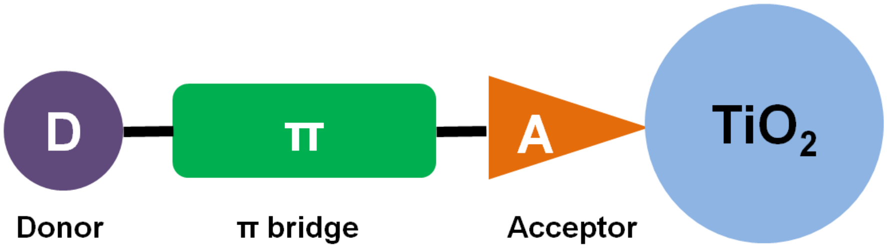

Figure 1.16 Schematic illustration of D-π-A organic dyes

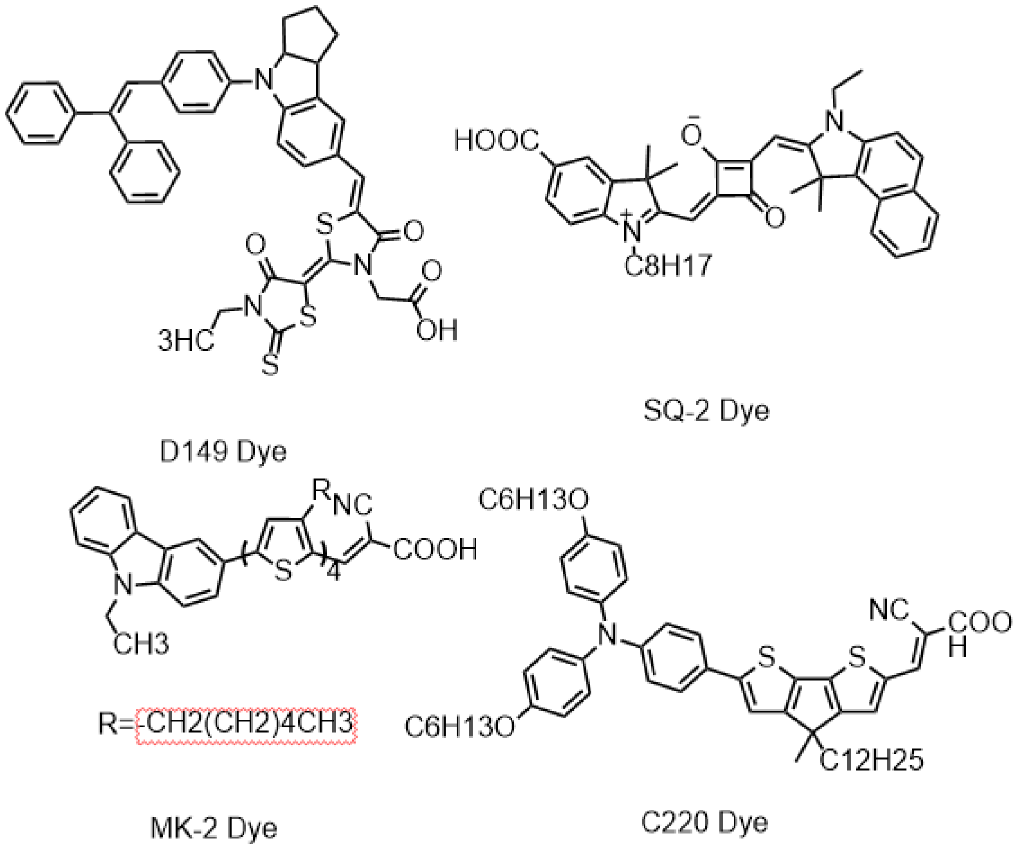

D149 Dye

SQ-2 Dye

MK-2 Dye

C220 Dye

Figure 1.17 Organic dyes employed in ss-DSSC fabrication.

Problems with interpenetration of solid HTM with the semi-conducting layer and poorer charge transport have driven ss-DSSC assembly towards thinner layers of nc-TiO_2. Indeed, the ss-DSSC semi-conductor layers are typically around 2-3 μm, compared to 10-12 μm for liquid electrolyte cells. Frankly, for ss-DSSC there are fewer good choices than for liquid cells. This is because the dye molecule must not only “wet” the nc-TiO_2 surface but also serve to induce the HTM into pore structure through an energetically favorable surface interaction. For these reasons, instead of the typical N3 dye, ss-DSSCs have often employed the Z907 dye (Figure 1.18) with amphiphilic chains that successfully assist the penetration of spiro-MeOTAD by hydrophobic modification[49]. Similarly, the K68 dye with tetra (ethylene oxide)-heptyl chain performs in a similar manner in ss-DSSC[50]. Another way to improve the ss-DSSC performance is to use a metal-free organic dye sensitizer with a higher extinction coefficient than the ruthenium complex (also see Figure 1.17). With this approach, Grätzel's group has reached a record efficiency of 7.2% with the Y123 Dye[47] (Figure 1.18) as light absorber. The structure of the Y123 Dye is highly adapted to ss-DSSC, being made from three parts: (1) a triarylamine unit donor tethered with four alkoxy chains. The alkoxy chain serves to adjust the energy level of dye, to repel direct electrolyte contact with theTiO_2 and thereby reduce charge recombination, and to "wet" the surface of TiO_2 pores. (2) acyclopentadithiophene based π-bridged unit serves to extend the absorption to the visible range of the solar spectrum. (3) acyanoacetic acid acceptor serves to strongly anchor the dye to the nc-TiO_2.

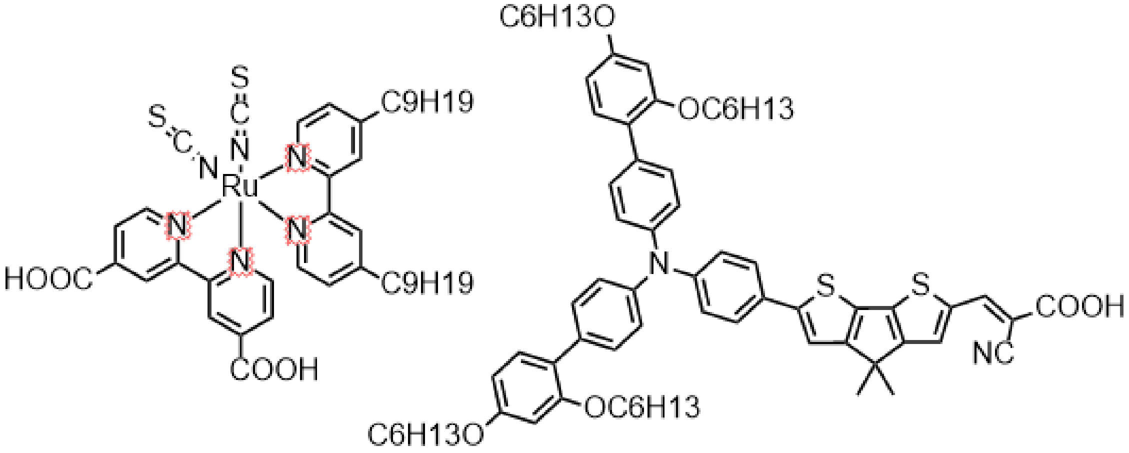

Z907 Dye

Y123 Dye

Figure 1.18 Z907 Dye (Left) and Y123 Dye (Right).

A particularly promising direction for the next generation of DSSC solar cells is the use of Quantum dots (QDs) semiconductors as light absorbers[51-53]. QDs offer advantageous features such as small size, shape-tunable optical properties, good photostability, high molar extinction coefficients, facile fabrication, and low cost. Much recent attention has focused on nc-TiO_2 films sensitized with QDs such as PbS[54], CdS[54-56], CdSe[57], or Sb_2S_3[58] in conjunction with spiro-MeOTAD. The superior light absorbance of QDs makes them particularly well suited to thin-layer and low illumination solar devices. Indeed, Grätzel's group recently obtained a QD-based ss-DSSC's with efficiency over 5% under 0.1 sun illumination. However, in their current incarnation, the QD cells produced by Gratzel's group showed significant current losses at higher light intensities, culminating in an 18%

current reduction at 1 sun over the current obtained at 0.1 sun. This surprising limitation may arise as from a slower rate of hole diffusion[58].

Hole transport material (HTM)

The hole transport material (HTM) serves as the charge transfer mediator and is located between the dye-coated nc-TiO_2 and counter electrode. It is responsible for regenerating the oxidized dye back to its ground state via a transfer of positive charge from the anode to the cathode. A good HTM must have: (1) energy levels which are well-aligned with those of the dye molecule so as to effect an efficient dye regeneration; (2) minimal light absorption in the visible spectrum, so as not to compete with dye molecule; (3) efficient infiltration into the negative space of the nc-TiO_2 pore structure; (4) high hole mobility; (5) good thermal and photostability for long-term operation. Common HTMs are inorganic crystalline compounds, such as CuI[59,60] and CuSCN[61,62], or organic molecular like spiro-MeOTAD[14], or polymeric materials, such as poly (3,4-ethylenedioxythiophene) (PEDOT)[63,64] and poly(3-hexylthiophene) (P3HT)[65]. The addition of Lithium bis(Trifluoromethanesulfonyl) imide (LiTFSI)[14] and 4-tert-butylpyridine (tBP)[66] may further optimize the cell's efficiency.

Inorganic p-type hole conductors were first used in solid type cells in 1995 by Tennakone who was able to obtain an impressively high photocurrent in a cell designed by infiltrating polycrystalline p-CuI into the nc-TiO_2. However, the cell could sustain its current for only 2 hours due to a serious photodegradation. The same photodegredation was also observed in cells using another copper salts, such as p-CuSCN, as the hole conductor. The major problem with p-type copper-based hole conductors is their poor conductivity that slows the rate of regeneration of excited dye molecules, consequently allowing the recombination of electrons from the conduction bands of the TiO_2 with the oxidized dye molecules or hole conductors. The conductivity of either CuSCN or of CuI prepared in the lab is too low to be of practical use in DSSC. Excess of SCN anions enables to induce p-type conductivity and the CuSCN film was further doped with SCN^- by soaking the film in a solution of $(SCN)_2$ in CCl_4. A higher conductivity CuSCN film can be also prepared by replacing some of the cuprous sites by triethylamine coordinated Cu(I) via concomitant $(SCN)_2$ doping[67]. After doping, the efficiency of the CuSCN-based DSSC increased from 0.75% to 2.39%[62].

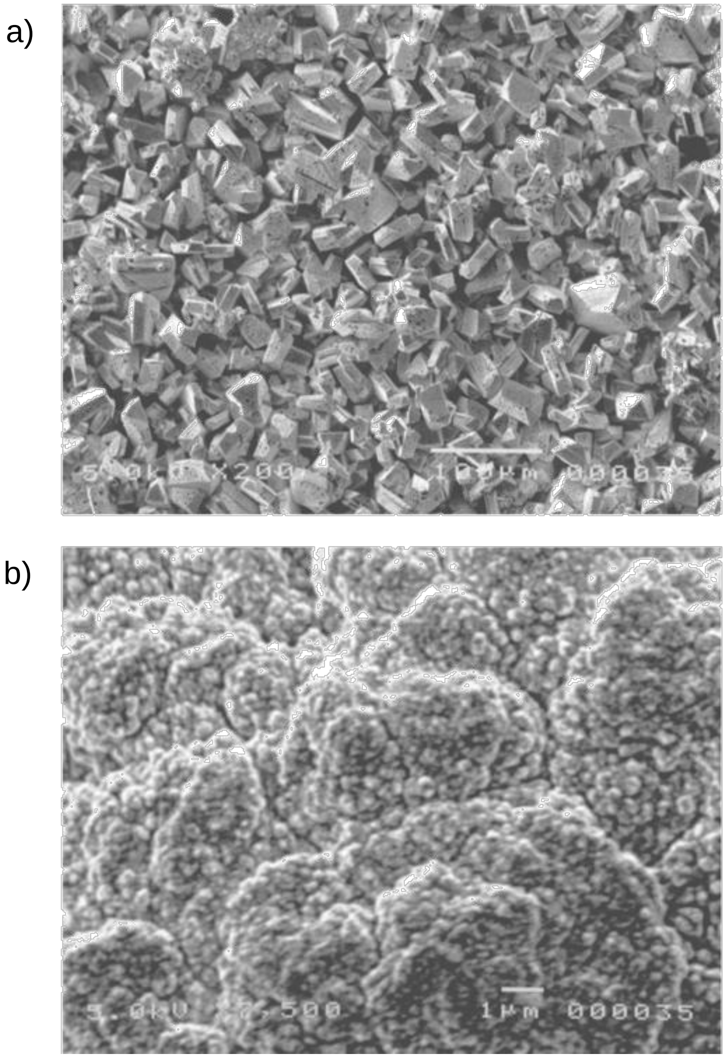

Figure 1.19 The SEM images of CuI layer on the dye-coated TiO_2 film: (a) without molten salt in the solution; (b) after adding molten salts in the solution.

One major difficulty with copper salts in ss-DSSC lies in the control of the size of the crystals which form within the pore space of the TiO_2 film. Excessive crystal size leads to an improper filling of the pores and poor contact with the dye-coated TiO_2. Overly large crystal sizes lead the ineffective charge transport and inefficient dye regeneration. Additionally, large crystals size can leave bared regions of TiO_2, which can enhance charge recombination with the hole conductor, further limiting the cell's stability. To overcome these limitations, Meng[60] and coworkers attempted to use molten salts as protective shell mixing with CuI (seen in Figure 1.19). The molten salts would concurrently improve the electrical contact between the dye-coated TiO_2 and the CuI. The molten-salt cells exhibited a higher efficiency and a greater stability, incurring on a 12% loss of efficiency of two weeks of continuous operation. Recently, Kanatzidis's group investigated a novel inorganic hole conductor based upon $CsSnI_3$[68] (seen in Figure 1.20). The resulting ss-DSSC was comprised of $CsSnI_{2.95}F_{0.05}$ doped with 5% SnF_2, and exhibited an efficiency of over 10%[69]. The enhanced performance was due to an increase in conductivity and hole mobility which also allowed them to thicken the dye region by 10 μm, yielding a better light absorption and increased photocurrent. This remarkable device was the first example of an ss-DSSC whose performance rivals that of a liquid DSSC.

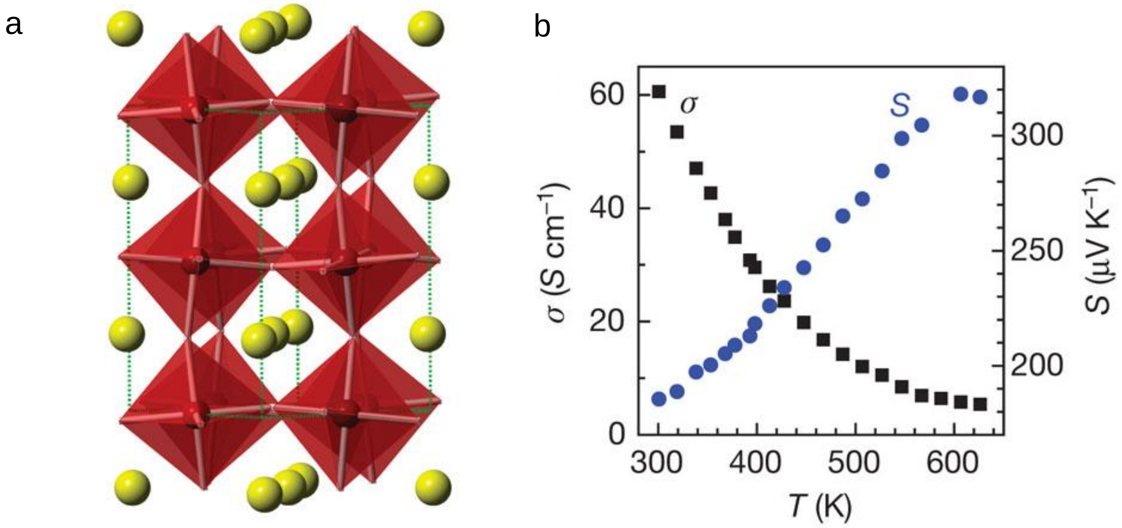

Figure 1.20 (a) Structure of $CsSnI_3$, red polyhedron, $[SnI_{6/2}]^-$; yellow sphere, Cs. (b) Temperature dependence of conductivity (black) and Seebeck coefficient (blue).

So far, organic molecular are the most widely used hole transport materials inss-DSSC. In 1997, Hagen first introduced triaryldiamine-structured TPD (N,N′-Bis(3-methoxylphenyl)-N,N′-diphenylbenzidine) (Figure 1.21) as hole transporters for DSSC systems. The TPD layer has a charge mobility of 10^{-3} cm^2 V^{-1} $S^{-1}$and achieves incident-photon-to-current conversion efficiencies (IPCE) of up to 0.2%[70]. The introduction of this material stimulated further interest in triphenylamine based ss-DSSCs. The first efficient triphenylamine based ss-DSSCs was reported in 1998 by Udo Bach, who used 2, 2’, 7, 7’ -tetrakis (N, N-di-p-methoxyphenylamine) 9, 9’-spirobifluorene (spiro-MeOTAD) (Figure 1.21) as the HTM. Using antimony and lithium salts as additives, they reported efficiencies under white light as high as 0.7% with a peak IPCE of 33%[14].

Currently, spiro-MeOTAD is the most successful and widely used organic HTM, with reported efficiencies of up to 7.2%[48].

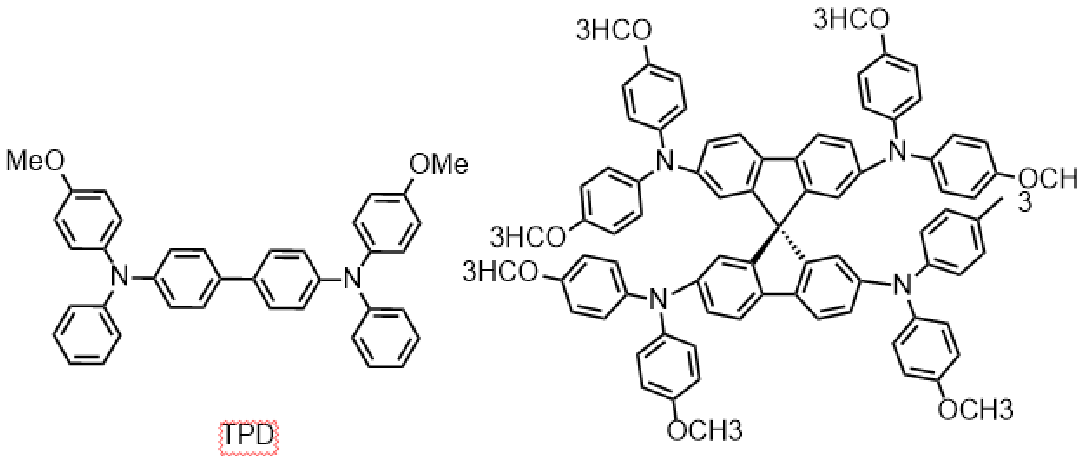

TPD

Spiro-MeOTAD

Figure 1.21 Structure of TPD (left) and Spiro-MeOTAD (right).

To improve the HTM interpenetration into the TiO_2 pore structure, Sellinger et al. designed new organic HTMs (AS 37 and AS 44, seen in Figure 1.22) with a low glass transition temperature (T_g) and a high solubility in organic solvent[71]. They attempted to mimic the structure of sprio-MeOTAD, while reducing the cost, by using half structure of spiro-MeOTAD with a longer alky chain attached to the carbozole or fluorene unit. Using a Z907 Dye, the cells based on AS 37 and AS 44 demonstrated an efficiency of 3%, comparable to the performance of conventional spiro-MeOTAD cells. The smaller size of AS 37 and AS 44, their excellent solubility and low T_g allowed superior interpenetration of the HTM within the porous nc-TiO_2. Increasing the width of the dye-laden TiO_2 by 6 μm yielded an ss-DSSC whose performance exceeded that of spiro-MeOTAD, suggesting possible future avenues for the fabrication of higher efficiency DSSC cells. Other examples of HTM[46,72-74] have been explored in the past decade with their own advantages, such as low cost, efficient deposition or high hole mobility.

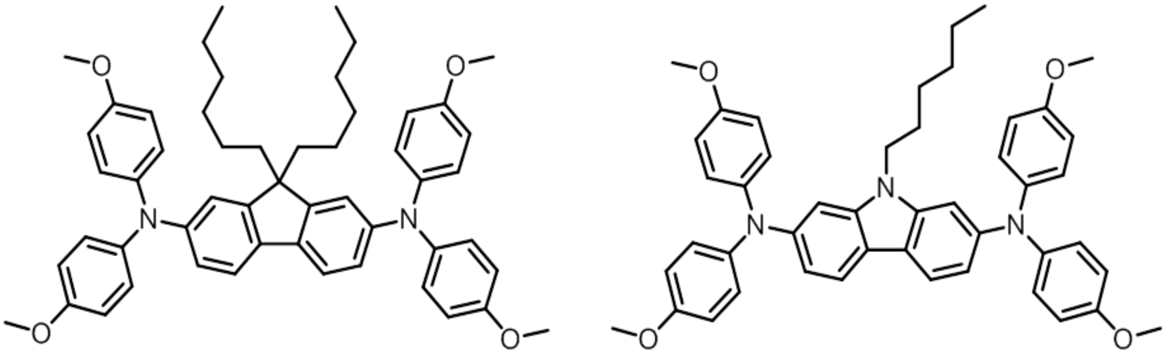

AS37 AS 44

Figure 1.22 Structure of novel HTMs, AS 37 and AS 44

Conjugated polymeric hole conductors comprise the biggest branch of HTMs used in the application of ss-DSSC. Their popularity is due to their better hole mobility, which arises from their conjugated structure, and their higher stability, which arises from their rigid polymer backbone, and their lower cost. Yanagida's group developed polypyrrole (PPy) as a HTM for ss-DSSC in 1997[75]. They used photo-eletrodepositon to generate the polymer within the porous regions of the TiO_2. The cell demonstrated an efficiency of 0.1% at low light density but had a good open circuit voltage of 0.67 V, indicating a low recombination and back-reaction rate. Further progress with this system has mainly focused on replacing the counter electrode[76] or replacing the N3 dye with a substitute[77]. However, the efficiency of this type of ss-DSSC based on PPy has not yet exceeded 1%. Tan's group has studied polyaniline (PANI), another conjugated system. They spin-coating a PANI solution onto a ruthenium dye sensitized TiO_2 film, but the device showed an extremely low current signal[78]. They subsequently added t-butyl pyridine (tBP) to enhance the conductivity and used in-situ polymerization to better infiltrate the PANI into the porous TiO_2, there-by reaching an efficiency of 1.1%[79,80].However the triarylamine moiety, discussed in the previous paragraph, has yielded the best results to date; still its efficiency is limited by its low hole mobility and limited stability. People have tried to oligomerize the triarylamine derivative to enhance the carrier mobility. Schimidt-Mende[81] and Kroeze[82] designed a series of oligomers of triarylamine which showed efficiencies of up to 2.0%. They compared the pore-filling properties of these oligomers with that of spiro-MeOTAD, and found that the wetting behavior of the oligomer was poorer than that of the smaller molecule, spiro-MeOTAD. Indeed the wettability corresponded very closely to the hole transfer yield and the cell's overall performance. Attempts have been made to polymerize the styrene-like triarylamine without a conjugated structure but these efforts have not surmounted the problem of incomplete pore filling. Jiang[83] prepared a new HTM using poly(4-vinylphenyloxymethyltriphenylamine) doped with LiSCN and imidazolium ionic liquid. Under one full sun illumination, the cell showed an efficiency of 0.6%. However this cell contains ionic liquid, and hence is not strictly a solid state cell. Another example reported an amphiphilic block copolymer as HTM, poly(ethylene oxide)-b-poly-(triphenylamine) (PEO-PTPA)[84]. The active layer was prepared by dissolving the block copolymer, PEO-PTPA, and a Z907 dye in DMF. After addition of HNO_3 and a titanium precursor, the mixture was heated to 90°C and spin-coated onto the FTO substrate. This single step fabrication yield an efficiency of up to 0.15% at 1 Sun.

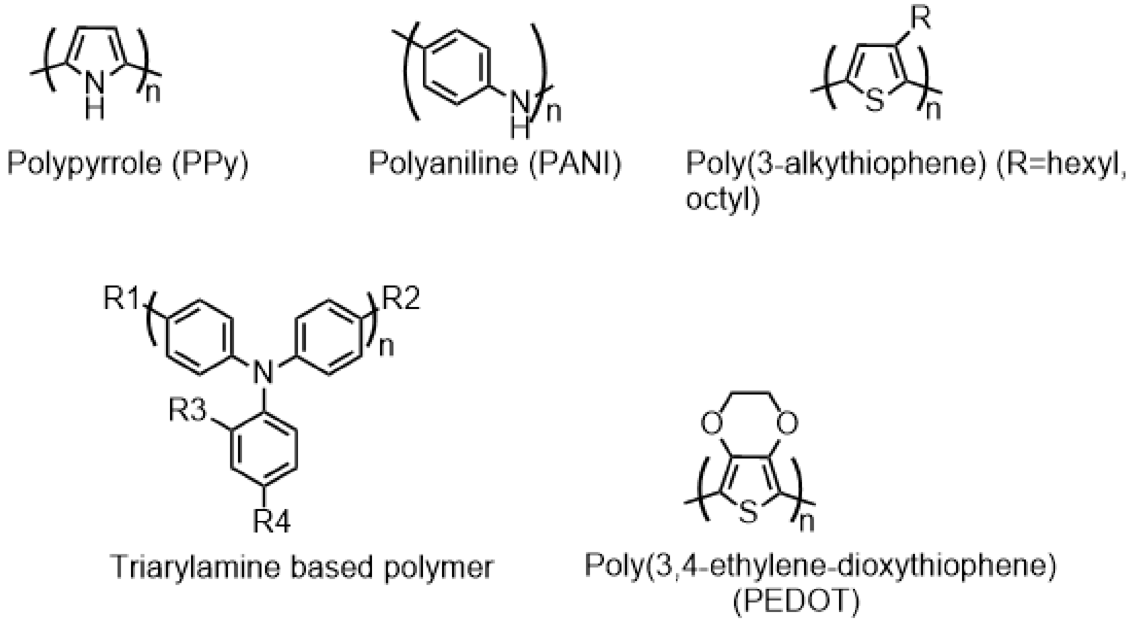

Figure 1.23 Different structures of conjugated polymers used as HTM in ss-DSSC

Polythiophene is another conjugated HTM that has played an important role in the development of ss-DSSC.   Polythiophene was introduced as a HTM in 2002 in a cell with a meager efficiency of 0.012%, however after only one decade of effort, recent cells have demonstrated efficiencies as high as 6%. Two main types of polythiophene are used in ss-DSSCs. One type is poly(3-alkylthiophene), particularly poly(3-hexylthiophene) (P3HT) and poly(3-octylthiophene) (P3OT). Initial reports[85-87] of ss-DSSC with poly(3-alkylthiophene) gave efficiency less than 1% due to the use of an unsuitable sensitizer and poor pore filling of the polymer into the TiO_2. By optimizing cell's thickness, a P3OT-based cell using N719 dye achieved an efficiency of over 1%[88], while a P3HT-based cell using an organic dye yielded an efficiency of 2.6%[89] by optimizing the Lithium salt treatment and the interaction of the HTM with the organic dye. Subsequently, significant effort on P3HT ss-DSSCs has focused replacing the ruthenium dye with indoline dye[65] or quantum dots[90], whose scattering effects enhance the absorption of photons from incident light. Chang et al. developed an Sb_2S_3-TiO_2/P3HT heterojunction solar cell, using Sb_2S_3 used as the photosensitizer and P3HT as the HTM[90]. They achieved a power efficiency of over 5% with a maximum IPCE of 80% under one full sun illumination. This encouraging result is competitive with the performance of spiro-MeOTAD based cells.

Poly(styrenesulfonate) poly(3,4-ethylenedioxythiophene) (PEDOT/PSS). PEDOT: PSS is another alternative to polythiophene that features high conductivity, high transparency, and excellent stability compared to P3HT and P3OT. Yanagida's group polymerized ethylenedioxythiophene (EDOT) through an oxidative polymerization[91], and added tBP and lithium salts to improve the polymer-dye contact and conductivity. Unfortunately, significantly charge recombination and poor dye regeneration lead to a meager efficiency of 0.012%. They next turned to in-situ photoelectrochemical polymerization, so that the polymerization took place within the pores of TiO2, yielding perfect contact with dye molecule. This effective deposition method yielded a 50-fold improvement of the overall cell efficiency[92]. This group subsequently studied the anion effect of lithium salts and employed bis-trifluoromethanesulfonyl imide ($TFSI^-$) to enhance the photocurrent[63]. Yanagida's group also replaced the Z907 dye, often used in the spiro-MeOTAD system, with a D149 dye which showed a broader absorbance in visible spectrum and lower charge recombination in the PEDOT system, leading to a record efficiency of 6.1%[64]. Recently, a PEDOT-based ss-DSSC with a 7.1% efficiency was achieved via a graft copolymer-templated, mesoporous TiO_2 film with a large surface area using spindle-shaped nanoparticles and solid PEDOT in-situ thermal polymerized[93]. This inspiring result indicates that PEDOTs have great potential as HTMs in highly efficient ss-DSSC.

Counter electrode

The counter electrode is responsible for the injection of electrons from the outer circuit back into the electrolyte or the HTMs. Commonly, in liquid DSSC systems, the counter electrode is formed from platinum (Pt) which has been thermally deposited from a solution of an organo-platinum compound. In solid cells, the counter electrode should form a good ohmic contact with HTM, be highly reflective, and electrochemically stable. The most common technique is to deposit a30-200 nm thick layer of gold[14] or silver[50] to form the counter electrode for spiro-MeOTAD or PEDOT-based cells. Ss-DSSC with gold electrodes can perform reasonably well even in the absence of a spiro-MeOTAD overlayer due to a Schottky contact at the Gold/TiO_2interface. However, a silver/TiO_2 interface displays a shunting behavior, and it is necessary to include a spiro-MeOTAD overlayer in a silver-based device.

Other Organic photovoltaic cell (OPVC)

The polymer solar cell, another type of OPVC, has developed rapidly during the same period and has showed similar gains in power conversion efficiency. The polymer solar cell has an active layer comprised of a blend of donor and acceptor materials. These cells have several differences in their working principles, architecture, and fabrication as compared to DSSCs:

1st, polymer solar cells absorb photons and form an exciton which must diffuse to the interface between the donor and acceptor, where the exiciton is separated into an electron and a hole. Both the absorption rates of the donor (P3HT) and of the acceptor (PCBM, Phenyl-C61-butyric acid methyl ester) will influence the photocurrent generated. Conversely in ss-DSSC, a dye is required which serves as a mediator to generate the electron with the electrons transporting by TiO_2 semiconductor. Subsequently the dye mediator is regenerated by the HTM (donor).

2nd, polymer solar cells obtain their bulk heterojunction (BHJ) structure via a polymer-phase separation process. (see Figure 1.24).The BHJ structure is formed from mixing the donor and acceptor together in a blend of organic solvents before deposition. The resulting heterojunction structure is deposited on an ITO/PEDOT substrate (see Figure 1.24) after the solvent blend has evaporated. The phase-separated structure of the BHJ cell enhances the interfacial area between donor and acceptor in the typically 100nm thick active layer. Conversely ss-DSSCs cells are typically 2-3μm thick and the surface-rich porous TiO_2/Dye structure must be back-filled with HTM. The infiltration of the HTM into the pre-existing TiO_2nano-porous structure is a major road-block to achieving optimal performance in ss-DSSCs.

3rd, while the fabrication of polymer cells requires fewer steps, it must be performed in an oxygen-free atmosphere since the thiophene unit from P3HT is easily oxidized.

REFERENCES

REFERENCES

(1) http://www.iea.org/textbase/pm/glossary.asp, 2002.

(2) Siemens, W.: *Van Nostrand's Eng. Mag.* **1885**, *32*, 392

(3) http://en.wikipedia.org/wiki/Timeline_of_solar_cells, 2012.

(4) Wronski, C. R.: In *Conference Record of the 28th IEEE Photovoltaic Specialists Conference, Anchorage, AK*; IEEE: New York, 2000; pp 1.

(5) Dennler, G.; Scharber, M. C.; Brabec, C. J.: Polymer-Fullerene Bulk-Heterojunction Solar Cells. *Adv Mater* **2009**, *21*, 1323-1338.

(6) Oregan, B.; Gratzel, M.: A Low-Cost, High-Efficiency Solar-Cell Based on Dye-Sensitized Colloidal Tio2 Films. *Nature* **1991**, *353*, 737-740.

(7) Yella, A.; Lee, H. W.; Tsao, H. N.; Yi, C. Y.; Chandiran, A. K.; Nazeeruddin, M. K.; Diau, E. W. G.; Yeh, C. Y.; Zakeeruddin, S. M.; Gratzel, M.: Porphyrin-Sensitized Solar Cells with Cobalt (II/III)-Based Redox Electrolyte Exceed 12 Percent Efficiency. *Science* **2011**, *334*, 629-634.

(8) Nogueira, A. F.; Alonso-Vante, N.; De Paoli, M. A.: Solid-state photoelectrochemical device using poly(o-methoxy aniline) as sensitizer and an ionic conductive elastomer as electrolyte. *Synthetic Met* **1999**, *105*, 23-27.

(9) Wang, L.; Fang, S. B.; Lin, Y.; Zhou, X. W.; Li, M. Y.: A 7.72% efficient dye sensitized solar cell based on novel necklace-like polymer gel electrolyte containing latent chemically cross-linked gel electrolyte precursors. *Chem Commun* **2005**, 5687-5689.

(10) Zakeeruddin, S. M.; Gratzel, M.: Solvent-Free Ionic Liquid Electrolytes for Mesoscopic Dye-Sensitized Solar Cells. *Adv Funct Mater* **2009**, *19*, 2187-2202.

(11) Gorlov, M.; Kloo, L.: Ionic liquid electrolytes for dye-sensitized solar cells. *Dalton T* **2008**, 2655-2666.

(12) Wang, P.; Wenger, B.; Humphry-Baker, R.; Moser, J. E.; Teuscher, J.; Kantlehner, W.; Mezger, J.; Stoyanov, E. V.; Zakeeruddin, S. M.; Gratzel, M.: Charge separation and efficient light energy conversion in sensitized mesoscopic solar cells based on binary ionic liquids. *J Am Chem Soc* **2005**, *127*, 6850-6856.

(13) Bai, Y.; Cao, Y. M.; Zhang, J.; Wang, M.; Li, R. Z.; Wang, P.; Zakeeruddin, S. M.; Gratzel, M.: High-performance dye-sensitized solar cells based on solvent-free electrolytes produced from eutectic melts. *Nat Mater* **2008**, *7*, 626-630.

(14) Bach, U.; Lupo, D.; Comte, P.; Moser, J. E.; Weissortel, F.; Salbeck, J.; Spreitzer, H.; Gratzel, M.: Solid-state dye-sensitized mesoporous TiO2 solar cells with high photon-to-electron conversion efficiencies. *Nature* **1998**, *395*, 583-585.

(15) Fabregat-Santiagoa, F.; Bisquert, J.; Palomares, E.; Haque, S. A.; Durrant, J. R.: Impedance spectroscopy study of dye-sensitized solar cells with undoped spiro-OMeTAD as hole conductor. *J Appl Phys* **2006**, *100*.

(16) Wang, X.; Zhi, L. J.; Mullen, K.: Transparent, conductive graphene electrodes for dye-sensitized solar cells. *Nano Lett* **2008**, *8*, 323-327.

(17) Bach, U.: *PhD. Thesis. EPFL* **2000**.

(18) Yu, H.; Zhang, S. Q.; Zhao, H. J.; Will, G.; Liu, P. R.: An efficient and low-cost TiO2 compact layer for performance improvement of dye-sensitized solar cells. *Electrochim Acta* **2009**, *54*, 1319-1324.

(19) Lellig, P.; Niedermeier, M. A.; Rawolle, M.; Meister, M.; Laquai, F.; Muller-Buschbaum, P.; Gutmann, J. S.: Comparative study of conventional and hybrid blocking layers for solid-state dye-sensitized solar cells. *Phys Chem Chem Phys* **2012**, *14*, 1607-1613.

(20) Hamann, T. W.; Farha, O. K.; Hupp, J. T.: Outer-Sphere Redox Couples as Shuttles in Dye-Sensitized Solar Cells. Performance Enhancement Based on Photoelectrode Modification via Atomic Layer Deposition. *J Phys Chem C* **2008**, *112*, 19756-19764.

(21) Kavan, L.; Gratzel, M.: Highly Efficient Semiconducting Tio2 Photoelectrodes Prepared by Aerosol Pyrolysis. *Electrochim Acta* **1995**, *40*, 643-652.

(22) Peng, B.; Jungmann, G.; Jager, C.; Haarer, D.; Schmidt, H. W.; Thelakkat, M.: Systematic investigation of the role of compact TiO2 layer in solid state dye-sensitized TiO2 solar cells. *Coordin Chem Rev* **2004**, *248*, 1479-1489.

(23) Ito, S.; Murakami, T. N.; Comte, P.; Liska, P.; Gratzel, C.; Nazeeruddin, M. K.; Gratzel, M.: Fabrication of thin film dye sensitized solar cells with solar to electric power conversion efficiency over 10%. *Thin Solid Films* **2008**, *516*, 4613-4619.

(24) Ito, S.; Kitamura, T.; Wada, Y.; Yanagida, S.: Facile fabrication of mesoporous TiO2 electrodes for dye solar cells: chemical modification and repetitive coating. *Sol Energ Mat Sol C* **2003**, *76*, 3-13.

(25) Ito, S.; Chen, P.; Comte, P.; Nazeeruddin, M. K.; Liska, P.; Pechy, P.; Gratzel, M.: Fabrication of screen-printing pastes from TiO2 powders for dye-sensitised solar cells. *Prog Photovoltaics* **2007**, *15*, 603-612.

(26) Barbe, C. J.; Arendse, F.; Comte, P.; Jirousek, M.; Lenzmann, F.; Shklover, V.; Gratzel, M.: Nanocrystalline titanium oxide electrodes for photovoltaic applications. *J Am Ceram Soc* **1997**, *80*, 3157-3171.

(27) Jeong, N. C.; Farha, O. K.; Hupp, J. T.: A Convenient Route to High Area, Nanoparticulate TiO2 Photoelectrodes Suitable for High-Efficiency Energy Conversion in Dye-Sensitized Solar Cells. *Langmuir* **2011**, *27*, 1996-1999.

(28) Chen, P.; Brillet, J.; Bala, H.; Wang, P.; Zakeeruddin, S. M.; Gratzel, M.: Solid-state dye-sensitized solar cells using TiO2 nanotube arrays on FTO glass. *J Mater Chem* **2009**, *19*, 5325-5328.

(29) Wang, M. K.; Bai, J.; Le Formal, F.; Moon, S. J.; Cevey-Ha, L.; Humphry-Baker, R.; Gratzel, C.; Zakeeruddin, S. M.; Gratzel, M.: Solid-State Dye-Sensitized Solar Cells using Ordered TiO2 Nanorods on Transparent Conductive Oxide as Photoanodes. *J Phys Chem C* **2012**, *116*, 3266-3273.

(30) Zukalova, M.; Zukal, A.; Kavan, L.; Nazeeruddin, M. K.; Liska, P.; Gratzel, M.: Organized mesoporous TiO2 films exhibiting greatly enhanced performance in dye-sensitized solar cells. *Nano Lett* **2005**, *5*, 1789-1792.

(31) Lancelle-Beltran, E.; Prene, P.; Boscher, C.; Belleville, P.; Buvat, P.; Lambert, S.; Guillet, F.; Boissiere, C.; Grosso, D.; Sanchez, C.: Nanostructured hybrid solar cells based on self-assembled mesoporous titania thin films. *Chem Mater* **2006**, *18*, 6152-6156.

(32) Docampo, P.; Guldin, S.; Stefik, M.; Tiwana, P.; Orilall, M. C.; Huttner, S.; Sai, H.; Wiesner, U.; Steiner, U.; Snaith, H. J.: Control of Solid-State Dye-Sensitized Solar Cell Performance by Block-Copolymer-Directed TiO2 Synthesis. *Adv Funct Mater* **2010**, *20*, 1787-1796.

(33) Guldin, S.; Docampo, P.; Stefik, M.; Kamita, G.; Wiesner, U.; Snaith, H. J.; Steiner, U.: Layer-by-Layer Formation of Block-Copolymer-Derived TiO2 for Solid-State Dye-Sensitized Solar Cells. *Small* **2012**, *8*, 432-440.

(34) Docampo, P.; Stefik, M.; Guldin, S.; Gunning, R.; Yufa, N. A.; Cai, N.; Wang, P.; Steiner, U.; Wiesner, U.; Snaith, H. J.: Triblock-Terpolymer-Directed Self-Assembly of Mesoporous TiO2: High-Performance Photoanodes for Solid-State Dye-Sensitized Solar Cells. *Adv Energy Mater* **2012**, *2*, 676-682.

(35) Plank, N. O. V.; Howard, I.; Rao, A.; Wilson, M. W. B.; Ducati, C.; Mane, R. S.; Bendall, J. S.; Louca, R. R. M.; Greenham, N. C.; Miura, H.; Friend, R. H.;

Snaith, H. J.; Welland, M. E.: Efficient ZnO Nanowire Solid-State Dye-Sensitized Solar Cells Using Organic Dyes and Core-shell Nanostructures. *J Phys Chem C* **2009**, *113*, 18515-18522.

(36) Desai, U. V.; Xu, C. K.; Wu, J. M.; Gao, D.: Solid-state dye-sensitized solar cells based on ordered ZnO nanowire arrays. *Nanotechnology* **2012**, *23*.

(37) Xu, C. K.; Wu, J. M.; Desai, U. V.; Gao, D.: High-Efficiency Solid-State Dye-Sensitized Solar Cells Based on TiO2-Coated ZnO Nanowire Arrays. *Nano Lett* **2012**, *12*, 2420-2424.

(38) Boucharef, M.; Di Bin, C.; Boumaza, M. S.; Colas, M.; Snaith, H. J.; Ratier, B.; Boucle, J.: Solid-state dye-sensitized solar cells based on ZnO nanocrystals. *Nanotechnology* **2010**, *21*.

(39) Docampo, P.; Snaith, H. J.: Obviating the requirement for oxygen in SnO2-based solid-state dye-sensitized solar cells. *Nanotechnology* **2011**, *22*.

(40) Qin, Y. C.; Peng, Q.: Ruthenium Sensitizers and Their Applications in Dye-Sensitized Solar Cells. *Int J Photoenergy* **2012**.

(41) Nazeeruddin, M. K.; De Angelis, F.; Fantacci, S.; Selloni, A.; Viscardi, G.; Liska, P.; Ito, S.; Bessho, T.; Gratzel, M.: Combined experimental and DFT-TDDFT computational study of photoelectrochemical cell ruthenium sensitizers. *J Am Chem Soc* **2005**, *127*, 16835-16847.

(42) Hagfeldt, A.; Boschloo, G.; Sun, L. C.; Kloo, L.; Pettersson, H.: Dye-Sensitized Solar Cells. *Chem Rev* **2010**, *110*, 6595-6663.

(43) Mishra, A.; Fischer, M. K. R.; Bauerle, P.: Metal-Free Organic Dyes for Dye-Sensitized Solar Cells: From Structure: Property Relationships to Design Rules. *Angew Chem Int Edit* **2009**, *48*, 2474-2499.

(44) Snaith, H. J.; Petrozza, A.; Ito, S.; Miura, H.; Gratzel, M.: Charge Generation and Photovoltaic Operation of Solid-State Dye-Sensitized Solar Cells Incorporating a High Extinction Coefficient Indolene-Based Sensitizer. *Adv Funct Mater* **2009**, *19*, 1810-1818.

(45) Cappel, U. B.; Daeneke, T.; Bach, U.: Oxygen-Induced Doping of Spiro-MeOTAD in Solid-State Dye-Sensitized Solar Cells and Its Impact on Device Performance. *Nano Lett* **2012**.

(46) Unger, E. L.; Morandeira, A.; Persson, M.; Zietz, B.; Ripaud, E.; Leriche, P.; Roncali, J.; Hagfeldt, A.; Boschloo, G.: Contribution from a hole-conducting dye to the photocurrent in solid-state dye-sensitized solar cells. *Phys Chem Chem Phys* **2011**, *13*, 20172-20177.

(47) Burschka, J.; Dualeh, A.; Kessler, F.; Baranoff, E.; Cevey-Ha, N. L.; Yi, C. Y.; Nazeeruddin, M. K.; Gratzel, M.: Tris(2-(1H-pyrazol-1-yl)pyridine)cobalt(III) as p-Type Dopant for Organic Semiconductors and Its Application in Highly Efficient Solid-State Dye-Sensitized Solar Cells. *J Am Chem Soc* **2011**, *133*, 18042-18045.

(48) Cai, N.; Moon, S. J.; Cevey-Ha, L.; Moehl, T.; Humphry-Baker, R.; Wang, P.; Zakeeruddin, S. M.; Gratzel, M.: An Organic D-pi-A Dye for Record Efficiency Solid-State Sensitized Heterojunction Solar Cells. *Nano Lett* **2011**, *11*, 1452-1456.

(49) Schmidt-Mende, L.; Zakeeruddin, S. M.; Gratzel, M.: Efficiency improvement in solid-state-dye-sensitized photovoltaics with an amphiphilic Ruthenium-dye. *Appl Phys Lett* **2005**, *86*.

(50) Snaith, H. J.; Moule, A. J.; Klein, C.; Meerholz, K.; Friend, R. H.; Gratzel, M.: Efficiency enhancements in solid-state hybrid solar cells via reduced charge recombination and increased light capture. *Nano Lett* **2007**, *7*, 3372-3376.

(51) Yang, Z. S.; Chen, C. Y.; Roy, P.; Chang, H. T.: Quantum dot-sensitized solar cells incorporating nanomaterials. *Chem Commun* **2011**, *47*, 9561-9571.

(52) Ruhle, S.; Shalom, M.; Zaban, A.: Quantum-Dot-Sensitized Solar Cells. *Chemphyschem* **2010**, *11*, 2290-2304.

(53) Mora-Sero, I.; Bisquert, J.: Breakthroughs in the Development of Semiconductor-Sensitized Solar Cells. *J Phys Chem Lett* **2010**, *1*, 3046-3052.

(54) Lee, H.; Leventis, H. C.; Moon, S.-J.; Chen, P.; Ito, S.; Haque, S. A.; Torres, T.; Nüesch, F.; Geiger, T.; Zakeeruddin, S. M.; Grätzel, M.; Nazeeruddin, M. K.: PbS and CdS Quantum Dot-Sensitized Solid-State Solar Cells: “Old Concepts, New Results”. *Adv Funct Mater* **2009**, *19*, 2735-2742.

(55) Ardalan, P.; Brennan, T. P.; Lee, H. B. R.; Bakke, J. R.; Ding, I. K.; McGehee, M. D.; Bent, S. F.: Effects of Self-Assembled Monolayers on Solid-State CdS Quantum Dot Sensitized Solar Cells. *Acs Nano* **2011**, *5*, 1495-1504.

(56) Brennan, T. P.; Ardalan, P.; Lee, H. B. R.; Bakke, J. R.; Ding, I. K.; McGehee, M. D.; Bent, S. F.: Atomic Layer Deposition of CdS Quantum Dots for Solid-State Quantum Dot Sensitized Solar Cells. *Adv Energy Mater* **2011**, *1*, 1169-1175.

(57) Lee, H.; Wang, M. K.; Chen, P.; Gamelin, D. R.; Zakeeruddin, S. M.; Gratzel, M.; Nazeeruddin, M. K.: Efficient CdSe Quantum Dot-Sensitized Solar Cells Prepared by an Improved Successive Ionic Layer Adsorption and Reaction Process. *Nano Lett* **2009**, *9*, 4221-4227.

(58) Moon, S. J.; Itzhaik, Y.; Yum, J. H.; Zakeeruddin, S. M.; Hodes, G.; Gratzel, M.: Sb2S3-Based Mesoscopic Solar Cell using an Organic Hole Conductor. *J Phys Chem Lett* **2010**, *1*, 1524-1527.

(59) Tennakone, K.; Kumara, G. R. R. A.; Kumarasinghe, A. R.; Wijayantha, K. G. U.; Sirimanne, P. M.: A Dye-Sensitized Nano-Porous Solid-State Photovoltaic Cell. *Semicond Sci Tech* **1995**, *10*, 1689-1693.

(60) Meng, Q. B.; Takahashi, K.; Zhang, X. T.; Sutanto, I.; Rao, T. N.; Sato, O.; Fujishima, A.; Watanabe, H.; Nakamori, T.; Uragami, M.: Fabrication of an efficient solid-state dye-sensitized solar cell. *Langmuir* **2003**, *19*, 3572-3574.

(61) Oregan, B.; Schwartz, D. T.: Efficient Photo-Hole Injection from Adsorbed Cyanine Dyes into Electrodeposited Copper(I) Thiocyanate Thin-Films. *Chem Mater* **1995**, *7*, 1349-1354.

(62) Perera, V. P. S.; Senevirathna, M. K. I.; Pitigala, P. K. D. D. P.; Tennakone, K.: Doping CuSCN films for enhancement of conductivity: Application in dye-sensitized solid-state solar cells. *Sol Energ Mat Sol C* **2005**, *86*, 443-450.

(63) Xia, J. B.; Masaki, N.; Lira-Cantu, M.; Kim, Y.; Jiang, K. J.; Yanagida, S.: Influence of doped anions on poly(3,4-ethylenedioxythiophene) as hole conductors for iodine-free solid-state dye-sensitized solar cells. *J Am Chem Soc* **2008**, *130*, 1258-1263.

(64) Liu, X. Z.; Zhang, W.; Uchida, S.; Cai, L. P.; Liu, B.; Ramakrishna, S.: An Efficient Organic-Dye-Sensitized Solar Cell with in situ Polymerized Poly(3,4-ethylenedioxythiophene) as a Hole-Transporting Material. *Adv Mater* **2010**, *22*, E150-+.

(65) Zhang, W.; Zhu, R.; Li, F.; Wang, Q.; Liu, B.: High-Performance Solid-State Organic Dye Sensitized Solar Cells with P3HT as Hole Transporter. *J Phys Chem C* **2011**, *115*, 7038-7043.

(66) Kruger, J.; Plass, R.; Cevey, L.; Piccirelli, M.; Gratzel, M.; Bach, U.: High efficiency solid-state photovoltaic device due to inhibition of interface charge recombination. *Appl Phys Lett* **2001**, *79*, 2085-2087.

(67) Premalal, E. V. A.; Kumara, G. R. R. A.; Rajapakse, R. M. G.; Shimomura, M.; Murakami, K.; Konno, A.: Tuning chemistry of CuSCN to enhance the performance of TiO2/N719/CuSCN all-solid-state dye-sensitized solar cell. *Chem Commun* **2010**, *46*, 3360-3362.

(68) Chung, I.; Song, J. H.; Im, J.; Androulakis, J.; Malliakas, C. D.; Li, H.; Freeman, A. J.; Kenney, J. T.; Kanatzidis, M. G.: CsSnI3: Semiconductor or Metal? High Electrical Conductivity and Strong Near-Infrared Photoluminescence from a

Single Material. High Hole Mobility and Phase-Transitions. *J Am Chem Soc* **2012**, *134*, 8579-8587.

(69) Chung, I.; Lee, B.; He, J. Q.; Chang, R. P. H.; Kanatzidis, M. G.: All-solid-state dye-sensitized solar cells with high efficiency. *Nature* **2012**, *485*, 486-U94.

(70) Hagen, J.; Schaffrath, W.; Otschik, P.; Fink, R.; Bacher, A.; Schmidt, H. W.; Haarer, D.: Novel hybrid solar cells consisting of inorganic nanoparticles and an organic hole transport material. *Synthetic Met* **1997**, *89*, 215-220.

(71) Leijtens, T.; Ding, I. K.; Giovenzana, T.; Bloking, J. T.; McGehee, M. D.; Sellinger, A.: Hole Transport Materials with Low Glass Transition Temperatures and High Solubility for Application in Solid-State Dye-Sensitized Solar Cells. *Acs Nano* **2012**, *6*, 1455-1462.

(72) Zhao, Y.; Chen, W.; Zhai, J.; Sheng, X. L.; He, Q. G.; Wei, T. X.; Bai, F. L.; Jiang, L.; Zhu, D. B.: Solid-state dye-sensitized photovoltaic device with newly designed small organic molecule as hole-conductor. *Chem Phys Lett* **2007**, *445*, 259-264.

(73) Juozapavicius, M.; O'Regan, B. C.; Anderson, A. Y.; Grazulevicius, J. V.; Mimaite, V.: Efficient dye regeneration in solid-state dye-sensitized solar cells fabricated with melt processed hole conductors. *Org Electron* **2012**, *13*, 23-30.

(74) Zhang, K.; Wang, L.; Liang, Y. L.; Yang, S. Q.; Liang, J.; Cheng, F. Y.; Chen, J.: A thermally and electrochemically stable organic hole-transporting material with an adamantane central core and triarylamine moieties. *Synthetic Met* **2012**, *162*, 490-496.

(75) Murakoshi, K.; Kogure, R.; Wada, Y.; Yanagida, S.: Solid state dye-sensitized TiO2 solar cell with polypyrrole as hole transport layer. *Chem Lett* **1997**, 471-472.

(76) Cervini, R.; Cheng, Y. B.; Simon, G.: Solid-state Ru-dye solar cells using polypyrrole as a hole conductor. *J Phys D Appl Phys* **2004**, *37*, 13-20.

(77) Murakoshi, K.; Kogure, R.; Wada, Y.; Yanagida, S.: Fabrication of solid-state dye-sensitized TiO2 solar cells combined with polypyrrole. *Sol Energ Mat Sol C* **1998**, *55*, 113-125.

(78) Tan, S. X.; Zhai, J.; Wan, M. X.; Jiang, L.; Zhu, D. B.: Polyaniline as a hole transport material to prepare solid solar cells. *Synthetic Met* **2003**, *137*, 1511-1512.

(79) Tan, S. X.; Zhai, J.; Wan, M. X.; Meng, Q. B.; Li, Y. L.; Jiang, L.; Zhu, D. B.: Influence of small molecules in conducting polyaniline on the photovoltaic

properties of solid-state dye-sensitized solar cells. *J Phys Chem B* **2004**, *108*, 18693-18697.

(80) Kim, H. S.; Wamser, C. C.: Photoelectropolymerization of aniline in a dye-sensitized solar cell. *Photoch Photobio Sci* **2006**, *5*, 955-960.

(81) Schmidt-Mende, L.; Gratzel, M.: TiO2 pore-filling and its effect on the efficiency of solid-state dye-sensitized solar cells. *Thin Solid Films* **2006**, *500*, 296-301.

(82) Kroeze, J. E.; Hirata, N.; Schmidt-Mende, L.; Orizu, C.; Ogier, S. D.; Carr, K.; Gratzel, M.; Durrant, J. R.: Parameters influencing charge separation in solid-state dye-sensitized solar cells using novel hole conductors. *Adv Funct Mater* **2006**, *16*, 1832-1838.

(83) Jiang, K. J.; Sun, Y. L.; Shao, K. F.; Wang, J. F.; Yang, L. M.: Dye-sensitized TiO2 solid solar cell using poly (4-vinylphenyloxymethyltriphenylamine) as hole transport material. *Chinese Chem Lett* **2003**, *14*, 1093-1096.

(84) Lechmann, M. C.; Kessler, D.; Gutmann, J. S.: Functional Templates for Hybrid Materials with Orthogonal Functionality. *Langmuir* **2009**, *25*, 10202-10208.

(85) Gebeyehu, D.; Brabec, C. J.; Sariciftci, N. S.; Vangeneugden, D.; Kiebooms, R.; Vanderzande, D.; Kienberger, F.; Schindler, H.: Hybrid solar cells based on dye-sensitized nanoporous TiO2 electrodes and conjugated polymers as hole transport materials. *Synthetic Met* **2001**, *125*, 279-287.

(86) Zafer, C.; Karapire, C.; Sariciftci, N. S.; Icli, S.: Characterization of N,N '-bis-2-(1-hydoxy-4-methylpentyl)-3,4,9,10-perylene bis (dicarboximide) sensitized nanocrystalline TiO2 solar cells with polythiophene hole conductors. *Sol Energ Mat Sol C* **2005**, *88*, 11-21.

(87) Wang, M. Q.; Wang, X. G.: P3HT/TiO2 bulk-heterojunction solar cell sensitized by a perylene derivative. *Sol Energ Mat Sol C* **2007**, *91*, 1782-1787.

(88) Prene, P.; Lancelle-Beltran, E.; Boscher, C.; Belleville, P.; Buvat, P.; Sanchez, C.: All-solid-state dye-sensitized nanoporous TiO2 hybrid solar cells with high energy-conversion efficiency. *Adv Mater* **2006**, *18*, 2579-+.

(89) Zhu, R.; Jiang, C. Y.; Liu, B.; Ramakrishna, S.: Highly Efficient Nanoporous TiO2-Polythiophene Hybrid Solar Cells Based on Interfacial Modification Using a Metal-Free Organic Dye. *Adv Mater* **2009**, *21*, 994-+.

(90) Chang, J. A.; Rhee, J. H.; Im, S. H.; Lee, Y. H.; Kim, H. J.; Seok, S. I.; Nazeeruddin, M. K.; Gratzel, M.: High-Performance Nanostructured Inorganic-Organic Heterojunction Solar Cells. *Nano Lett* **2010**, *10*, 2609-2612.
(91) Saito, Y.; Kitamura, T.; Wada, Y.; Yanagida, S.: Poly(3,4-ethylenedioxythiophene) as a hole conductor in solid state dye sensitized solar cells. *Synthetic Met* **2002**, *131*, 185-187.

(92) Saito, Y.; Fukuri, N.; Senadeera, R.; Kitamura, T.; Wada, Y.; Yanagida, S.: Solid state dye sensitized solar cells using in situ polymerized PEDOTs as hole conductor. *Electrochem Commun* **2004**, *6*, 71-74.

(93) Ahn, S. H.; Chi, W. S.; Park, J. T.; Koh, J. K.; Roh, D. K.; Kim, J. H.: Direct Assembly of Preformed Nanoparticles and Graft Copolymer for the Fabrication of Micrometer-thick, Organized TiO2 Films: High Efficiency Solid-state Dye-sensitized Solar Cells. *Adv Mater* **2012**, *24*, 519.

Chapter 2: Spiro-MeOTAD

Introduction:

Spiro-MeOTAD, more precisely 2, 2’, 7, 7’ -tetrakis (N, N-di-p-methoxyphenylamine) 9, 9’-spirobifluorene, is the most widely used hole-transport material (HTM) used in the fabrication of ss-DSSC[1]. This polymer, first designed and synthesized by Salbeck and coworkers[2], is comprised of two identical π systems connected by a sp^3-hybridized carbon atom, see Figure 2.1. Each π system contains two triarylamine units which facilitate the hole transportation. It is important that the structure have a spiro center, which serves to control the molecule’s organization and film’s morphology. One of the major limited factors of efficiency in ss-DSSC is the degree of interpenetration of the spiro-MeOTAD into pore structure of the mesoporous TiO_2[3,4]. Complete pore-filling enhances the interfacial contact between the dye molecule and the HTM molecule, which allows efficient regeneration of the reduced dye molecules. To increase the interpenetration and obtain a spatially homogeneous thin film, it is desirable to introduce the HTM in an amorphous state so as to prevent the formation of grain boundaries. If polycrystalline thin films within the mesoporous TiO_2 region of the ss-DSSC, then traps may develop along the interfaces of the crystal domains; these traps inhibit hole transport and lower the cell’s performance. The perpendicular arrangement of the two π system units within spiro-MeOTAD serves to efficiently suppress molecular interactions and inhibits recrystallization. Because of aromatic structure, the good physical stability of the spiro-MeOTAD structure also serves to prevent its degradation under illumination. The glass transition temperature, T_g, of a polymer is a key characterization of the physical stability of its amorphous state; when the amorphous-state material is heated beyond T_g, the excited molecular motion permits the polymer chains to slide more effectively, and often permits them to relax into a more crystalline state. It has been observed that molecules with a symmetric spiro-structure, larger molecular weight, and smaller intermolecular interaction have a more stable amorphous state, and a higher glass transition temperature[5,6].

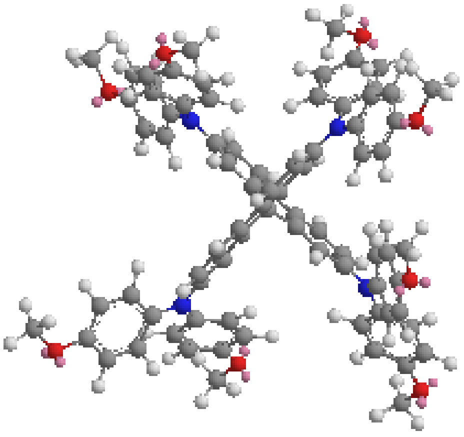

Figure 2.1 The dual-π structure of spiro-MeOTAD and a 3D representation of this structure (from Chemdraw 13.0 via MM2 calculation)

Currently spiro-MeOTAD is available commercially and is widely used in the fabrication of ss-DSSCs. However its price, roughly $1000/gram from its two dominant suppliers, Merck and Lumtech, limits its usage to small-scale research conducted in laboratory or industrial settings. Moreover, a detailed, unambiguous description of the synthesis of spiro-MeOTAD has never been presented in the literature. In this chapter, we describe the developed synthetic route of spiro-MeOTAD in our lab and the characterization of its optical and thermal properties. This chapter forms the basis for the following chapters in this thesis, from fabrication and optimization of ss-DSSC to synthesis of novel HTMs that replace spiro-MeOTAD.

Results and Discussion

Synthesis of spiro-MeOTAD

The plan for the synthesis of spiro-MeOTAD is shown in Figure 2.2. From the symmetry of its molecular structure, the four triarylamines units could be formed by a C-N coupling reaction in one step. The two fragements, Bis (4-methoxyphenylamine) (**3**) and 2, 2’, 7, 7’-tetrabromo-9, 9’spirobifluorene (**8**), are synthesized first. Bis (4-methoxyphenylamine) is readily prepared in a single step starting from the commercially available 4-iodoanisole (**1**) and p-anisidine (**2**). Ullmann-type aryl amination was used to form the C-N bond using CuI/L-proline as the catalyst[7]. By this copper-catalyzed amination procedure, the product could be obtained in a mild condition at a lower cost than a one would via a typical Pd-catalyzed Buchwald-Hartwig reaction. Another key compound, 2, 2’, 7, 7’-tetrabromo-9, 9’spirobifluorene (**8**) was synthesized via a four step procedure[8].

The first step is to convert 2-aminobiphenyl to the corresponding iodide derivative via a Sandmeyer reaction, followed by a Grignard reaction with 9-fluorenone. An acid treatment to finish the spiro structure is followed by a full bromination catalyzed via $FeCl_3$; this yields the target compound **8**. Each step of the reaction gave an acceptable yield with the exception of the Grignard reaction depicted in Figure 2.4. This step gave a yield with 74%, even with enhanced attention to moisture that may have been introduced into the Grignard system either from the N_2 line or from the starting materials.

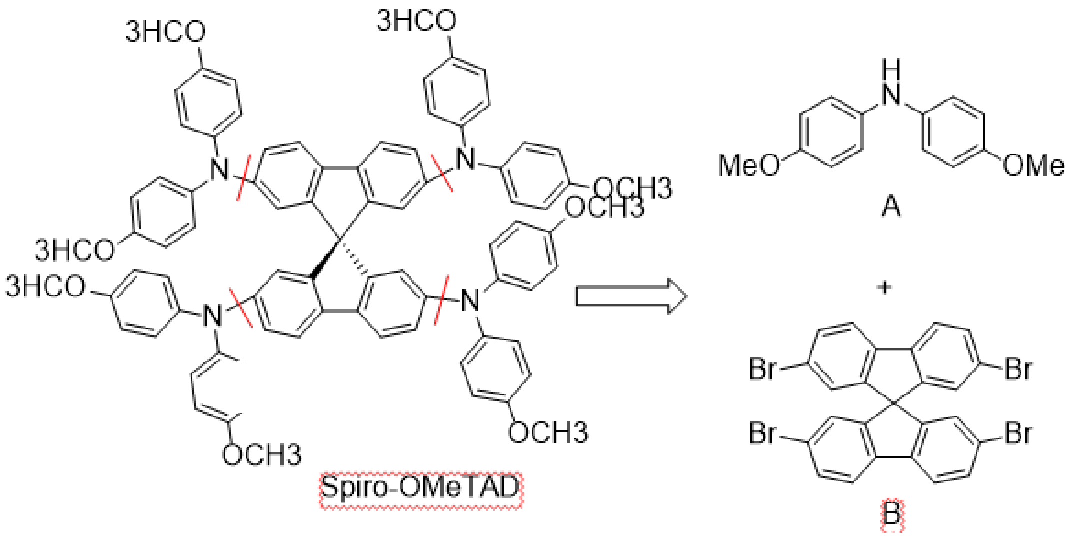

Figure 2.2 Retrosynthetic analysis of spiro-MeOTAD

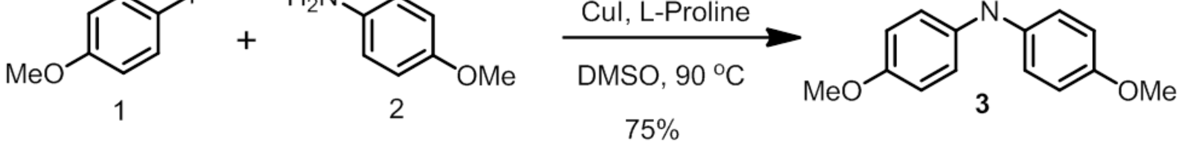

Figure 2.3 Synthesis of bis (4-methoxyphenylamine)

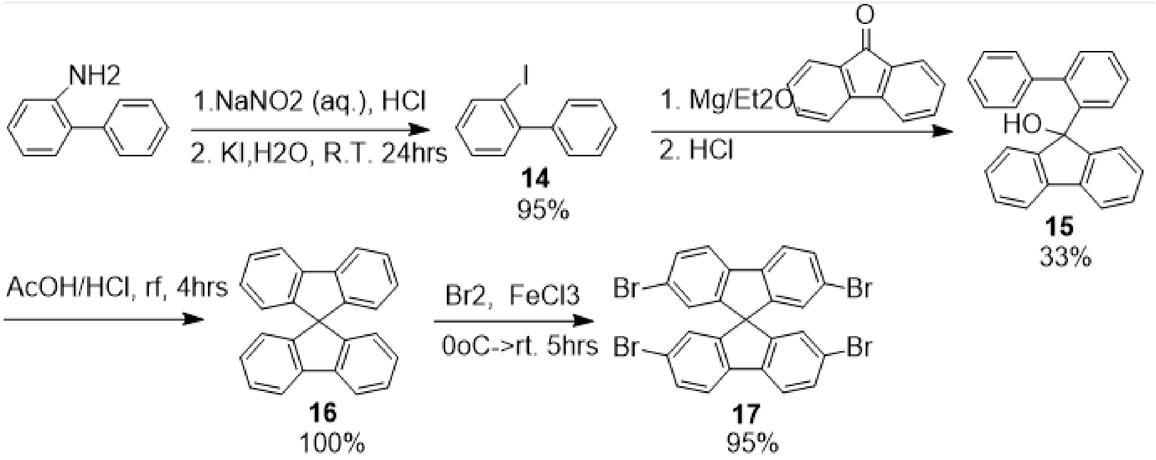

Figure 2.4 Synthesis of tetrabromo-9, 9’spirobifluorene and spiro-MeOTAD

The key step in the synthesis of spiro-MeOTAD is the amination through a metal-catalyzed cross-coupling reaction. This step is generally finished by the reaction of the aryl halide with the secondary amine using a copper or a palladium system. My initial trial was based on a Cu/crown ether catalyzed couple (see Table 2.1, entry 1). This reaction required temperatures of over 140 ℃. Unfortunately, even under these extreme conditions the reaction produced no measureable yield. Subsequently, as an alternative to the copper system, a more active palladium/phosphine system was employed in this reaction. a variety of common catalyst/ligand combinations has been tried until determining that the most efficient way to manufacture spiro-MeOTAD was via a system of Tris (dibenzylideneacetone) dipalladium (Pd_2dba_3) combined with tri-tert-butylphosphine ($P(t\text{-}Bu)_3$) ligand. This catalyst/ligand system offered the highest yield for this key reaction step (as shown in Table 2.1, entry 7). Indeed, an optimal yield of 85% was obtained at a mole ratio of catalyst and ligand of 1:6. Claims in the literature suggested that a Pd(II) catalyst with a $P(t\text{-}Bu)_2Cl$ ligand could provide a yield of over 90%[9], but it seemed not good in my synthesis. A synthesis with a five-gram yield is now routinely achieved in our lab. To verify the end-product, Proton NMR spectra were taken and a comparison made between the lab-made spiro-MeOTAD and the spiro-MeOTAD purchased from Lumtech. The results, presented in Figure 2.5, show strong agreement: both samples display 44 aromatic H residing in the range of 6.40~7.50 ppm, while the 24 H from the methoxy group gave a single sharp peak at 3.76 ppm. The spiro-MeOTAD was dissolved in and precipitated from a dichloromethane/methanol solvent multiple times in order to decolorize the product to pale yellow, which removed the impurities, spiro-MeOTAD radical cation by oxidation.

Table 2.1 C-N bond formation of spiro-MeOTAD by Ullmann or Buchwald-Hartwig reaction.

Entry	Catalyst	Ligand	Catalyst: Ligand (mol ratio)	Base	Yield[a]
1	Cu	18-crown-6	1:2	K_2CO_3	0%
2	Pd $(OAc)_2$	$P(t\text{-}Bu)_2Cl$	1:2	NaOtBu	23%
3	Pd $(OAc)_2$	$P(t\text{-}Bu)_3$	1:2	NaOtBu	26%
4	$PdCl_2$dppf	N.A.	N.A.	NaOtBu	0%
5	Pd_2dba_3	dppf[b]	1:2	Cs_2CO_3	0%
6	Pd_2dba_3	$P(t\text{-}Bu)_3$	1:4	NaOtBu	43%
7	Pd_2dba_3	$P(t\text{-}Bu)_3$	1:6	NaOtBu	85%
8	Pd_2dba_3	$P(t\text{-}Bu)_3$	1:10	NaOtBu	25%

a. Reactions were conducted with 5 mol % catalyst (except Entry 1) in a solvent of toluene at 95-105 °C overnight.

b. 1,1'-Bis(diphenylphosphino)ferrocene, commonly abbreviated dppf.

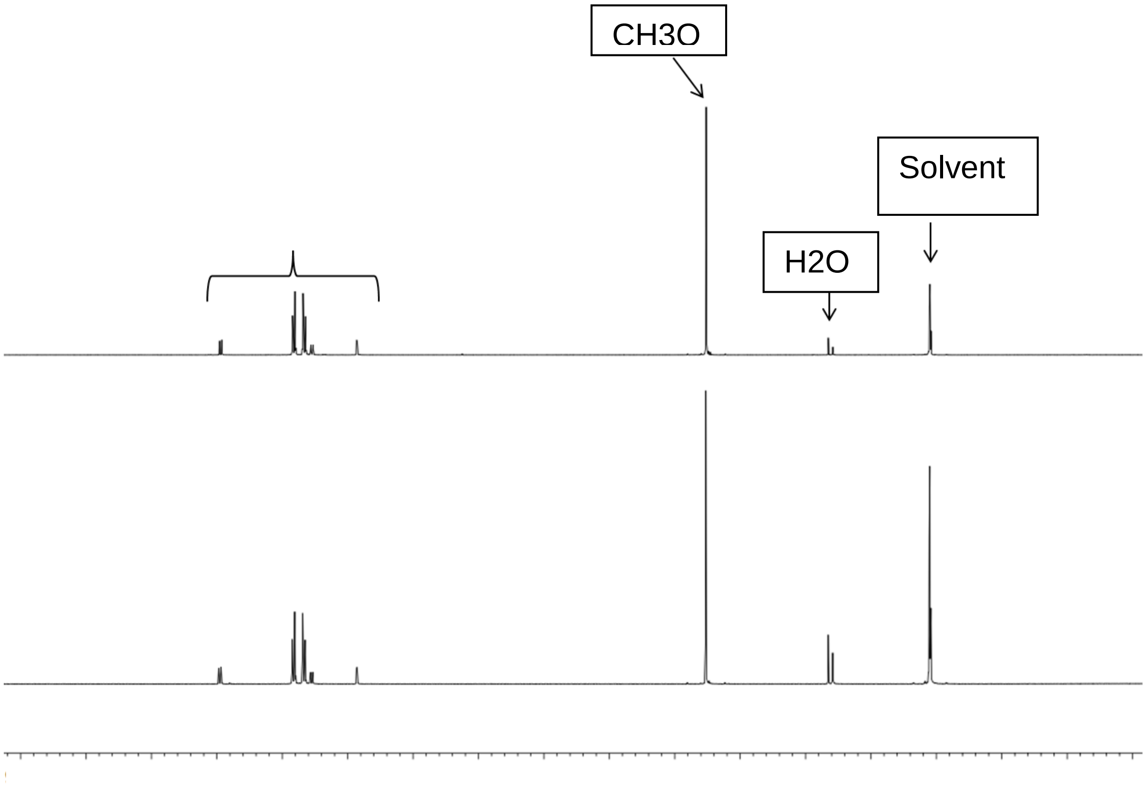

Figure 2.5 Comparison of H1NMR spectrum of Lab-made spiro-MeOTAD (top) and Spiro-MeOTAD purchased from Lumtech. Deuterated solvent used for both samples was $(CD_3)_2CO$.

Thermal properties of spiro-MeOTAD

As mentioned in the beginning of this chapter, spiro compounds have a relatively high T_m and T_g due to their bulky structure and high molecular weights. Spiro-MeOTAD follows this rule, displaying an excellent thermal stability. After the successful synthesis of spiro-MeOTAD, we investigated the thermal properties by thermogravimetric analysis (TGA) and differential scanning calorimetry (DSC).

The TGA curve of spiro-MeOTAD under both air and N_2 atmospheres is displayed in Figure 2.6. When exposed to air under a heating rate of 10 °C/min, the spiro-MeOTAD degradation occurred in two steps in the temperature ranges of 400-515 °C and 515-800 °C, respectively. Conversely, when exposed to an N_2 atmosphere, the degradation occurred in a single step, with a decomposition temperature (T_d) that was 30 °C higher under N_2 than under air. In addition, the final weight retention was 60% at 850 °C in N_2, while it was almost zero under air at the same temperature.

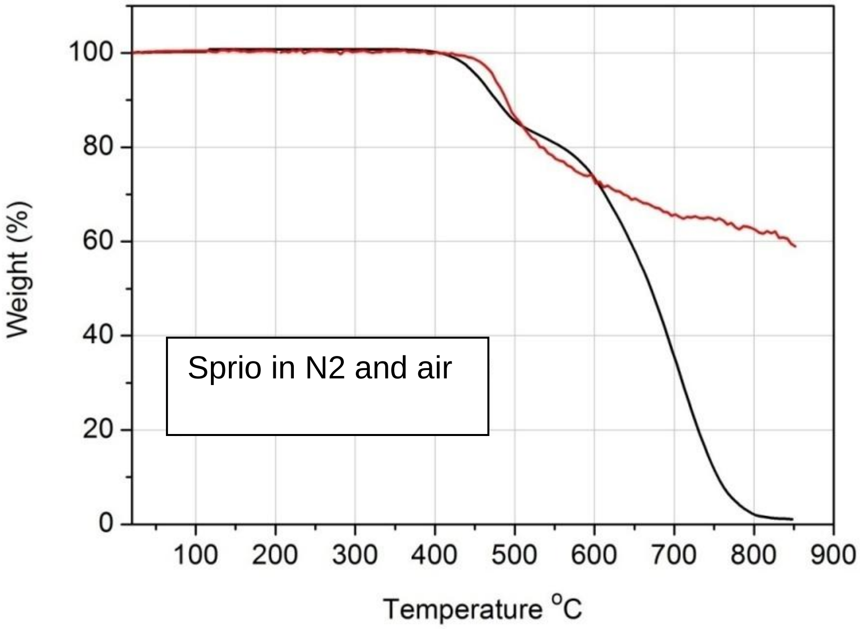

Figure 2.6 Thermogravimetric curve of lab-made spiro-MeOTAD measured at rate of 10 °C/min exposed to N_2 (red line) or air (black line) atmospheres.

The DSC data for the lab-made spiro-MeOTAD was collected under N_2 purging at a rate of 50 mL/min, and is presented in Figure 2.7. The T_g and T_m for the lab-made spiro-MeOTAD were found to be 123 °C and 247 °C, respectively, which is in sharp agreement with DSC results for the commercial spiro-MeOTAD. We found that spiro-MeOTAD formed a very stable amorphous state, in particular the exothermic T_m peak from the 1st heating curve of a crystalline spiro-MeOTAD sample disappeared in the second heating cycle, suggesting that it had remained in the amorphous state after cooling. Indeed, only the T_g bump is visible in the second heating, which further supports spiro-MeOTAD's failure to recrystallize after arriving in the glassy state.

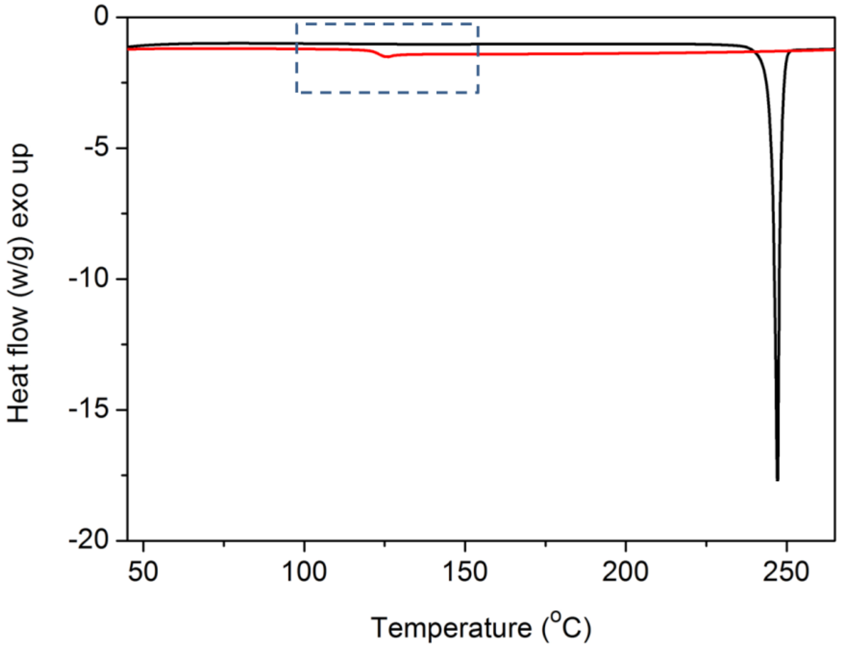

Figure 2.7 Differential scanning calorimetric curves for spiro-MeOTAD (first and second heating curve). The T_g is indicated by a characteristic step and the T_m by an exothermic peak. All measurements were carried out under N_2 purging (50 mL/min) and at a rate of 10 °C/min.

Optical properties of spiro-MeOTAD and its oxidized state

The absorption spectrum of spiro-MeOTAD is displayed in Figure 2.8. The maximum absorbance peak of spiro-MeOTAD lies at 394 nm, which is associated with chlorobenzene. A wide scan of spiro-MeOTAD from 300 nm to 750 nm exhibited a strong absorption only in UV range, with a high molar extinction coefficient of 7×10^{-4} L mol^{-1} cm^{-1}. No peaks were present in the visible region, from 400-700 nm, where the dye molecules used in the DSSC are active. This confirms that, the spiro-MeOTAD will not compete with the dye molecule for photons in the visible light spectrum.

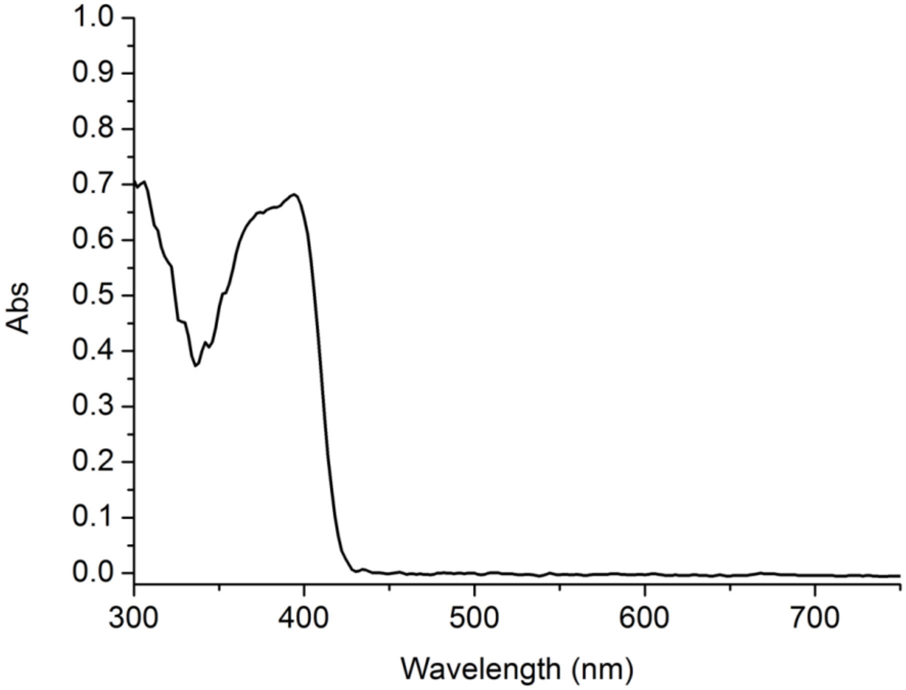

Figure 2.8 Absorption spectrum of 1×10^{-5} M spiro-MeOTAD in chlorobenzene. Inset is a narrow scan from 300 nm to 450 nm.

Films composed of pure spiro-MeOTAD exhibit low hole conductivity and mobility. Doping spiro-MeOTAD with chemical p-dopant can partially oxidize the spiro-MeoTAD, yielding the spiro-MeOTAD radical cation (spiro-MeOTAD^{+}) [oxidized state]. It is well documented that the dark hole-conductivity of spiro-MeOTAD increases by several orders of magnitude with increasing density of the radical cation[10]. Typical p-dopants in ss-DSSC include $NOBF_4$ and tris (p-bromophenyl) ammoniumyl hexachloroantimonate, [N(p-$C_6H_4Br)_3$][$SbCl_6$]. The chemistry guiding the conversion of spiro-MeOTAD to its oxidized state is shown in Figure 2.9.

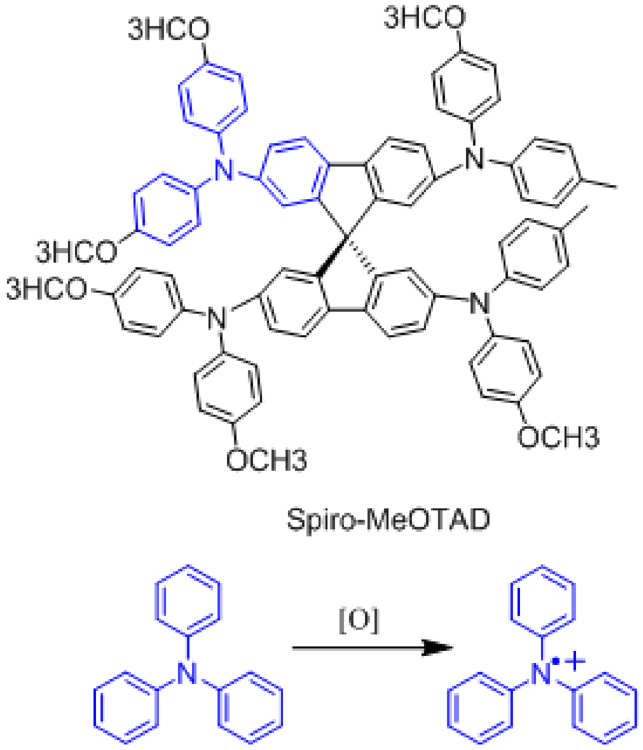

Figure 2.9 spiro-MeOTAD and its conversion to an oxidized state.

We used UV-Vis spectroscopy to confirm the presence of the oxidized form, spiro-MeOTAD$^+$, after the p-dopant was added to the spiro-MeOTAD. A 1:2 mixture of spiro-MeOTAD and [N(p-$C_6H_4Br)_3$][$SbCl_6$] oxidant was dissolved in chlorobenzene. Both spiro-MeOTAD and [N(p-$C_6H_4Br)_3$][$SbCl_6$] absorb only in the near UV and UV region. After mixing these two compounds together, a new peak emerged at 525 nm while the major peak at 390 nm was somewhat attenuated. The new peak obtained after oxidization is consistence with the formation of sprio-MeOTAD$^+$. In chapter 3, we will discuss these optical properties of spiro-MeOTAD in conjunction with an investigation of the light soaking effect in ss-DSSC.

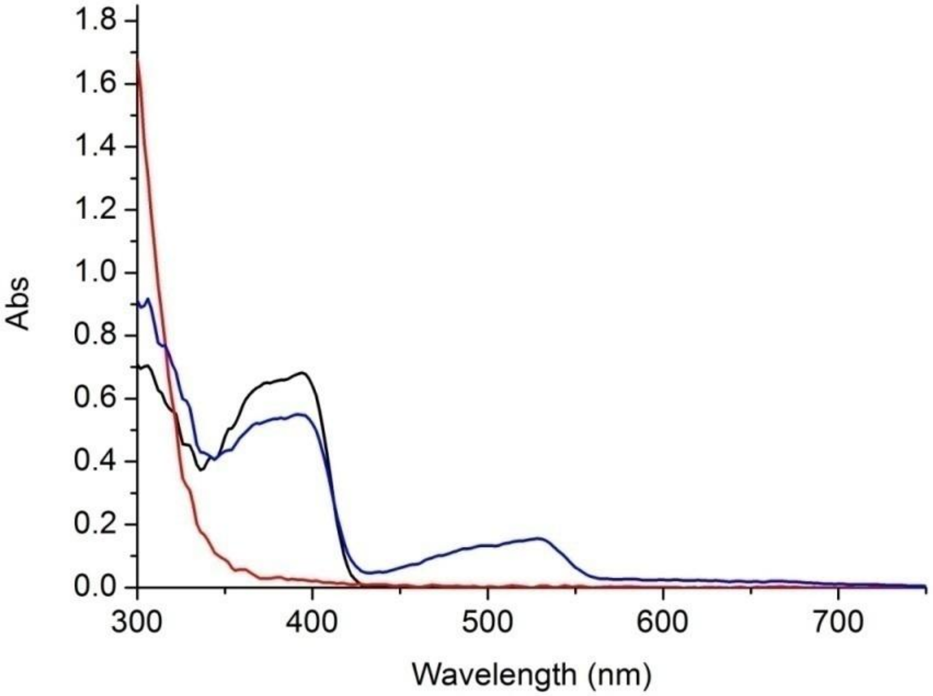

Figure 2.10 UV-Vis spectrum of spiro-MeOTAD (black), the oxidizer (red), and the mixture (blue) containing the oxidized state.

Conclusion

In this chapter, we successfully synthesized spiro-MeOTAD, one of the most commonly used hole transport materials in ss-DSSC. We confirmed the structure and purity by proton NMR and compared with commercial one purchased from Lumtech. We've also performed the TGA and DSC measurement to study the thermal properties of spiro-MeOTAD. The spiro-MeOTAD showed a high T_g of 123 ℃ and T_m of 247 ℃, which preferably formed a very stable amorphous state. This amorphous state structure is suitable to penetrate into TiO_2 pores with few vacancies between TiO_2 particles, boosting dye regeneration efficiency in ss-DSSC. Absorption spectroscopy was also conducted on spiro-MeOTAD, and a strong absorbance around 390 nm was observed. Oxidation of spiro-MeOTAD by p-dopant was captured with an additional broad peak appeared at 525 nm. A small loading of oxidized state of spiro-MeOTAD will increase the solar cell performance and will be detailed discussed in the next chapter

Experimental

2.4.1Materials

All the chemicals purchased from Sigma-Aldrich and TCI America and were used as receive unless mentioned otherwise. The toluene was distilled before use.

2.4.2 Instruments

^{1}H NMR spectra were collected using a Varian UnityPlus-500 spectrometer. Thermogravimetric analyses (TGA) were obtained in air using a Perkin-Elmer TGA 7. The heating rate is 10 °C/min, and samples were held at 120 °C for 30 min before running. Differential scanning calorimetry (DSC) measurements were carried out using a TA DSC Q100 with a heating/cooling rate of 10 °C/min under nitrogen. Absorption spectra were obtained from Varian Carey Model 50 UV-Vis Spectrophotometer.

2.4.3 Synthesis

Bis-(4-methoxyphenyl) amine 3 was synthesized by literature[7]**.** ^{1}H NMR ($CDCl_3$), δ= 3.83 (s, 6H), 5.36 (s, 1H), 6.94(dd, 8H).

2-Iodo-1-phenylbenzene 5 was synthesized by literature[11]. ^{1}H NMR ($CDCl_3$), δ= 7.03 (m, 1H), 7.30-7.47 (m, 7H), 7.96 (m, 1H).

9, 9'-spirobifluorene 7 was synthesized by literature[11]**.** ^{1}H NMR ($CDCl_3$), δ= 6.72 (m, 4H), 7.09 (m, 4H), 7.33 (m, 4H), 7.83 (m, 4H).

2, 2’, 7, 7’-tetrabromo-9, 9’-spirobifluorene 8 was synthesized by literature[8]**.** ^{1}H NMR ($CDCl_3$), δ= 6.81 (d, 4H), 7.51 (dd, 4H), 7.60 (d, 4H).

2, 2’, 7, 7’ -tetrakis (N, N-di-p-methoxyphenylamine) 9, 9’-spirobifluorene (spiro-MeOTAD). A degassed suspension of tetrabromo-spirobifluorene **8** (0.640g, 1mmol), diphenylamine **3** (0.966g, 4.2mmol), tBuONa (1.16g, 12mmol) and Pd_2dba_3 (0.0480g, 0.05 mmol) were prepared in 20mL fresh distilled toluene prior to adding tri-tert-butylphosphine (0.3mL, 0.3 mmol, 1.0M in toluene). The reaction mixture was gradually heated to 105 °C and allowed to stir for 12 hours before cooling, then passing through a flash SiO_2 column with 25% EtOAC/Hexane as eluent before dry to crude brown solid. Further purification by multiple times precipitation from CH_2Cl_2/Methanol gave a pale yellow powder after vacuum dry over night at 65°C Yield: 85%. ^{1}H NMR (D-acetone), δ= 7.49 (d, 4H), 6.89 (m, 32H), 6.80 (dd, 4H), 6.45 (d, 4H), 3.75 (s, 24H).

REFERENCES

REFERENCES

(1) Bach, U.; Lupo, D.; Comte, P.; Moser, J. E.; Weissortel, F.; Salbeck, J.; Spreitzer, H.; Gratzel, M.: Solid-state dye-sensitized mesoporous TiO2 solar cells with high photon-to-electron conversion efficiencies. *Nature* **1998**, *395*, 583-585.

(2) Weissörtel, F.: *PhD. Thesis. University of Regensburg* **1999**.

(3) Schmidt-Mende, L.; Gratzel, M.: TiO2 pore-filling and its effect on the efficiency of solid-state dye-sensitized solar cells. *Thin Solid Films* **2006**, *500*, 296-301.

(4) Ding, I. K.; Tetreault, N.; Brillet, J.; Hardin, B. E.; Smith, E. H.; Rosenthal, S. J.; Sauvage, F.; Gratzel, M.; McGehee, M. D.: Pore-Filling of Spiro-OMeTAD in Solid-State Dye Sensitized Solar Cells: Quantification, Mechanism, and Consequences for Device Performance. *Adv Funct Mater* **2009**, *19*, 2431-2436.

(5) Naito, K.: Quantitative Relations between Glass-Transition Temperatures and Thermodynamic Parameters for Various Materials - Molecular Design for Nonpolymeric Organic-Dye Glasses with Thermal-Stability. *Chem Mater* **1994**, *6*, 2343-2350.

(6) Naito, K.; Miura, A.: Molecular Design for Nonpolymeric Organic-Dye Glasses with Thermal-Stability - Relations between Thermodynamic Parameters and Amorphous Properties. *J Phys Chem-Us* **1993**, *97*, 6240-6248.

(7) Ma, D. W.; Cai, Q.; Zhang, H.: Mild method for Ullmann coupling reaction of amines and aryl halides. *Org Lett* **2003**, *5*, 2453-2455.

(8) Wu, R. L.; Schumm, J. S.; Pearson, D. L.; Tour, J. M.: Convergent synthetic routes to orthogonally fused conjugated oligomers directed toward molecular scale electronic device applications. *J Org Chem* **1996**, *61*, 6906-6921.

(9) Stossel, P. F., DE), Spreitzer, Hubert (Viernheim, DE), Becker, Heinrich (Eppstein-Niederjosbach, DE): Method for the production of arylamines. United States, 2005.

(10) Bach, U.: *PhD. Thesis. EPFL* **2000**.

(11) Convergent Synthetic Routes to Orthogonally Fused Conjugated Poriel, C.; Ferrand, Y.; Juillard, S.; Le Maux, P.; Simonneaux, G.: Synthesis and stereochemical studies of di and tetra 9,9 '-spirobifluorene porphyrins: new building blocks for catalytic material. *Tetrahedron* **2004**, *60*, 145-158.

Chapter 3 The role of Lithium salts in fill factor enhancement of solid-state dye sensitized solar cells

3.1 Introduction:

Solid state dye sensitized solar cells (ss-DSSC) generally suffer from low hole conductivity[1-5]: improving hole conductivity while minimizing parasitic back reactions, such as charge recombination, is a major thrust of current research[6-9]. It has been observed experimentally that the addition of lithium salts can have a dramatic impact on hole conductivity. Contrary to prior thought, we argue that the primary role of Li salt is to stabilize the oxidation state of hole conducting molecules. The initial motivation for adding p-dopants was to modify the band-gap structure in the porous TiO_2 photo-anode and to compensate for space-charge effects[1], increase polarizability of the medium[10], and smooth the potential landscape[10] for efficient charge transport. In this chapter, we present data to support the thesis that lithium salt serves primarily to stabilize the oxidized state of spiro-MeOTAD$^+$ which is produced under illumination in an oxygenated environment. It is well documented that partially oxidized (also called doped) hole conductors exhibit significantly better conductivity. We illuminate the hole conductor under open-circuit conditions, and subsequently characterize the state of the spiro-MeOTAD by measuring ex-situ absorbance and by obtaining in-situ J-V curves, both as a function of time of illumination, under various filters, and for a combination of Li salts with different anions. We also examine electron life-time and electrochemical impedance spectroscopy to quantify rates of charge recombination.

In this chapter we first provide an overview of doping in organic or polymeric materials. Subsequently, we discuss the prior literature on p-dopants and additives incorporated into ss-DSSCs. Finally we present our data that suggests the primary role of Lithium salts is to stabilize the oxidized state of the hole conducting polymer.

Poor charge conduction in ss-DSSC is widely attributed to the slowness of the hole hopping mechanism which provides the dominant mechanism of charger transportationin solid state conductors. Chemical doping increases conductivity of the organic or polymeric conductor, either by partially oxidizing the electron acceptors (p-doping) or by reduction of the electron donor (n-doping). This process generates positively or negatively charged defects, enhancing the density of charge carriers in the conductor. Generally, doping can be accomplished through chemical and electrochemical processes. Chemical doping can be considered as a redox reaction in which the neutral conductor is oxidized or reduced to cations or anions (Chemical Equation 1&2). Such reactions are particularly facile in conductive polymers, like polypyrrole, polyacetylene, polyaniline and polyacene.

Where Ox_1 and Red_2 denote the oxidizing and reducing agents, respectively, while red_1 and ox_2 are their conjugates formed as a result of the charge transfer reaction.

Electrochemical doping corresponds to the removal or addition of electrons at the interface of an electrode. In the case of polyacene, shown below, positively charged molecules are p-doped, and negatively charged polyacenes are n-doped (Chemical Equation 3&4). Dopant ions form during the electron transfer reaction or as the original component of the system.

Other doping methods include photo-doping, charge-injection doping, and Non-redox doping. The successful doping of the conductor will enhance conductivity, typically by several orders of magnitude. The mechanism of this enhancement is explained in Figure 3.1. In organic conductors, there is a finite energy gap that separates the HOMO (highest occupied molecular orbital, valence band) and LUMO (lowest unoccupied molecular orbital, conducting band).This energy gap (E_g), corresponds to the energy that must be applied to the system to induce charge mobility. The P-doping process removes one electron from the HOMO, and thus the HOMO level increases while E_g decreases. For the n-doping process, one electron is added to LUMO lowering its energy level and decreasing E_g. In this manner, both p and n-doping decrease E_g and hence increase the conductivity.

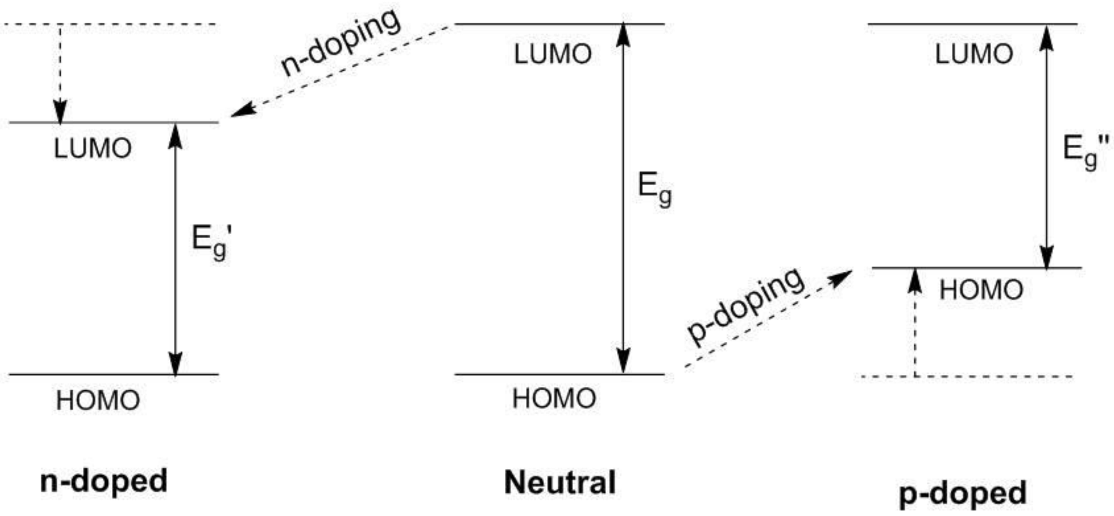

Figure 3.1 Molecular orbital energy diagram of organic conductor.

Doping is frequently applied quite to ss-DSSC, in order to increase the conductivity of the organic conductor. One of the most commonly used p-dopants in ss-DSSC is the oxidant Antimony complex[1,11]. In the presence of LiTFSI (Li $(CF_3SO_2)_2N$), the conductivity of spiro-MeOTAD has been observed to increase by two orders of magnitude[4] (see Figure 1) to the range of 10^{-5} S/cm. Initially, this enhancement was attributed to the combined effects of p-doping via antimony complex in conjunction with space-charge screening induced by lithium salts[1]. The addition of lithium salts was thought to increase polarizability of the medium[10] and smooth the potential energy landscape[10], thereby increasing the efficiency of charge transportation. Co-dopants with LiTFSI like I_2[12], $NOBF_4$[13,14] and cobalt (III) complex[15] were also observed to increase conductivity and improve the cell performance. However, recent papers indicated that enhanced conductivity could be obtained without the Antimony complex[6,16], while in the presence of antimony complex but absence of LiTFSI the conductivity of the spiro-MeOTAD remained approximately the same as for neat spiro-MeOTAD[10]. Indeed there was no direct evidence supporting the oxidization of spiro-MeOTAD by addition of LiTFSI (see Figure 3.2).

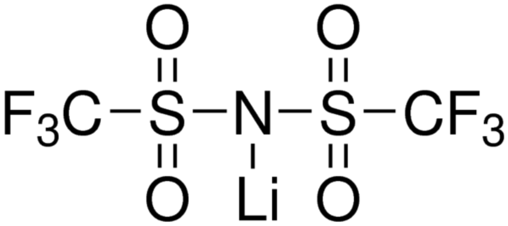

Figure 3.2 Left: Absorption spectra of a 7 mM solution of spiro-MeOTAD in chlorobenzene. Right: Current-voltage characteristics for in-plane devices containing pure spiro-MeOTAD and its doped state.

Very recently, Bach's group observed spiro-MeOTAD$^+$ formation at the TiO_2 interface during cell illumination and suggested a superoxide was involved in the oxidation of the spiro-MeOTAD[17], and furthermore that LiTFSI was required in the oxidation mechanism. Later, Snaith's group studied a system of SnO_2-based DSSCs. They observed a steady increase of short-circuit photocurrent under constant illumination, and argued that the creep in short-circuit current was probably caused by a conduction band shift of SnO_2 after light soaking[18]. In this chapter, we argue that these effects are due to the photo-oxidation of spiro-MeOTAD was in an oxygenated environment. We observe that the fill factor of DSSCs cell improves steady for 20 minutes under light exposure, at which point the cell reaches maximum efficiency. We argue that LiTFSI triggers this oxidation regardless of the composition of the semiconductor (either TiO_2 or SnO_2). We support this argument by analyzing absorbance and J-V curve measurements under various conditions. For photons in the near UV region, LiTFSI can catalyze photo-oxidation of spiro-MeOTAD$^+$ in an oxygenated environment. For photons in the visible region, a chromophore is also required to catalyze the oxidation. Unlike the steady increase of photocurrent measured in an organic dye based ss-DSSC[17], the current from a ruthenium dye based ss-DSSC marginally decreased until it stabilized. We argue that this is due to an enhancement of charge recombination. Additionally, we investigated the influence of the counter-ion in lithium salts on ss-DSSC performance, finding that LiTFSI is the most efficient at stabilizing spiro-MeOTAD$^+$, yielding the highest cell efficiency.

Result and discussion:

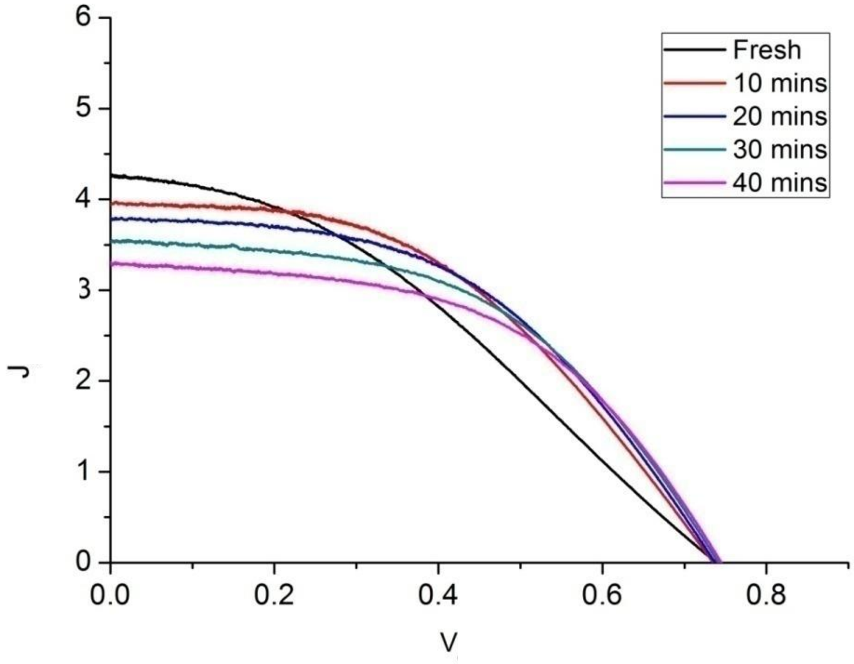

Figure 3.3 J-V curves of ss-DSSC measured after periods of 10, 20, 30, and 40 minutes of steady light exposure.

The fabricated ss-DSSC was stored under an N_2 atmosphere before the initial operation. The cell was then illuminated under an open-circuit for a pre determined period of time, after which the current-voltage characteristic (J-V curve) was measured. As shown in Figure 3.3, the fill factor (FF) and short-circuit current density (J_{SC}) varied considerably as a function of the open-circuit illumination time. The black curve in Figure 1 shows the J-V curve with zero open-circuit illumination time: it shows the highest J_{SC} of 4.3 mA/cm^2 and the lowest FF of 0.36 (see Table 3.1). Increasing the open-circuit illumination from zero to 40 minutes, the FF of ss-DSSC increased while J_{SC} slightly decreased. (see Figure 3.3 and Table 3.1).

Table 3.1 Summary of cell performance for different periods of open-circuit illumination

Time	J_{sc}(mA/cm^2)	V_{oc}(V)	FF	η(%)
Fresh	4.3	0.74	0.36	1.1
10 mins	3.9	0.74	0.46	1.3
20mins	3.8	0.74	0.49	1.4
30 mins	3.6	0.74	0.50	1.3
40 mins	3.3	0.74	0.51	1.2

We extended this experiment up to two hours of open-circuit illumination give a clearer trend. As displayed in Figure 4a, the J_{SC} attenuated gradually in the first 40 minutes until achieving a steady value of 3.0 mA/cm^2. After a period of 2 hours, the short-circuit current had decreased by roughly 30% compared to the non-illuminated state. However, the cell's FF increased by 40% over the first 20 minutes of illumination, stabilizing at a value of 0.5 (see Figure 3.4b). Meanwhile, the open-circuit voltage, V_{OC}, remained constant around 0.74V. Overall, the cell's power conversion efficiency achieved a maximum value after 20 minutes of open-circuit illumination and then decreased slightly thereafter reaching a steady-state (see Figure 3.4a).From Table 1, we see that after 20 mins the cell had a J_{SC} of 3.8 mA/cm^2, V_{OC} of 0.74 V, and FF of 0.49. Compared to the original cell without open-circuit illumination, the FF had increased by 36% while the short-circuit current density decreased 12%. Eventually, the overall efficiency improved by over 25%.

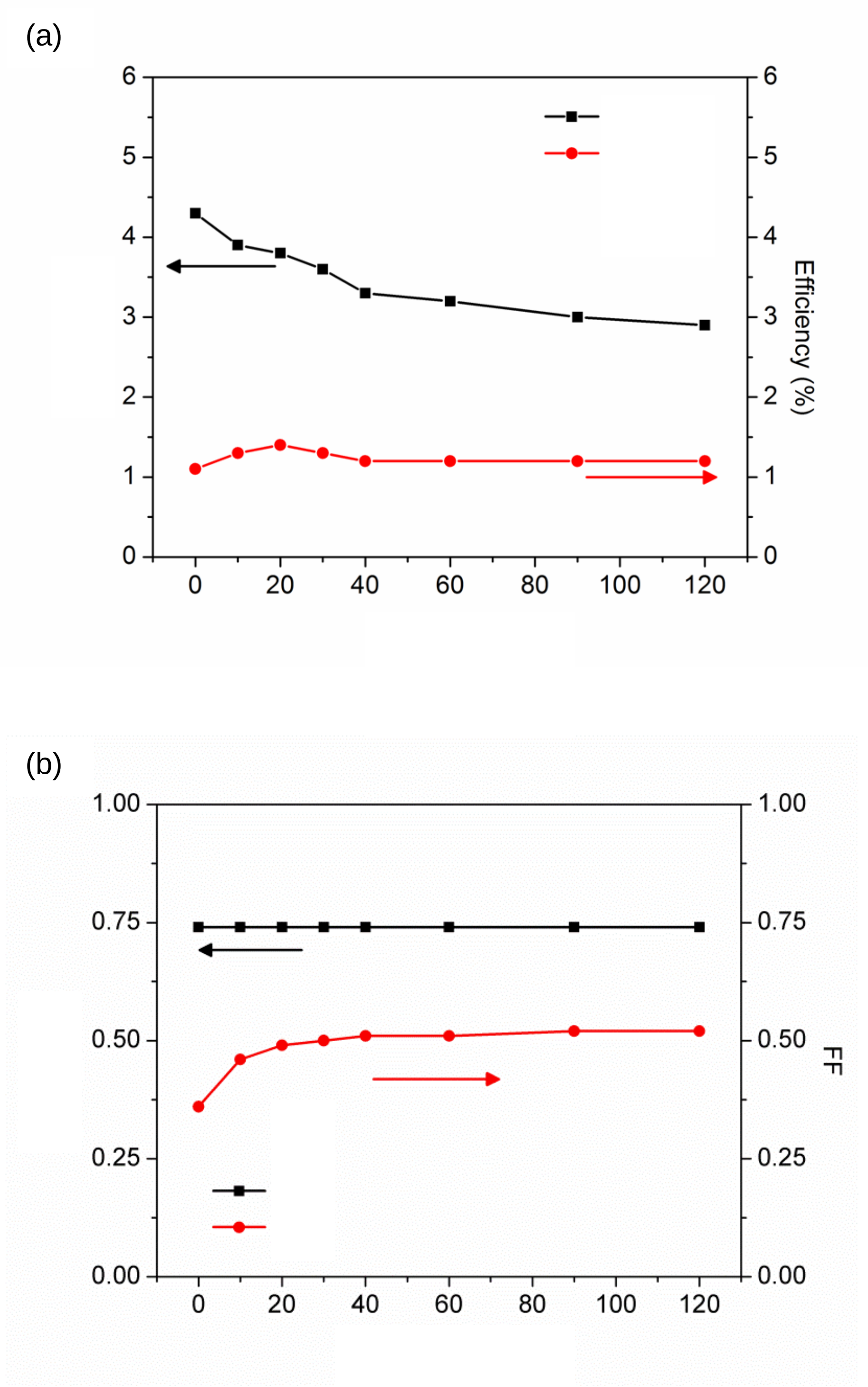

Figure 3.4 Cell performances as a function of open-circuit illumination time. (a) J_{SC} (mA/cm^2) and Eff (%) Vs time (mins); (b) V_{OC}(V) and FF Vs time (mins).

Enhancement of Fill Factor (FF) after pre-illumination:

Previous reports[19,20] have established that UV exposure of liquid-based DSSC cells can lead to a remarkable increase in photocurrent, a higher injection efficiency and faster charge transport[19]. This phenomenon had not been investigated in ss-DSSC. Long pass filters have a sharp transition in transmittance at a cut-point in frequency. To study the UV effect in ss-DSSCs, we repeated the open-circuit illumination trials on cells that were overlaid with either a 385nm or a 435nm filter during the open-circuit illumination. The filters eliminated the UV component of the light source. As shown in Figure 3.5, the cells exhibited the same increase in FF after 20 minutes as those that had been exposed to the full spectrum of light. Moreover, we repeated the open-circuit illumination experiment using a 20-minute exposure to a monochromatic green light (500nm). As shown in Figure 3.6, these cells also showed the same tendency, with increased FF and a minor loss of J_{SC}. This demonstrates that the light-soaking effects can be achieved with light from the visible spectrum.

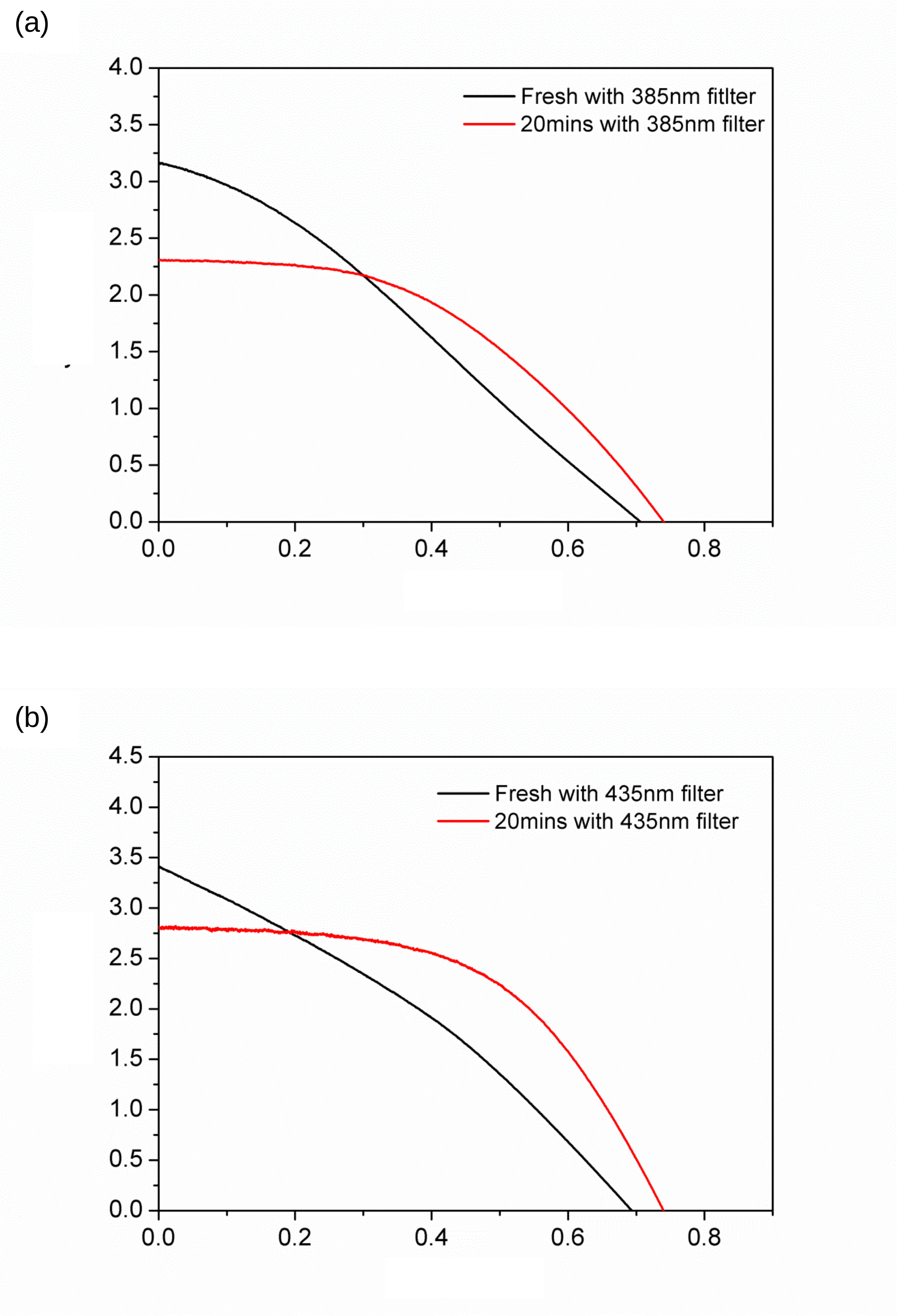

Figure 3.5. J-V curve of ss-DSSC with zero and 20 minutes open-circuit illumination overlaid with (a) 385 nm long pass filter; and (b) 435 nm long pass filter.

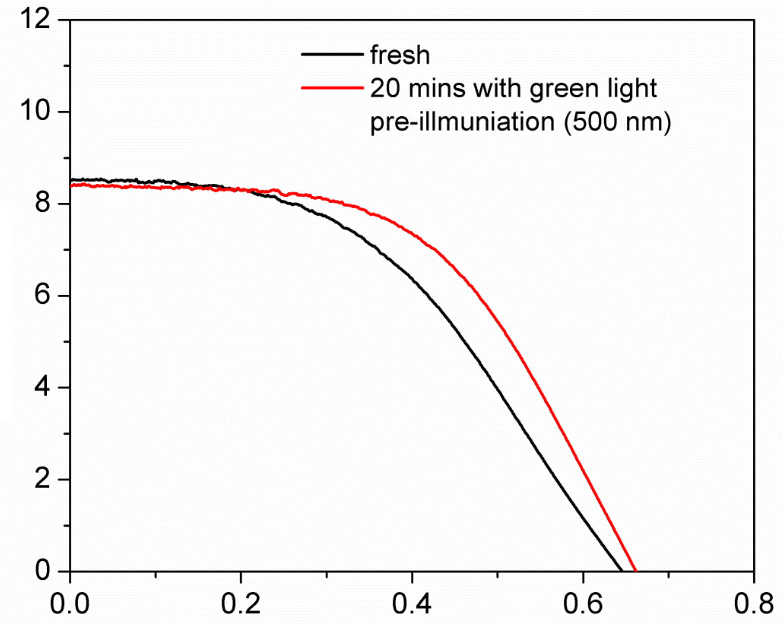

Figure 3.6 J-V curve of ass-DSSC after zero and 20-minute open-circuit illumination under monochromatic light (500nm wavelength).

We propose that during open-circuit illumination the excited dye injects electrons into the TiO_2, leaving behind oxidized dye is regenerated by the spiro-MeOTAD, forming its oxidized state spiro-MeOTAD$^+$. But electrons captured by TiO_2 couldn't be transported to out-circuit under open-circuit condition. The absorbed photon energy was subsequently either transferred to heat or recombine with spiro-MeOTAD$^+$. Moreover, given the hole transport properties of spiro-MeOTAD, it is natural to assume that the density of spiro-MeOTAD$^+$ would equilibrate to a spatially uniform distribution. Grätzel's group[10] reported that blending 12% Li salts with the hole conducting polymer lead to a significant increase in hole mobility and hence to better power conversion efficiency, however, they did not establish the formation of spiro-MeOTAD$^+$. Since the oxidized state of spiro-MeOTAD has different optical absorption properties, it is natural to use this physical distinction to track the evolution of the oxidized state.

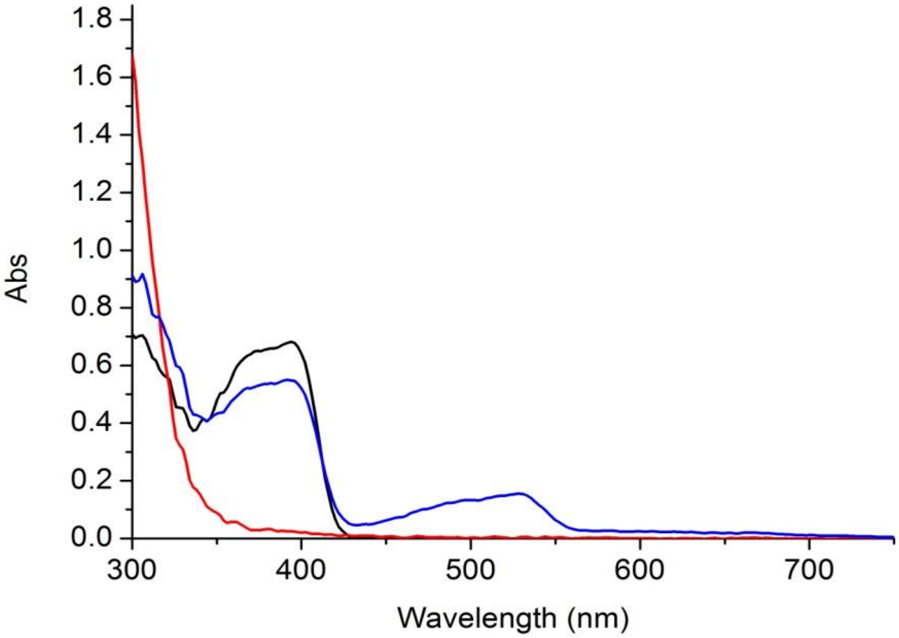

Figure 3.7 Absorption spectra of chlorobenzene solution of spiro-MeOTAD, $N(PhBr)_3SbCl_6$, and spiro-MeOTAD with 2 eq. of $N(PhBr)_3SbCl_6$. The concentration of spiro-MeOTAD in chlorobenzene is 10^{-5}mol/L.

We believe the enhanced FF in ss-DSSCs after open-circuit illumination results from p-doping of spiro-MeOTAD into its oxidized state. Furthermore we suspect that the role of lithium salt as an additive is to stabilize the oxidized state of the spiro-MeOTAD. To demonstrate this hypothesis, we used UV-Vis spectroscopy to detect the concentration of the oxidized state of spiro-MeOTAD under ex-situ conditions, particularly in the absence of TiO_2 and dye. To establish the signature absorption spectra peak of oxidized spiro-MeOTAD (spiro-MeOTAD$^+$), we used tris (p-bromophenyl) ammoniumyl hexachloroantimonate ($N(PhBr)_3SbCl_6$) (Sb complex salt) as an oxidant to create spiro-MeOTAD$^+$ through electron transfer oxidation. Compared with the neat spiro-MeOTAD and Sb complex salt, as shown in Figure 7, a 525 nm absorbance peak appeared which we take as the signature for the presence of the oxidized state of spiro-MeOTAD. Subsequently, we replaced the Sb complex salt with the commonly used lithium salts, such as LiTFSI, in the spiro-MeOTAD solution. The concentration of spiro-MeOTAD used for spin-coating in ss-DSSC is ca. 0.1M and the typical ratio of LiTFSI and spiro-MeOTAD is 1:6.2 (14% Li content). Because of the extremely high extinction coefficient of spiro-MeOTAD, we employed a diluted spiro-MeOTAD solution (10^{-5}mol/L), with the same 14% LiTFSI content, in order to clearly and precisely track the spiro-MeOTAD$^+$ peak.

We measured the absorption spectrum of the solution as a function of the length of illumination. As shown in Figure 3.8, the initial absorption spectrum of the spiro-MeOTAD and LiTFSI mixture does not manifest the spiro-MeOTAD$^+$ signature peak at 525 nm. However, after a 20 minute illumination the spiro-MeOTAD$^+$ signature peak is clearly present, while the absorption peak at 392 nm, corresponding to spiro-MeOTAD, had weakened. This strongly suggests that LiTFSI is not an oxidant, and rather photo-oxidation of the spiro-MeOTAD occurred through ambient oxygen. Moreover, the strength of the oxidized peak was stable, even after continuous illumination up to one hour.

In a subsequent experiment we changed the concentration of lithium salts in the spiro-MeOTAD solution, and measured the absorbance after a 20-minute illumination. Figure 3.9 shows that the intensity of the spiro-MeOTAD$^+$ peak increases with increasing LiTFSI concentration under fixed illumination conditions. We infer from this that the lithium salt acts as a catalyst or reactant in the formation of spiro-MeOTAD$^+$. Equally, the LiTFSI may serve to stabilize the spiro-MeOTAD$^+$. We repeated these experiments with a solid thin film of spiro-MeOTAD and LiTFSI on FTO glass, without the chlorobenzene solution. As shown in Figure 3.10, we observe a small spiro-MeOTAD$^+$ absorbance peak after a 20-minute illumination.

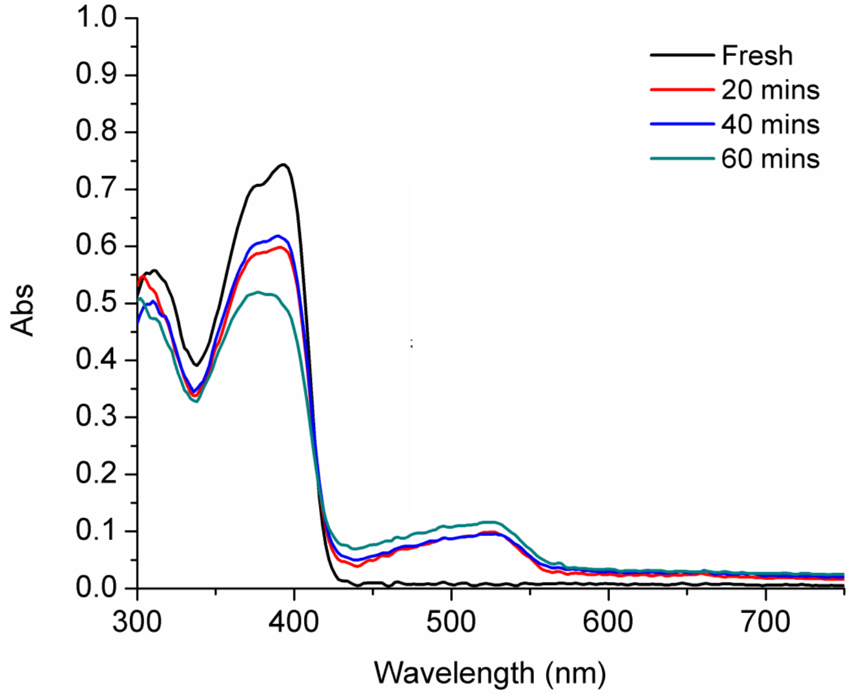

Figure 3.8. Dependenceof absorption spectra of chlorobenzene solution of spiro-MeOTAD with 14% LiTFSI on the length of illumination.

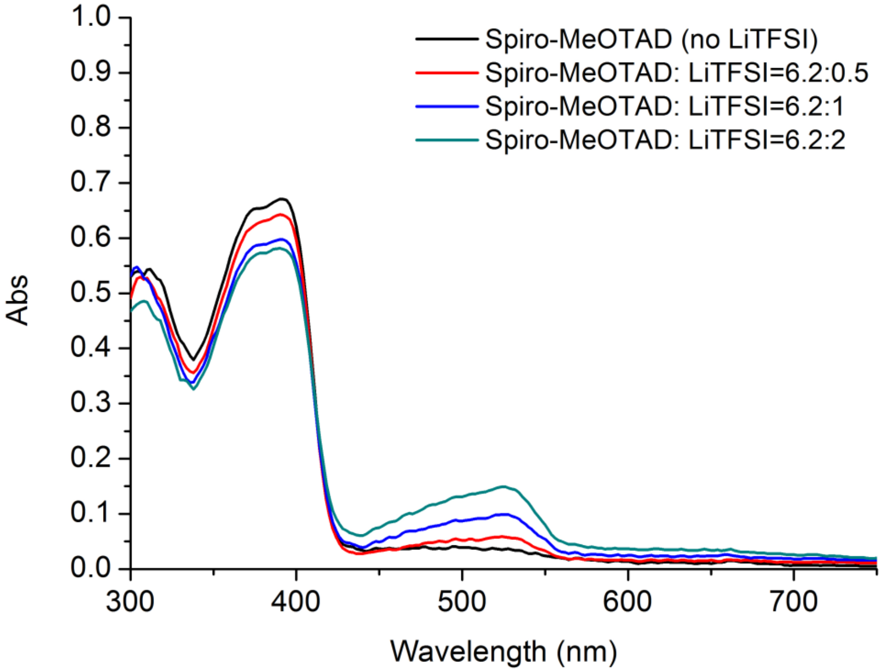

Figure 3.9 Dependence of absorption spectrum of LiTFSI, chlorobenzene solution of spiro-MeOTAD upon concentration of LiTFSI, after 20-minute illumination.

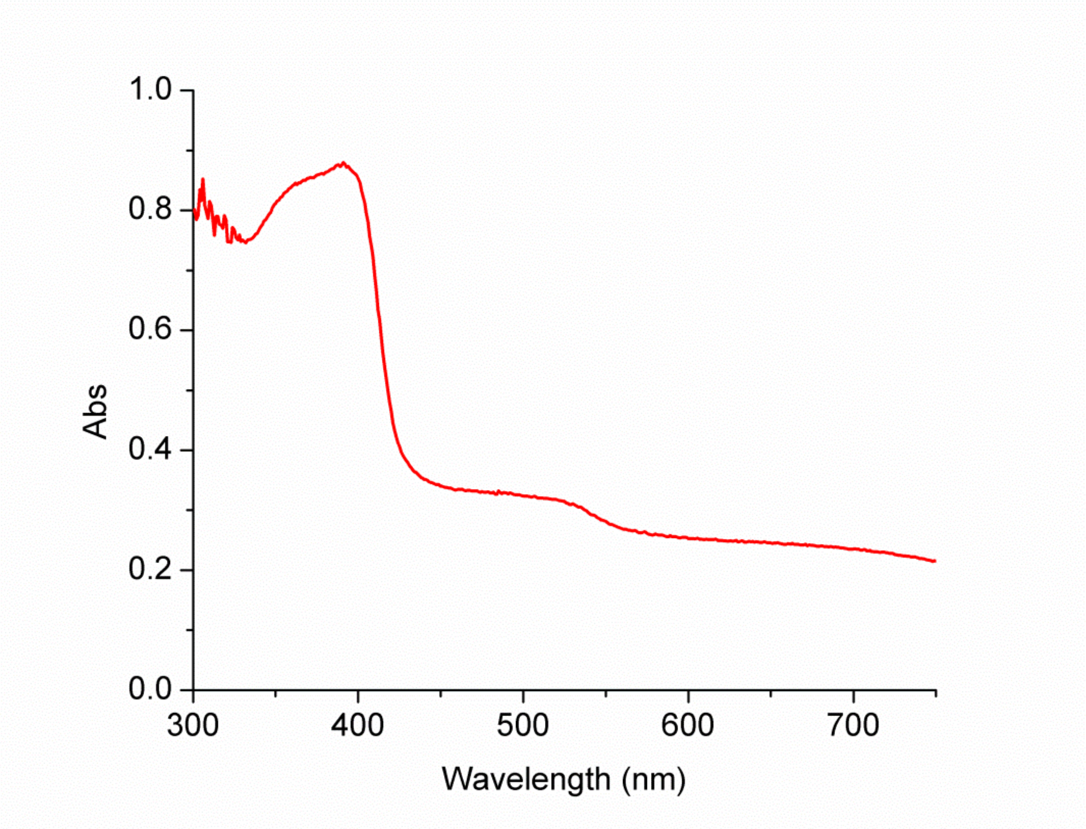

Figure 3.10. Absorption spectrum of spiro-MeOTAD film with LiTFSI on FTO glass after 20-minute illumination.

The in-situ results, reported in Figure 3.5, show a FF enhancement associated to spiro-MeOTAD^{+} formation for illumination under a wide range of light frequencies, including illumination under visible light. We repeated these experiments in our ex-situ framework. Using the same long pass filters (385 nm and 435 nm) overlaid on the spiro-MeOTAD/LiTFSI solution, the mixture was illuminated for 20 minutes, and the absorption was subsequently measured. In Figure 11, we saw that under the 385 nm long-pass filter, the spiro-MeOTAD^{+} signature peak was formed, however under the 435 nm long-pass filter the peak does not form. Since spiro-MeOTAD primarily absorbed around 392 nm, we deduced that the lower energy photons beyond 435 nm were unable to excite the spiro-MeOTAD and could not produce the oxidized state.

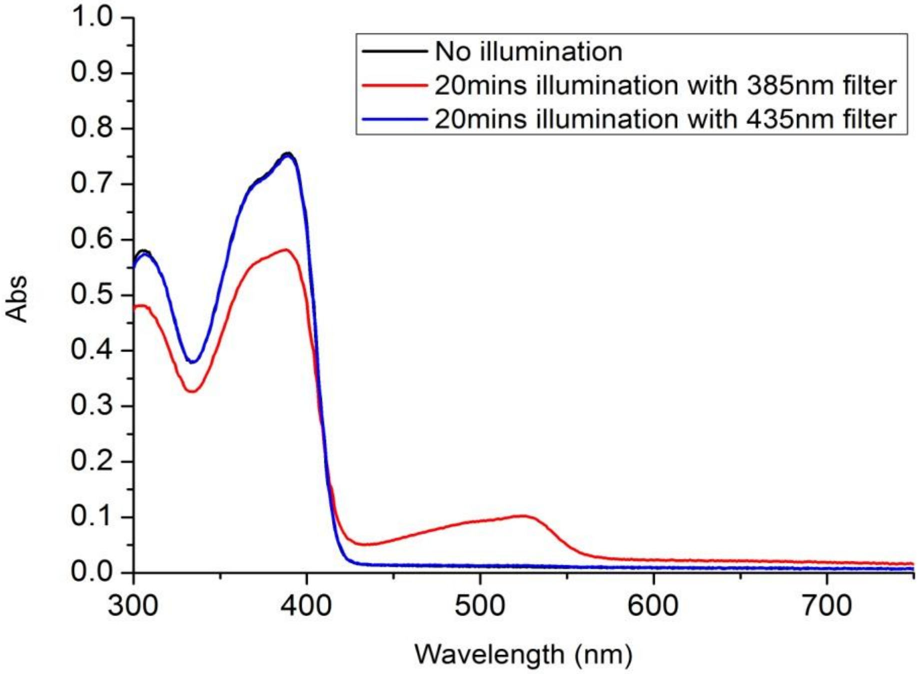

Figure 3.11 Absorption spectra of chlorobenzene solution of spiro-MeOTAD with LiTFSI without illumination and after 20-minute illumination with long pass filters of 385 nm and 435 nm.

The ex-situ results presented above contrasts with the in-situ J-V characteristics presented in Figure 3.5, which demonstrated an improvement in FF even under illumination beyond 435 nm. The TiO_2 semiconductor absorbs primarily in the range from 280 nm to 380 nm, with a peak at 320 nm[21]. Moreover it has been well demonstrated that photo-degradation of the organic compounds occurred only when TiO_2 is illuminated by light with $\lambda<388$nm[22]. This diminishes the probability that the TiO_2 plays a direct role oxidation, and increases the likelihood the light absorber, such as the N3 dye, is an intermediary in the oxidation process. To further investigate this phenomenon we extended the ex-situ experiment, adding N3 dye to the spiro-MeOTAD solution containing LiTFSi, which was illuminated for 20 minutes under a 435 nm long-pass filter, and subsequently measured its absorbance. The result, presented in Figure 3.12, shows the signature 525 nm peak for spiro-MeOTAD$^+$. We used a 6.2:6.2:1 ratio of spiro-MeOTAD: N3 Dye: LiTFSI since the extinction coefficient of spiro-MeOTAD is much larger than N3 dye. The absorbance change contributed by the N3 dye is negligible, and we deduce that the 525 nm peak is attributable to the oxidation of spiro-MeOTAD. In summary: when illuminated in the 385-435 nm range, spiro-MeOTAD can be oxidized by in the presence of LiTFSI. When illuminated beyond 435 nm, the N3 dye was required to obtain spiro-MeOTAD$^+$. Very recently, Snaith's group observed lithium oxide complex formed in a similar system after illumination[23]. This inferred a non-reversible process. However, when we stored the solar cell in glove box and retested it after 24 hours, we observed that FF in J-V plot reversed back to original after 24 hours. We assumed lithium might prefer to presence as a reversible and active ion form, like anchoring on the TiO_2 surface while illuminating. These results suggest the photo-oxidation mechanism proposed in

Scheme 3.1. To examine our hypothesis that the spiro-MeOTAD$^+$ is stabilized by TFSI anion, we examine the ex-situ absorption spectra in a variety of Lithium salts.

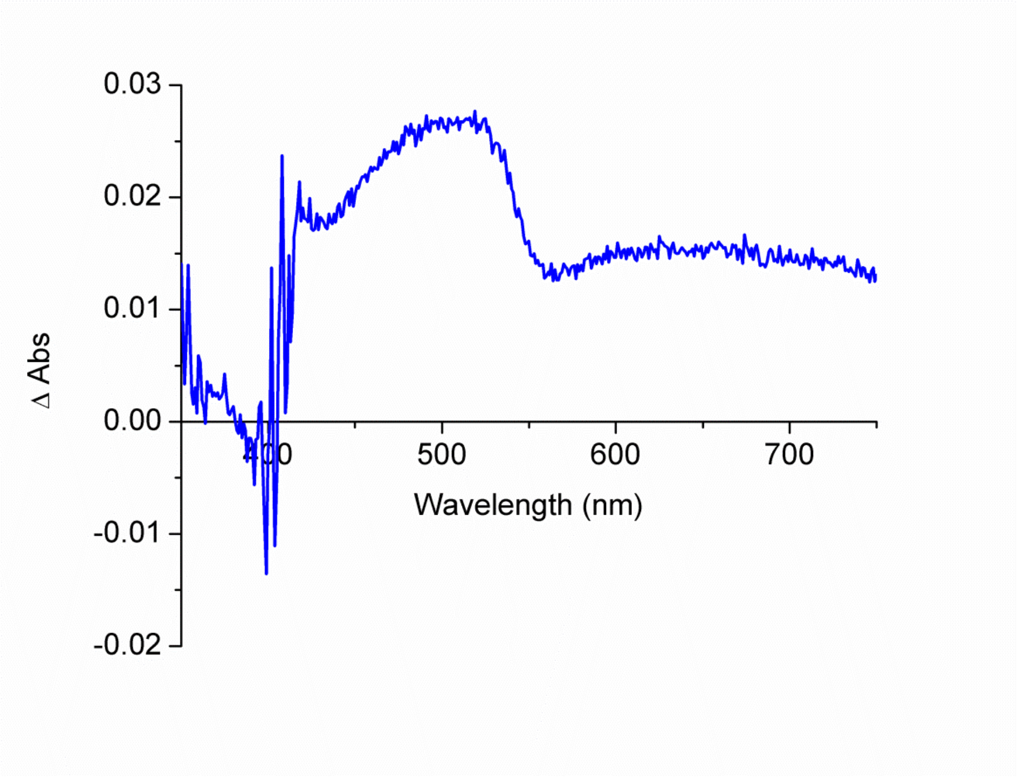

Figure 3.12 Change in absorption spectrum before and after a 20-minute illumination of spiro-MeOTAD with both LiTFSI and N3 dye in chlorobenzene solution under a 435 nm long-pass filter.

$$2\ \text{spiro} + 1/2\ O_2 \xrightarrow[385\text{-}435\text{nm}]{Li^+} 2\ \text{spiro}^+ + O^{2-}$$

$$\text{spiro} + \text{Dye} + 1/2\ O_2 \xrightarrow[>435\text{nm}]{Li^+} \text{Dye}^+ + \text{spiro}^+ + O^{2-}$$

Scheme 3.1 Proposed mechanism of LiTFSI-induced photo-oxidation of spiro-MeOTAD

The mechanism for the reduction of short-circuit current density (J_{SC}).

Table 1 shows that the ss-DSSC performance improvement was mainly achieved through improvement of conductivity, as measured by the FF. However the short-circuit current, J_{SC}, decreased marginally which had a small negative impact on overall cell efficiency. We investigate the role of sprio-MeOTAD$^+$ on charge recombination by investigating the impact of open-circuit illumination on Open-circuit voltage decay (OCVD). A previous study[1] reported a perfect ohmic contact between spiro-MeOTAD and FTO glass. The role of theTiO_2compact layer covering the FTO is to minimize charge recombination at the FTO/spiro-MeOTAD interface. However, as shown in Figure 3.13, cracks can be seen in the compact layer, allowing residual contact between FTO and spiro-MeOTAD. Since photo-oxidization of the spiro-MeOTAD induces fast charge transport, we deduce that the rate of charge recombination between FTO and spiro-MeOTAD$^+$ is greater than that between FTO and spiro-MeOTAD. Charge recombination can also occur between the electrons in the TiO_2 conduction band and either spiro-MeOTAD or its oxidized state.

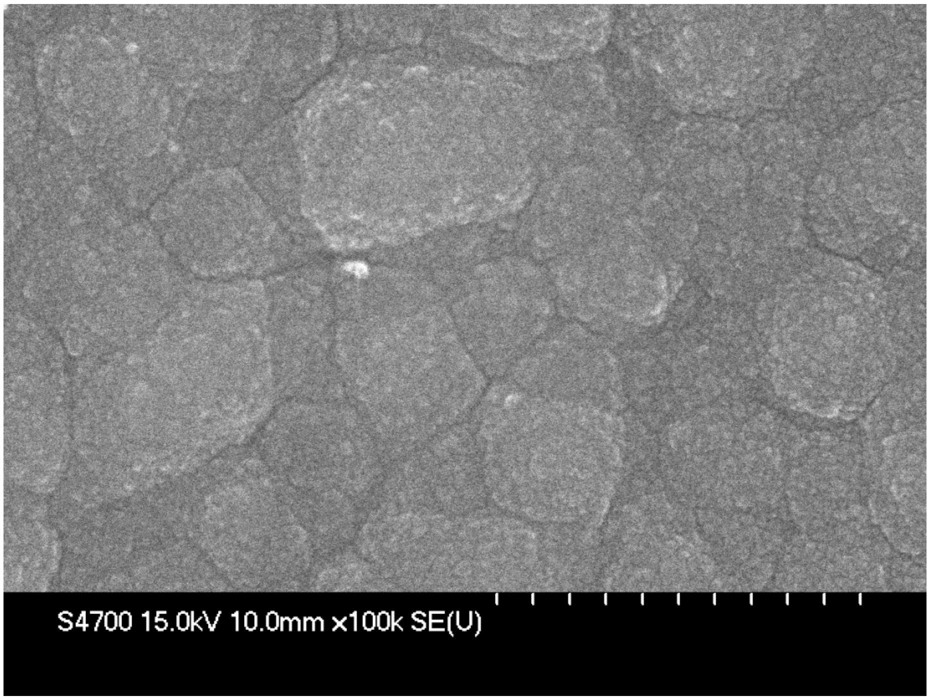

Figure 3.13 Top view of TiO_2 compact layer covering the FTO glass.

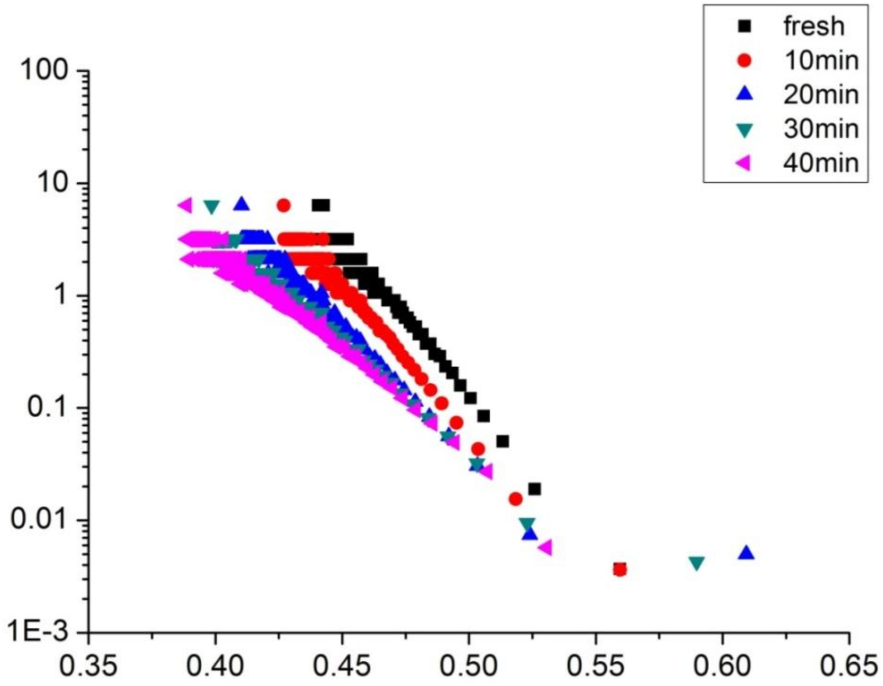

Figure 3.14 Electron lifetime as a function of V_{OC} for a ss-DSSC subject to illumination times of zero, 10, 20, 30, and 40 minutes.

Open-circuit voltage decay (OCVD) is an effective measurement to extract information about rates of charge recombination and electron lifetime in DSSC[24]. The cell is illuminated at open-circuit until a stable voltage is obtained, then the illumination is interrupted, and a potentiostat is used to monitor the temporal decay of the V_{OC}. As there is no external circuit the decay of the V_{OC} reflects the decrease in electron density in TiO_2, which is mainly due to charge recombination. The electron lifetime (τ), defined as the reciprocal of the derivative of the decay curve normalized by the voltage, is a common diagnostic. In general, longer electron lifetime correspond to less charge recombination in DSSC[24]. In Figure 3.14, the τ versus V_{OC} is plotted for a single ss-DSSC with after a range of illumination times. Its dominant feature is the reduction of electron life-time as a function of cell illumination time. This is a strong indication that the increased density of the oxidized state, spiro-MeOTAD is also associated with enhanced rates of charge recombination.

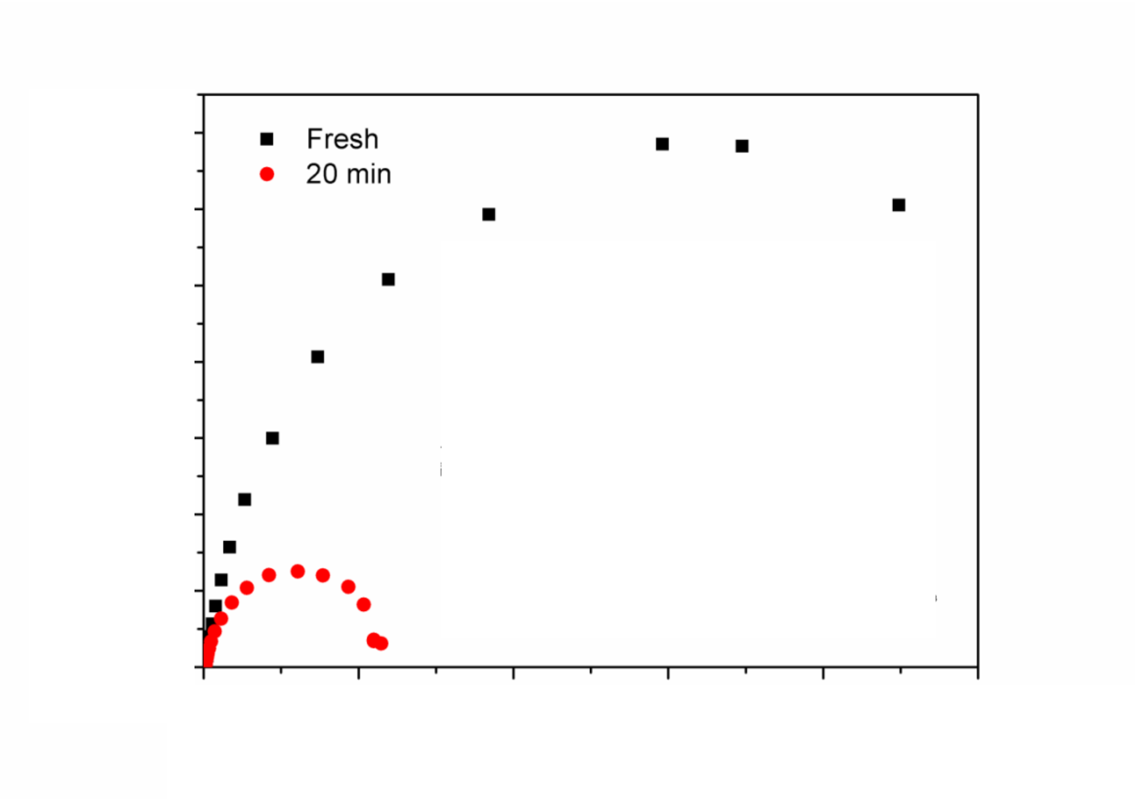

Figure 3.15 EIS spectra of ss-DSSC after zero and 20 minutes of open-circuit illumination. (Inset: high frequency phase of Nyquist plot)

In addition to OCVD measurement, electrochemical impedance spectroscopy (EIS) measurements are frequently used to study charge recombination. In a typical Nyquist plot of ass-DSSC, the high-frequency portion of the curve is associated to electron diffusion in the TiO_2 and the charge-exchange process at the spiro-MeOTAD/Au interface; the low-frequency portion is associated with charge recombination[8]. Figure 3.15 shows the Nyquist plot of ass-DSSC after zero and 20 minutes of open-circuit illumination. The cell was measured at 0.7 V under dark conditions. The charge-transport resistances derived from the high-frequency portion (inset picture in Figure 3.15) are similar before and after short-circuit illumination. However, the low frequency portion of the diagram shows that the cell exposed to a 20-minute open-circuit illumination had a much higher rate of charge recombination as compared to the un-illuminated cell. This result is in agreed with the conclusions obtained from the OCVD measurement.

The elimination of charge recombination after illumination is the subject of on-going research. One potential mechanism to avoid charge recombination in ss-DSSC, is to replace the N3 dye with Z907 dye. The latter dye contains longer hydrophobic chains which serve as spacers between the TiO_2 and spiro-MeOTAD[11]. Another approach is to use zwitterionic co-adsorbents, which shield the TiO_2 surface against charge recombination[8].

The mechanism for the Lithium salt effect:

Lithium salts are common additives to ss-DSSCs due to their superior solubility in organic solvent as compared to sodium and potassium salts. In our previous studies, LiTFSI has been demonstrated to trigger photo-oxidation of spiro-MeOTAD and improved the ss-DSSC performance. The Li cation contributed to the enhancement of FF and was involved in the proposed mechanism presented in Scheme 3.1. To further investigate the mechanism behind the FF improvement, and to select the optimal counter-anion for lithium salts in ss-DSSC applications, we investigate the ex-situ absorption profiles of spiro-MeOTAD in solution with a series of lithium salts, including: lithium tetrafluoroborate ($LiBF_4$), lithium perchlorate ($LiClO_4$), lithium triflate ($LiCF_3SO_3$), lithium chloride (LiCl), and LiTFSI. We dissolve the spiro-MeOTAD and lithium salt in chlorobenzene, and illuminate the solution for 20 minutes, and measure the absorbance profile. The ratio of spiro-MeOTAD to lithium salt was held fixed at the usual 6.2:1 ratio. As shown in Figure 3.16, LiCl could not induce any photo-oxidation due to its extremely poor solubility in chlorobenzene. Indeed, the addition of a dilute LiCl solution to spiro-MeOTAD yielded a cloudy mixture. However three other lithium salts all revealed the same spiro-MeOTAD$^+$ signature absorption peak at 525 nm as observed for LiTFSI. However the amplitude of the peak was roughly half that obtained for LiTFSI. These results suggest that the lithium cation can photo-oxidize the spiro-MeOTAD but that the doping concentration is strongly depended upon the counter anion. We conclude that the TFSI anion stabilizes the spiro-MeOTAD$^+$ in chlorobenzene better than the other counter anions. The order of stabilization ability is LiTFSI>$LiCF_3SO_3$ = $LiBF_4$= $LiClO_4$>LiCl.

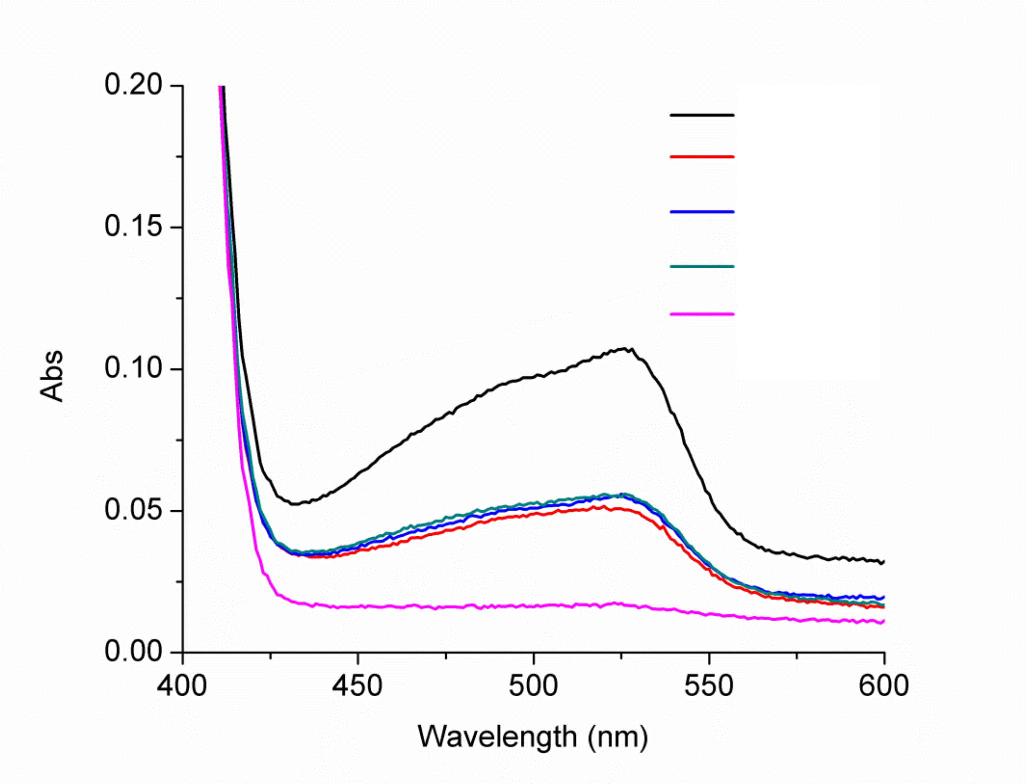

Figure 3.16 Absorption spectra of chlorobenzene solution of spiro-MeOTAD with five different lithium salts, each in a 6.2:1 ratio to spiro-MeOTAD.

We also performed in-situ studies of the ss-DSSC performance after open-circuit illumination with the different lithium salts. As shown in Figure 17, the LiTFSI-based ss-DSSC yielded the J-V plot with the highest performance. The other lithium salt-based ss-DSSC all exhibited much lower cell performance. We expect the drop-off in cell performance is due to the poor stabilization of other lithium salts compared to LiTFSI. The generated spiro-MeOTAD$^+$ will quickly recombine with electrons from TiO_2 with poor stabilization by other Li salts. This enhanced charge recombination resulted in a low V_{oc} in J-V plots. The poor current was because of poor conductivity by less spiro-MeOTAD$^+$, to be consistent with Figure 3.16. The overall efficiency calculated from J-V curves listed in sort: LiTFSI>>$LiCF_3SO_3$> $LiBF_4$> $LiClO_4$≈LiCl.

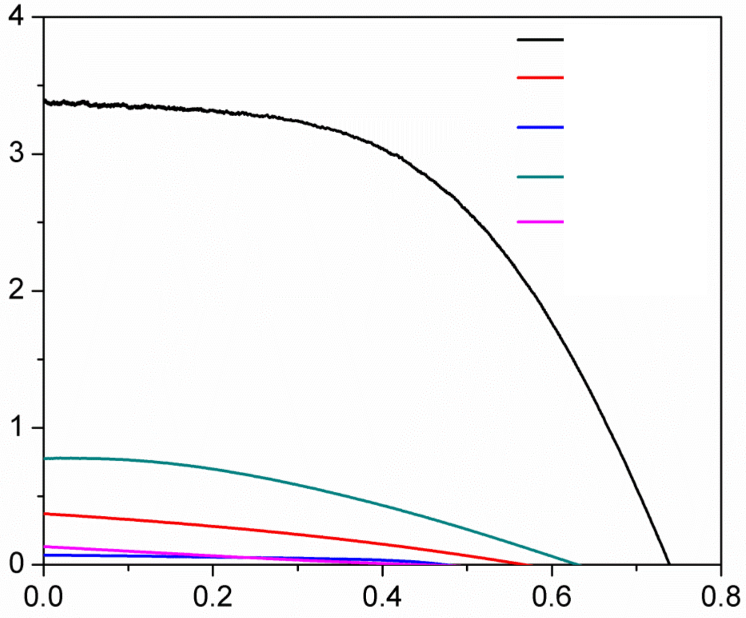

Figure 17. J-V curves of ss-DSSCs with different types of lithium salts.

Conclusion:

LiTFSI is a common performance enhancing additive for ss-DSSC, significantly improving cell conductivity and efficiency. A key issue is to understand the mechanism behind the increased conductivity, and the interaction of LiTFSI with the other components of ss-DSSC. Our key observation is that the cell performance improved after the ss-DSSC was illuminated under open-circuit conditions. After twenty minute short-circuit illumination the FF increased 36%, resulting in a 25% increasing of cell efficiency. To determine the mechanism for this optimization, we investigated the ex-situ dependence of absorption spectra of spiro-MeOTAD chlorobenzene solutions to time of illumination, lithium concentration, and frequency of illuminating light. We deduced that LiTFSI triggers a photo-oxidation of spiro-MeOTAD under short wave length light, and that dye is required to trigger the oxidation under longer wave-length light. We also inferred that the counter anion, TFSI serves to^{-} stabilize the spiro-MeOTAD^{+}.

For in-situ performance, we found a direct correlation between the presence of the oxidized state, spiro-MeOTAD^{+}, and an increase in FF of cell in J-V curve. Additionally, the oxidized state corresponded to a slight reduction of J_{SC} after short-circuit illumination. The absorbance of spiro-MeOTAD^{+} can compete with theN3 dye, leading to a lower photocurrent. However, through OCVD and EIS measurements, we found that presence of the oxidized state spiro-MeOTAD^{+} also lead to enhanced charge recombination, which lowers the J_{SC}. Besides LiTFSI, other lithium salts with different counter anions were investigated both ex-situ and

Experimental

3.4.1 Materials

Fluorine doped Tin Oxide (FTO) Glass purchased from Hartford was pretreated by Alconox, distilled water, acetone and UV-ozone before use. Spiro-MeOTAD was purchased from Lumtech. TiO_2 paste (Ti-Nanoxide T) was from Solaronix. Gold used as evaporation source for counter electrode was from Kurt J. Lesker. All other chemicals were purchased from Sigma Aldrich and were used as receive unless mentioned otherwise.

3.4.2 Instruments

Absorption spectra were obtained from Varian Carey Model 50 UV-Vis Spectrophotometer. The morphology of compact layer coated FTO glass was determined by a Hitachi S-4700 II field-emission scanning electron microscope (FESEM). Current-voltage measurements and open circuit voltage decay measurements of ss-DSSC were performed using a Xe Arc Lamp and CHI-650D Electrochemical work station. An AM 1.5 solar filter and neutral density filter were used to simulate sunlight at 100 mW cm^{-2}. A mask with an area of $0.25cm^2$ was used. A Horiba Jobin Yvon MicroHR was used for monochromatic light. The electrochemical impedance spectra (EIS) were carried out by applying bias from the open circuit voltage (~0.7 V) under fully dark condition, and the data were recorded over the frequency range 10^{-1}–10^{6} Hz with a 10 mV AC signal.

3.4.3 Solar cell fabrication and preparation

Devices of ss-DSSC were fabricated according to a procedure[25]. Briefly, a pre-cleaned FTO glass was put on a hot plate with a temperature of 500°C for 30 min before any deposition. A 200nm thickness of TiO_2 compact layer on FTO was formed by home-made spray-pyrolysis set-up using air as carrier gas and titanium di-isopropoxidebis (acetylacetonate) as precursor. A 2.5 µm thickness of mesoporous TiO_2 film was deposited by doctor-blading TiO_2 pastes with scotch tape as spacer. The thickness was measured by profilometer and confirmed by cross-section SEM image. After baking the TiO_2 paste with a programmable heating procedure up to 450°C, we let the substrate cooling down to 80 °C before soaking into a 0.3mM N3 dye ethanol solution. The dye soaking took about 16 hours at least, followed by rinsing with ethanol and acetonitrile. A chlorobenzene solution of spiro-MeOTAD or mixture of spiro-MeOTAD and silica/polymer were used for spin-coating on dye-coated TiO_2 substrates. The concentration of hole conductors was 120mg/mL in total with additives of lithium bis(trifluoromethylsulfonyl) imide (LiTFSI) and 4-tert butylpyridine (4-tBP). A 36 µL electrolyte solution firstly stood on the substrate for one minute and then was spin-coated with 2000 rpm for 30 seconds in air. The cell was stored under dark overnight before depositing the gold electrode. A 30 nm thickness of gold was applied by thermal evaporation as back contact.

REFERENCES

REFERENCES

(1) Bach, U.; Lupo, D.; Comte, P.; Moser, J. E.; Weissortel, F.; Salbeck, J.; Spreitzer, H.; Gratzel, M.: Solid-state dye-sensitized mesoporous TiO2 solar cells with high photon-to-electron conversion efficiencies. *Nature* **1998**, *395*, 583-585.

(2) Kroeze, J. E.; Hirata, N.; Schmidt-Mende, L.; Orizu, C.; Ogier, S. D.; Carr, K.; Gratzel, M.; Durrant, J. R.: Parameters influencing charge separation in solid-state dye-sensitized solar cells using novel hole conductors. *Adv Funct Mater* **2006**, *16*, 1832-1838.

(3) Poplavskyy, D.; Nelson, J.: Nondispersive hole transport in amorphous films of methoxy-spirofluorene-arylamine organic compound. *J Appl Phys* **2003**, *93*, 341-346.

(4) Snaith, H. J.; Gratzel, M.: Electron and hole transport through mesoporous TiO2 infiltrated with spiro-MeOTAD. *Adv Mater* **2007**, *19*, 3643-+.

(5) Rana, O.; Srivastava, R.; Grover, R.; Zulfequar, M.; Husain, M.; Kamalasanan, M. N.: Charge transport studies in thermally evaporated 2,2 ',7,7 '-tetrakis-(N,N-di-4-methoxyphenylamino)-9,9 '-spirobifluorene (spiro-MeOTAD) thin film. *Synthetic Met* **2011**, *161*, 828-832.

(6) Fabregat-Santiago, F.; Bisquert, J.; Cevey, L.; Chen, P.; Wang, M. K.; Zakeeruddin, S. M.; Gratzel, M.: Electron Transport and Recombination in Solid-State Dye Solar Cell with Spiro-OMeTAD as Hole Conductor. *J Am Chem Soc* **2009**, *131*, 558-562.

(7) Howie, W. H.; Claeyssens, F.; Miura, H.; Peter, L. M.: Characterization of solid-state dye-sensitized solar cells utilizing high absorption coefficient metal-free organic dyes. *J Am Chem Soc* **2008**, *130*, 1367-1375.

(8) Wang, M. K.; Gratzel, C.; Moon, S. J.; Humphry-Baker, R.; Rossier-Iten, N.; Zakeeruddin, S. M.; Gratzel, M.: Surface Design in Solid-State Dye Sensitized Solar Cells: Effects of Zwitterionic Co-adsorbents on Photovoltaic Performance. *Adv Funct Mater* **2009**, *19*, 2163-2172.

(9) Fabregat-Santiagoa, F.; Bisquert, J.; Palomares, E.; Haque, S. A.; Durrant, J. R.: Impedance spectroscopy study of dye-sensitized solar cells with undoped spiro-OMeTAD as hole conductor. *J Appl Phys* **2006**, *100*.

(10) Snaith, H. J.; Gratzel, M.: Enhanced charge mobility in a molecular hole transporter via addition of redox inactive ionic dopant: Implication to dye-sensitized solar cells. *Appl Phys Lett* **2006**, *89*.

(11) Schmidt-Mende, L.; Zakeeruddin, S. M.; Gratzel, M.: Efficiency improvement in solid-state-dye-sensitized photovoltaics with an amphiphilic Ruthenium-dye. *Appl Phys Lett* **2005**, *86*.

(12) Juozapavicius, M.; O'Regan, B. C.; Anderson, A. Y.; Grazulevicius, J. V.; Mimaite, V.: Efficient dye regeneration in solid-state dye-sensitized solar cells fabricated with melt processed hole conductors. *Org Electron* **2012**, *13*, 23-30.

(13) Wong, H. M. P.; Wang, P.; Abrusci, A.; Svensson, M.; Andersson, M. R.; Greenham, N. C.: Donor and acceptor behavior in a polyfluorene for photovoltaics. *J Phys Chem C* **2007**, *111*, 5244-5249.

(14) Snaith, H. J.; Zakeeruddin, S. M.; Wang, Q.; Pechy, P.; Gratzel, M.: Dye-sensitized solar cells incorporating a "liquid" hole-transporting material. *Nano Lett* **2006**, *6*, 2000-2003.

(15) Burschka, J.; Dualeh, A.; Kessler, F.; Baranoff, E.; Cevey-Ha, N. L.; Yi, C. Y.; Nazeeruddin, M. K.; Gratzel, M.: Tris(2-(1H-pyrazol-1-yl)pyridine)cobalt(III) as p-Type Dopant for Organic Semiconductors and Its Application in Highly Efficient Solid-State Dye-Sensitized Solar Cells. *J Am Chem Soc* **2011**, *133*, 18042-18045.

(16) Cai, N.; Moon, S. J.; Cevey-Ha, L.; Moehl, T.; Humphry-Baker, R.; Wang, P.; Zakeeruddin, S. M.; Gratzel, M.: An Organic D-pi-A Dye for Record Efficiency Solid-State Sensitized Heterojunction Solar Cells. *Nano Lett* **2011**, *11*, 1452-1456.

(17) Cappel, U. B.; Daeneke, T.; Bach, U.: Oxygen-Induced Doping of Spiro-MeOTAD in Solid-State Dye-Sensitized Solar Cells and Its Impact on Device Performance. *Nano Lett* **2012**, *12*, 4925-4931.

(18) Tiwana, P.; Docampo, P.; Johnston, M. B.; Herz, L. M.; Snaith, H. J.: The origin of an efficiency improving "light soaking" effect in SnO2 based solid-state dye-sensitized solar cells. *Energ Environ Sci* **2012**, *5*, 9566-9573.

(19) Gregg, B. A.; Chen, S. G.; Ferrere, S.: Enhanced dye-sensitized photoconversion efficiency via reversible production of UV-induced surface states in nanoporous TiO2. *J Phys Chem B* **2003**, *107*, 3019-3029.

(20) Wang, Q.; Zhang, Z. P.; Zakeeruddin, S. M.; Gratzel, M.: Enhancement of the performance of dye-sensitized solar cell by formation of shallow transport levels under visible light illumination (vol 112C, pg 7089, 2008). *J Phys Chem C* **2008**, *112*, 10585-10585.

(21) Duan, Y. G.; Zhou, Y.; Tang, Y. P.; Li, D. C.: Nano-TiO2-modified photosensitive resin for RP. *Rapid Prototyping J* **2011**, *17*, 247-252.

(22) Yu, J. G.; Zhao, X. J.; Zhao, Q. N.: Effect of surface structure on photocatalytic activity of TiO2 thin films prepared by sol-gel method. *Thin Solid Films* **2000**, *379*, 7-14.

(23) Abate, A.; Leijtens, T.; Pathak, S.; Teuscher, J.; Avolio, R.; Errico, M. E.; Kirkpatrik, J.; Ball, J. M.; Docampo, P.; McPherson, I.; Snaith, H. J.: Lithium salts as "redox active" p-type dopants for organic semiconductors and their impact in solid-state dye-sensitized solar cells. *Phys Chem Chem Phys* **2013**, *15*, 2572-2579.

(24) Zaban, A.; Greenshtein, M.; Bisquert, J.: Determination of the electron lifetime in nanocrystalline dye solar cells by open-circuit voltage decay measurements. *Chemphyschem* **2003**, *4*, 859-864.

(25) Snaith, H. J.; Humphry-Baker, R.; Chen, P.; Cesar, I.; Zakeeruddin, S. M.; Gratzel, M.: Charge collection and pore filling in solid-state dye-sensitized solar cells. *Nanotechnology* **2008**, *19*.

Chapter 4: Synthesis and characterization of the hole conducting silica/polymer nanocomposites: applications to solid-state dye-sensitized solar cell

Introduction:

Nanocomposites formed from hole conducting polymers anchored onto silica nanoparticles exhibit physical and chemical properties'[1,2] unattainable in the pure polymer state. The resulting materials have potential applications in the field of energy storage[1] and hybrid solar cells[2]. In this chapter, we use surface-initiated polymerization to anchor hole conducting polymersonto silica nanoparticles. The strong covalent bond between polymer and silica particles yields a material with enhanced chemical and thermal stability. In particular, we investigate the performance of these nanocomposites mixed with spiro-MeOTAD (2, 2', 7, 7' -tetrakis (N, N-di-p-methoxyphenylamine) 9, 9'-spirobifluorene) as a new type of hole conductor for solid-state dye-sensitized solar cell (ss-DSSC). We argue that the formation of silica/polymer composites serve as a light scattering layer on the top of photoanode, raising the short circuit current by 26% over conventional spiro-MeOTAD ss-DSSCs while enhancing the overall power conversion efficiency. Notably, this is the first application of conductive light scattering layers in ss-DSSC to enhance cell performance. In this introduction, I first focus on the synthesis of organic/inorganic hole-conducting nanocomposite. Subsequently, I briefly discuss the use of triphenylamine units as hole-conducting blocks in ss-DSSCs.

In the past decade, increasing attention has been paid to the preparation and application of organic/inorganic nanocomposite materials in ss-DSSCs[3-5]. Here “organic” refers to organic molecules or polymers while the term “inorganic” includes silica[5], metal[6], quantum dots[7], metal oxide semiconductor[8] and magnetic nanoparticles[9]. These composite materials are synthesized through physical blends, interfacial interactions, and in-situ polymerization and they offer different thermal and mechanical properties which can be optimized for biomedical and electrical applications. The grafting of different functional organic layers onto the silica particles represents a significant breakthrough in the quest for low-cost alternatives to multi-functional material. These grafted composite materials exhibit good thermal, chemical and optical stability with well-defined, size-tuneable structure[5].

Hybrid, hole-conducting silica-based nanocomposites are produced by grafting a hole conducting polymer onto a silica core structure. The conducting shell layer is typically comprised of polypyrrole[10], polyaniline[11,12], or polythiophene[13], and the conventional grafting strategy is based upon in-situ oxidative polymerization[10-13]. For example, polythiophene-coated silica nanocomposite are synthesized from direct dispersion polymerization of thiophene monomers using ammonium peroxodisulfate as an oxidant[13]. However, the mechanism of grafting in this procedureis mainly attributable to non-covalent bonding due to electrostatic interactions[12], with either extensive washing or ultra-sonication leading to potential delamination of the polymer layer. On the other hand, the grafting of polymers from a surface initiator forms a strong covalent bond between substrate surface and polymer shell which is robustly stable to mechanical perturbations. The most widely used grafting method is via controlled living radical polymerization (CLRP)[14-21]. Among different CLRP methods, nitroxide mediatedpolymerization (NMP)[20-23] is especially attractive due to the fine control it provides over the molecular weight of the grafted polymers, the facile polymerization of styrene-like monomer, and the feasibility of metal-free polymerization.

Triphenylamine is one of the most common building blocks for hole conducting polymers. It is widely utilized in the production of organic light-emitting diodes[24], polymer solar cell[25] and ss-DSSC[26-29]. To date the record efficiency for an ss-DSSC is 7.2%, held by Grätzel's group[28]; however this level is still below that required to spur wide spread manufacturing demand. Spiro-MeOTAD[26,27] incorporates four triphenylamine units and is one of the most promising hole conducting materials developed so far. However it is expensive and offers low photocurrent and relatively high charge recombination as compared to liquid based DSSCs. These issues have inhibited the advancement of ss-DSSC over the past decade.

In this chapter we present asuccessful route to the synthesis of thermally stable poly (triphenylamine) grafted-silica nanoparticles via a surface-initiated nitroxide mediated polymerization (SI-NMP). We blend the nanoparticles with spiro-MeOTAD and the resulting silica/polymer nanocompositeis employedin the manufacture of ss-DSSCs. The composite material reduces the cost of the ss-DSSC by lowering the spiro-MeOTAD loading, while the nanoparticles enhance the cell's performance by serving as a light scattering layer.

Results and Discussion

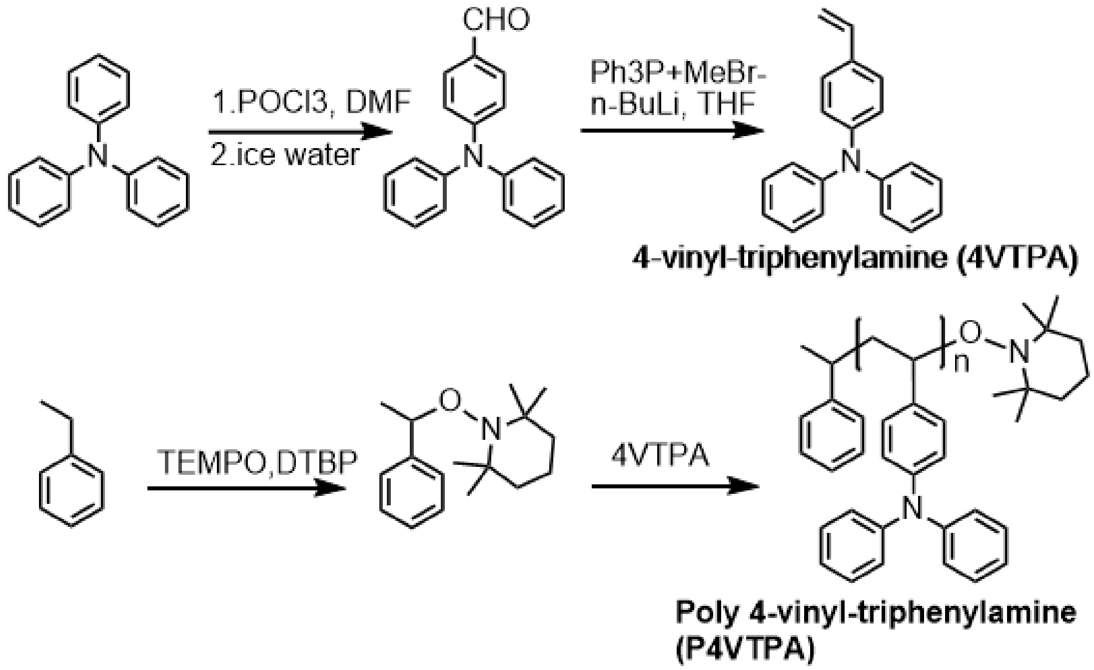

Scheme 4.1 Synthesis of 4-vinyl-triphenylamine (4VTPA) and poly 4-vinyl-triphenylamine (P4VTPA)

Synthesis and characterization of silica/polymer nanocomposites

The synthetic route for the production of both themonomer and the free polymer are shown in scheme 4.1. The monomer, 4-vinyl-triphenylamine (4VTPA) was readily prepared in two steps from commercially available triphenylamine following a standard procedure[30]. The vinyl group on the triphenylamine was used asthe functional group for polymerization. The free polymer(P4VTPA) was prepared by NMP using an alkoxyamine derivative as a unimolecular initiator according to Hawker's procedure for polystyrene[22]. A GPC analysis shows that the polymer has a molecular weight of Mn=11000g/mol with a low polydispersity index (PDI) of 1.07 after purification. The free polymer is used as a reference standard against which the chemical structure and thermal properties of the silica/polymer nanocomposites are compared. The silica/polymer nanocomposites were synthesized by SI-NMP. We found that a thermal initiator such as azobis (isobutyronitrile) (AIBN) combined with a nitroxide such as 2, 2, 6, 6-tetramethyl-1-1piperdinyloxy (TEMPO) or its alkoxyamine derivative served toefficiently initiate and control the polymerization. However, the reaction proceeded slowly because of a low polymerization rate since the surface-initiated polymerization occurred at the solid-liquid interface. The equilibrium constant for the phosphonylated nitroxide-based polymerization was 1000 fold larger than the polymerization using TEMPO as initiator[31], which allowed the polymerization took place much faster. In prior work, Bartholome and coworkers[20,32] reported using N-tert-butyl-N-[1-diethylphosphono(2,2-dimethylpropy)] nitroxide (DEPN) as a surface initiator to grow styrene on silica nanoparticles successfully. We optimized their procedure, using 4VTPA as the monomer instead of styrene. As illustrated in Scheme 4.2, the surface-initiated polymerization proceeds in two steps: (1) in-situ attachment of the acrylic phosphonylated alkoxyamine onto the surface of the silica, and (2) growth of triphenylamine polymer from silica nanoparticles.

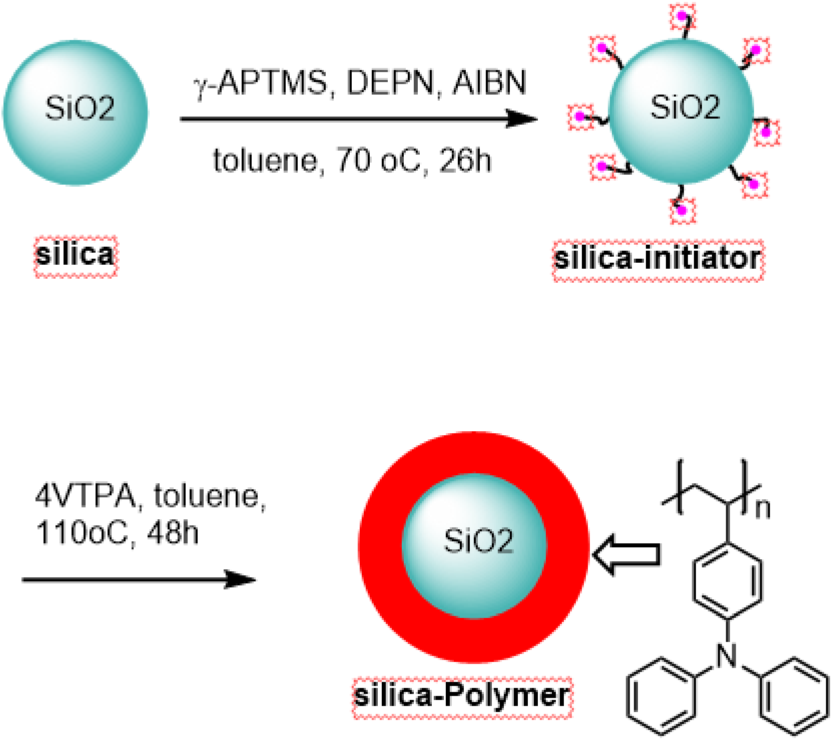

Scheme 4.2 Two steps in the synthesis of the silica-P4VTPA nanocomposite.

Figure 4.1 shows the FTIR spectra of the materials at different stages. The spectrum of bare silica displays a broad peak in the 3000-3600 cm^{-1} range, indicating O-H stretching. This hydroxyl signal is attributed to the silanol group and the physisorbed moisture from silica. Additionally, the peaks centered at 790cm^{-1}

and 1150cm^{-1} represent the Si-O stretching. After the immobilization of the initiator (Silica-DEPN),peaks associated to carbonyl ($v_{C=O}$, 1750cm^{-1}) and to the aliphatic group (v_{C-H}, 2900cm^{-1} and δ_{C-H}, 1360cm^{-1})appeared. Meanwhile, the absorbance of hydroxyl group from silica was seen to decrease due to the consumption of the silanol group. The silica-DEPN structure can also be resolved by XPS analysis. In Figure 4.2, the peaks at 530, 285, 270, 115, 24 eV correspond to the O1s, C1s, Si2s, Si2p and O2s of the silica particles and grafted initiator, respectively. The peaks at 402, 190, and 135 eV are attributed to the N1s, P2s and P2p from the grafted initiator, phosphonylated nitroxide. (See the structure inset). Figure 4.3 presents an XPS analysis of the carbon level of the silica initiator on the silica particles. This narrowly focused scan again confirmed the silica initiator structure. The binding energy of C 1s derived from the C-P bond at 283.05 eV, the C–C bond at 284.70 eV, the C≡N group with C-N bond at 286.20 eV, C-O bond at 287.70 eV and C=O bond at 289.20 eV. The FTIR spectrum of silica/polymer composites (Silica-P4VTPA) showed sp2 and sp3 C-H signals at 3050 and 2800 cm^{-1}that are attributed to the polymer chain and backbone. In addition, bands around 1600, 1500 cm^{-1} (C-C in aromatic ring), 800, 750, 700 cm^{-1} (substituted pattern of benzene ring) were consistent with the grafting of the polymer structure onto the silica. An FTIR spectrum of the free P4VTPA in Figure 4.1 was used as reference here. These data confirmed the successful grafting of the P4VTPA onto the silica nanoparticles.

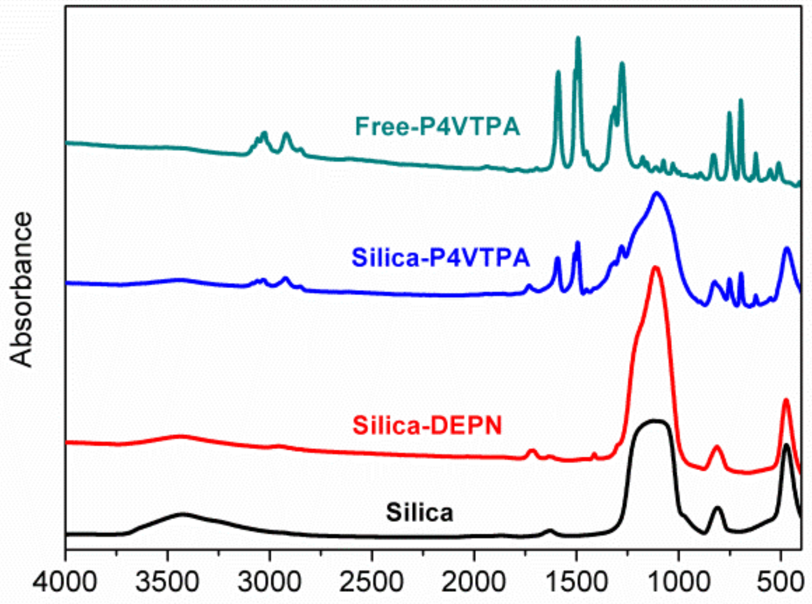

Figure 4.1 FTIR spectra of bared silica, silica-DEPN, silica-P4VTPA, and free-P4VTPA (from bottom to top).

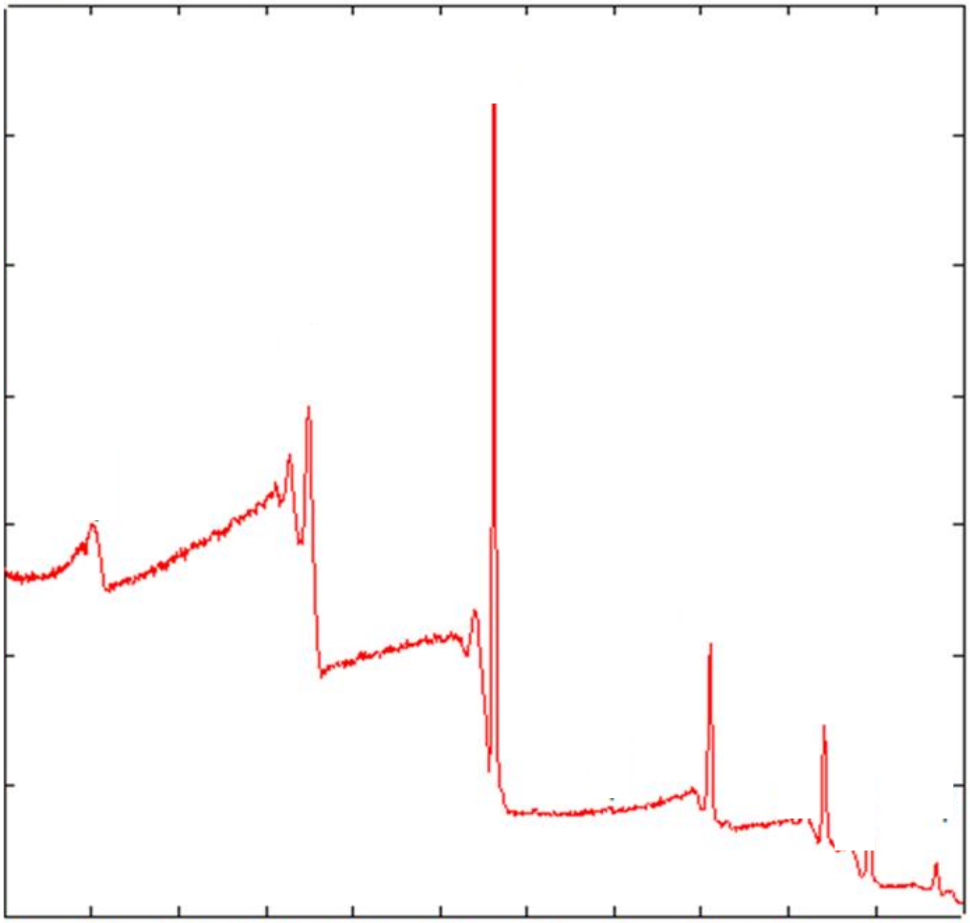

Figure 4.2 A wide scan result of XPS spectra of silica-initiator (Silica-DEPN, inset structure).

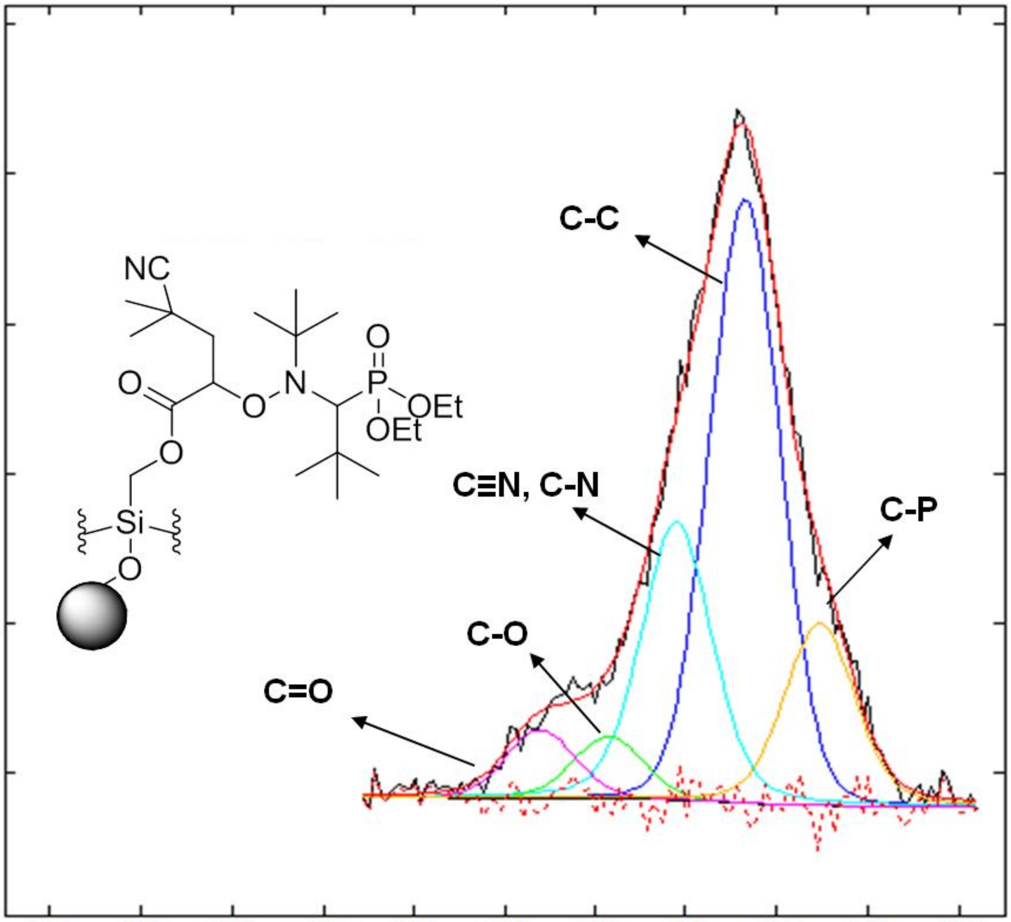

Figure 4.3 A narrow scan result of XPS C1s spectra of silica initiator (Silica-DEPN, inset structure).

The bare silica nanoparticles had an initial particle size of 8-12 nm. After the immobilization and surface polymerization the silica/polymer particles agglomerated; achieving a well-separated dispersion required additional steps such as precipitation, washing, centrifuging, and drying. A DLS (dynamic light scattering) analysis of the silica/polymer nanocomposites in a diluted solution yielded a particle size around 300 nm in diameter.

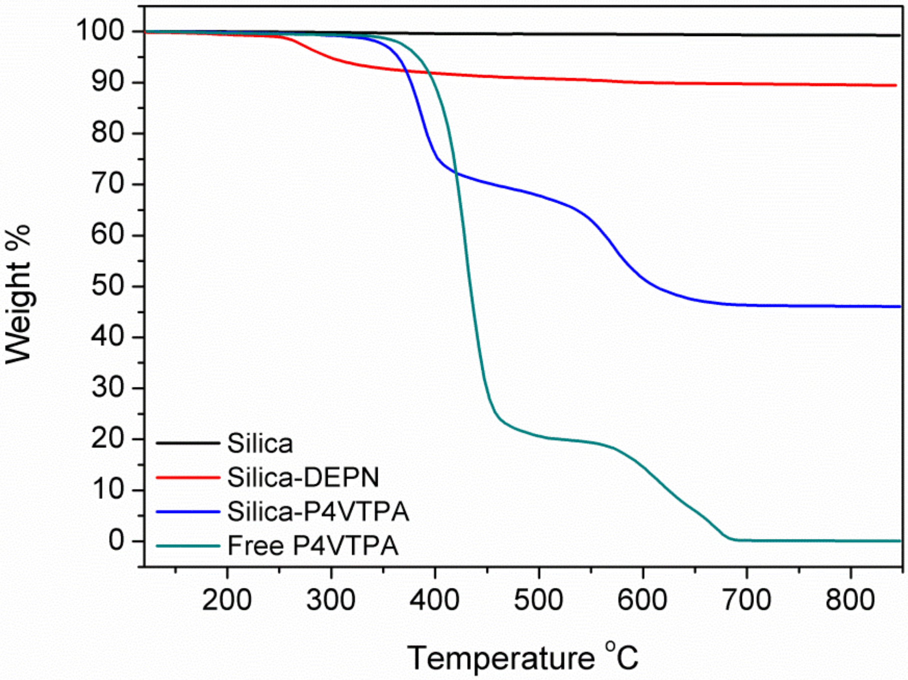

Figure 4.4 TGA curves for bared silica, silica-DEPN, silica-P4VTPA, and free-P4VTPA.

Thermal stability of silica/polymer nanocomposite

Figure 4.4 shows the thermal degradation of the silica/polymer nanocomposites obtained from a TGA analysis. The sample weight was recorded as the temperature was increased from 120°C to 850°C under air. At the final temperature all organic components will be oxidized to a gas phase with only the silica core remaining. We found that silica-DEPN decomposed at 250 °C with a weight loss of 11%. For the polymer/silica nanoparticles decomposition was observed at 350°C, leading to a 55% weight loss after two-step degradation. The first step was probably the decomposition of the polymer side chains while the second step corresponded to the combustion of polymer backbone. The reference curve of free polymer is displayed for comparison.

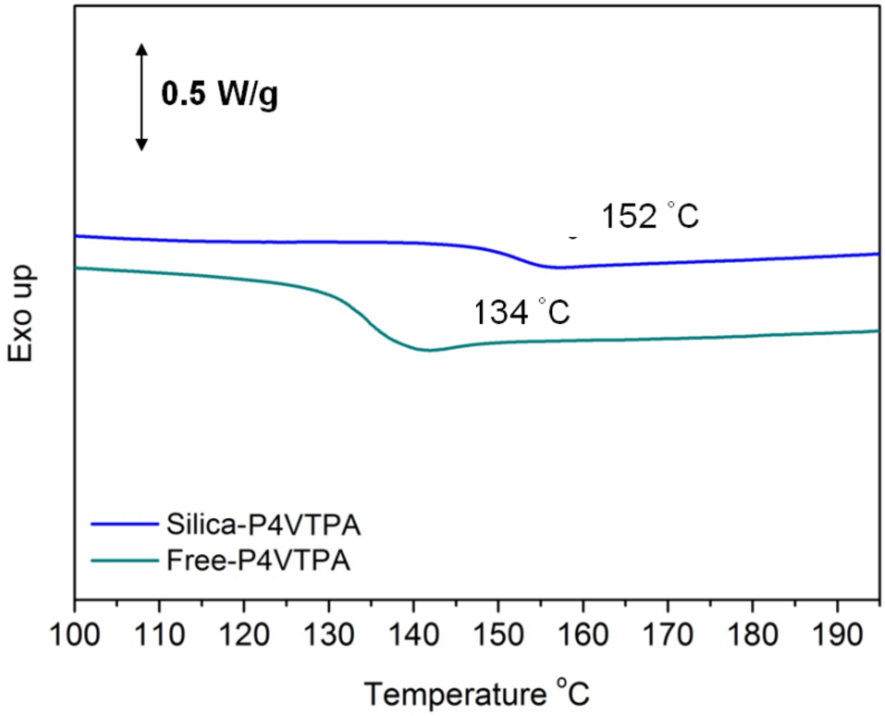

Figure 4.5 DSC curves of free polymer and silica/polymer nanocomposites.

Figure 4.5 displayed differential scanning calorimetry (DSC) curves of both free-P4VTPA and silica-P4VTPA. It clearly reveals a glass transition temperature (T_g) for the silica/polymer composites at 152 °C without any occurrence of crystallization. This is beneficial for ss-DSSC performance as the corresponding fully amorphous state will be compatible with other components, minimizing the possibility of void spaces between the composite and the electrodes. We remark that the anchored polymer has a 20 degree larger T_g than the free polymer, which is consistent with restricted movement of the polymer chain induced by the silica nanoparticles[33]. Both TGA and DSC results demonstrate excellent thermal stability of the silica/polymer nanocomposite, suggesting their suitability for ss-DSSC's fabrication and operation.

We employed an N3 ruthenium dye in our cell fabrication; this is the most widely used light absorber in DSSC. The photoanode was made by sintering A TiO_2 paste (Ti-Nanoxide T), obtained from Solaronix, onto the FTO. A mixture of spiro-MeOTAD and silica/polymer nanocomposites was used as the electrolyte. The counter electrode was comprised of a 30 nm gold layer applied on top of capping layer, in Figure 4.6.

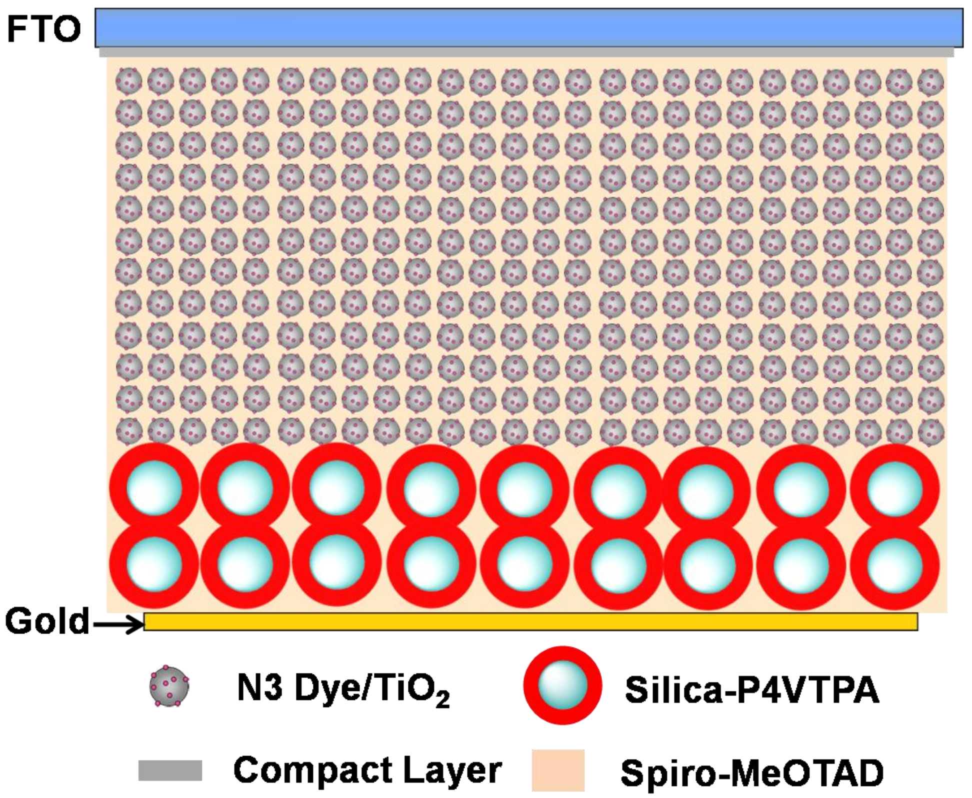

Figure 4.6 Illustration of ss-DSSC with a capping layer comprised of silica-P4VTPA.

Cell performance

It is established in the literature that incomplete filling of hole-conductor into the pores of the mesoporous TiO_2 is a principle contributor to inefficient dye regeneration in ss-DSSCs[29,34]. A hole-conducting polymer with a small radius of gyration is required to achieve a complete infiltration into the porous TiO_2. Given the large size of the silicia/polymer nanoparticles, we combined it with spiro-MeOTAD. The smaller spiro-MeOTAD polymers effectively interpenetrate the TiO_2, while providing good ionic connection with the nanoparticles. Figure 4.6

provides a device-level illustration of the ss-DSSC basing upon this hole-conducting mixture. A chlorobenzene solution of hole conductor mixture was applied via a spin-coating procedure to the dye-coated TiO_2. As depicted in Figure 4.6, the smaller spiro-MeOTAD molecules penetrate throughout the porous TiO_2, while the larger hole-conducting silica/polymer nanocomposites remain on top of the TiO_2 forming a capping layer which serves to form an electronic barrier between the TiO_2 and the counter electrode, while serving as an efficient hole-conductor and as a light scatterer. These statements are further supported by an examination of the cross-sectional SEM image (Figure 4.7) of the ss-DSSC. Good penetration of the spiro-MeOTAD into the TiO_2 pores can be clearly seen, while a 2 μm silica/polymer nanocomposite layer is seen on top of the TiO_2. Prior results suggest an optimal capping layer thickness of 100-400 nm. The capping layer thickness can be controlled by adjusting the hole-conductor concentration and spin-coating rate[34,35]. Both photocurrent and fill factor are known to increase with decreasing capping layer width since a thicker capping layer results in a higher internal resistance. In our system, a 2 μm capping layer is optimal and a study of the capping layer's thickness and deposition method are part of ongoing research.

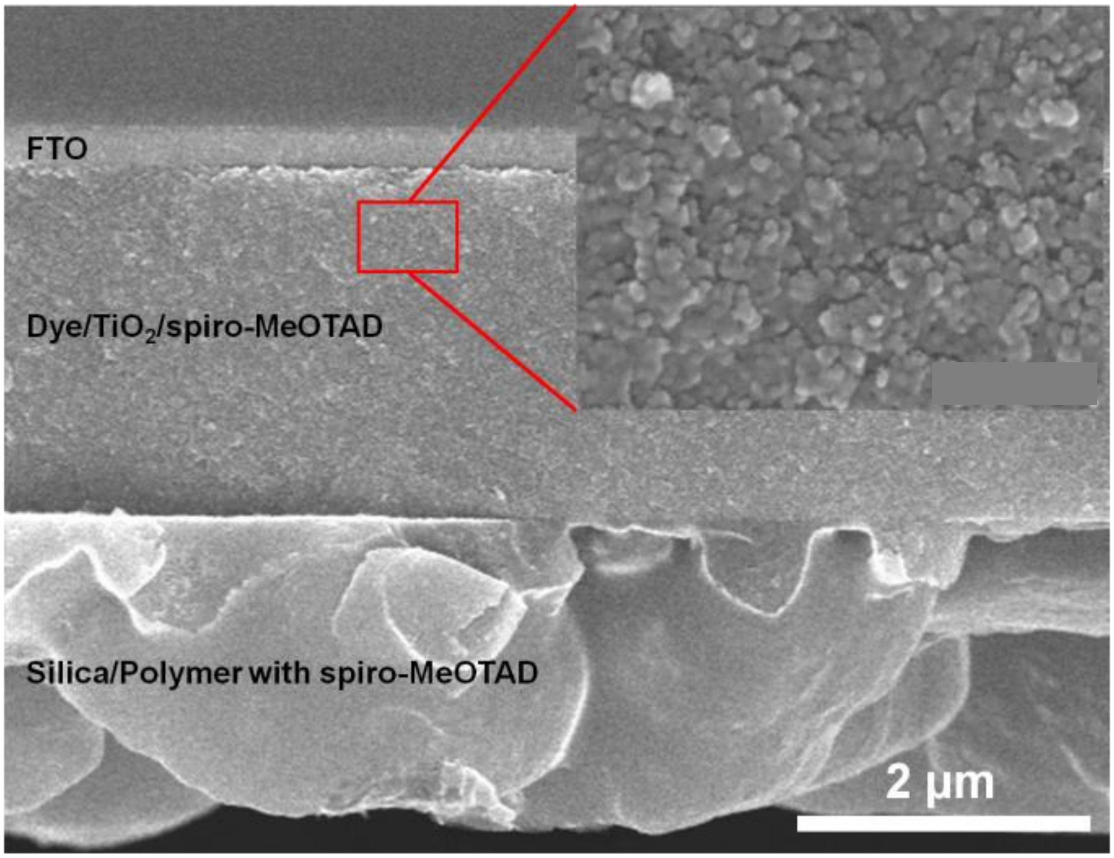

Figure 4.7 SEM image of cross-sectional structure of ss-DSSC (Inset: demonstration of spiro-MeOTAD penetration into the TiO_2 pore)

To examine the impact of the capping layer on cell performance we assembled and measured the performance of three different types of devices (Figure 4.8). The first cell type (Type I) used only spiro-MeOTAD as the electrolyte; the other two cells, (Type II and Type III) were constructed using an electrolyte mixture of spiro-MeOTAD and nanocomposites with weight ratios 1:1 and 3:1 respectively. In addition, we mixed spiro-MeOTAD with bare silica nanoparticles to serve as a control, but silica particles do not disperse well in chlorobenzene without the grafted polymer layer, We replaced the cholorobenzene with DMF in the fabrication; however, only a negligible efficiency was observed. We conjecture that the small silica particles occupied the TiO_2 pores, inhibiting the penetration of the spiro-MeOTAD and interrupting the conduction paths.

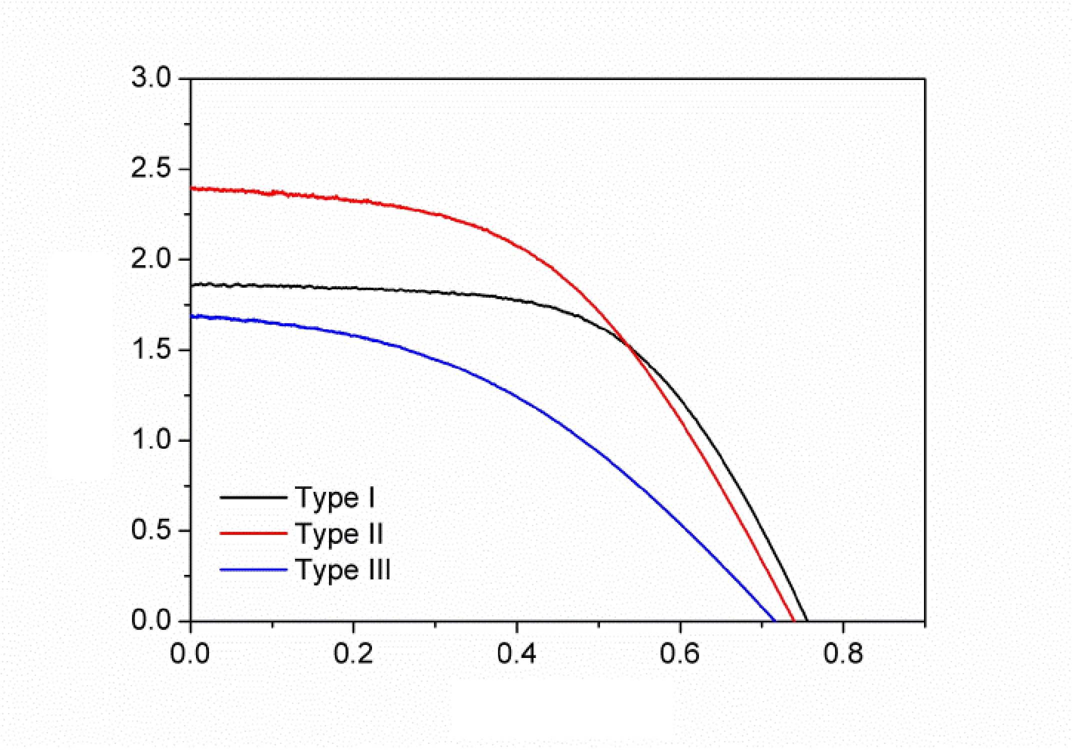

Figure 4.8 J-V curves of ss-DSSC with the three different types of hole conductors.

Table 4.1 Summary of three types of solar cell's performance.

	^{a}Silica-P4VTPA (%)	J_{SC} (mA/cm^2)	V_{OC} (V)	FF	η (%)
Type I	0%	1.9	0.76	0.58	0.84
Type II	50%	2.4	0.74	0.49	0.87
Type III	25%	1.7	0.72	0.41	0.50

a: weight percentage of silica-P4VTPA in hole conductor mixture

The Type I, spiro-MeOTAD based ss-DSSC fabricated in our lab gave a power conversation efficiency of 0.84%, which is below the literature level of approximately 3%. This is reduction in performance can be attributed to the dye and TiO_2 paste chosen. Introducing the silica/polymer with spiro-MeOTAD in the Type II and Type III cells, we were able to decrease the overall loading of spiro-MeOTAD, thereby reducing the overall cost of the solar cell. For the Type II cells, the short circuit current density (J_{SC}) improved 26% from 1.9 mA/cm^2 to 2.6 mA/cm^2, while the fill factor (FF) decreased 15% and open circuit voltage (V_{OC}) decreased slightly compared to the pure spiro-MeOTAD based ss-DSSC (Table 4.1). The overall efficiency of the Type II cell increased comparing to the pure spiro-MeOTAD device. For the type II cell, the lower FF can be attributed to a lower hole mobility associated to the capping layer. The hole mobility of free polymer, P4VTPA is 3.1x10^{-6} cm^2/Vs[36], which is roughly 10 times less than the conductivity of spiro-MeOTAD[37]. However, FF went down with increasing particle contents (from Type II to Type III) in the capping layer. We thought it was due to additives adding to cells. While fabrication cell, we fixed the total weight of hole conductor from Type I to Type III with the same amount of lithium salts. For lithium salts to spiro-MeOTAD, the higher ratio leads to higher conductivity. Type II cell gave higher ratio than Type III if silica-polymer cannot be well-oxidized to radical cation. Indeed, the highest occupied molecular orbital (HOMO) level of P4VTPA is 0.2 eV lower than that of spiro-MeOTAD[36], which is also suggestive of a to lower charge-transport efficiency. We assume that the silica core does not have any effect on the carrier mobility of the grafted P4VTPA. We thus anticipated a greater internal resistance and a lower FF and J_{SC} into both the Type II and Type III cells.

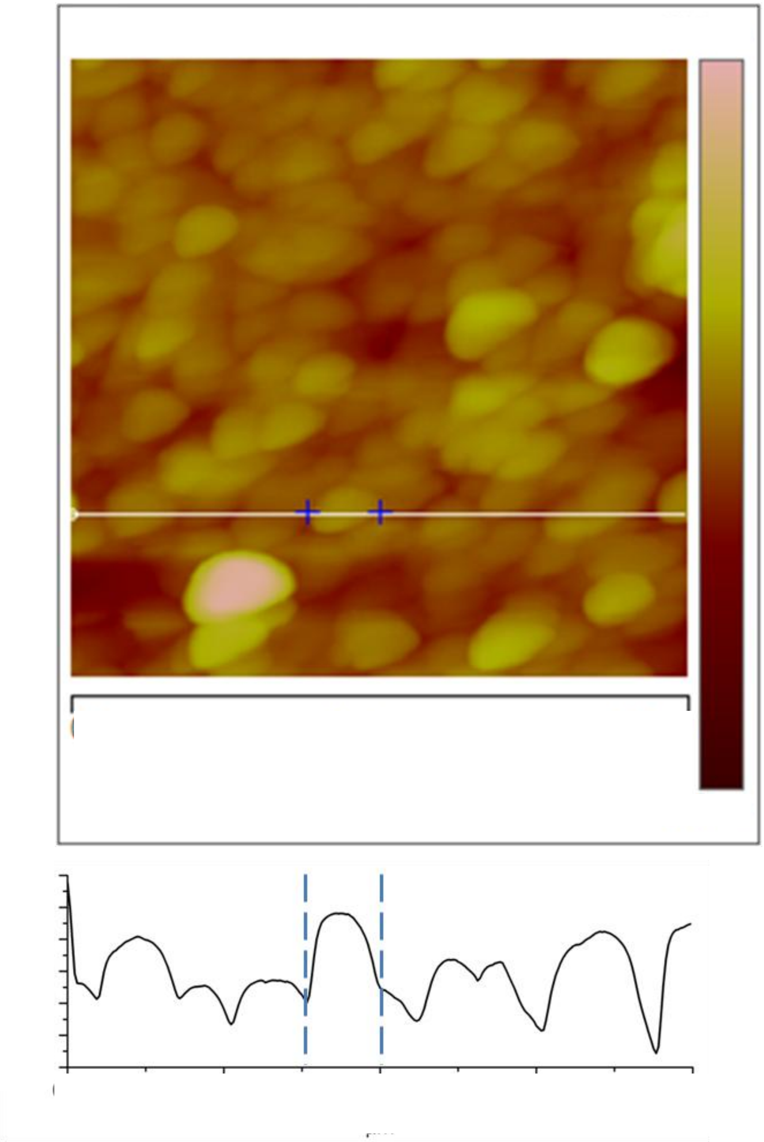

Figure 4.9 AFM image of silica/polymer nanocomposites as light scattering layer in ss-DSSC and corresponding linear cross-section profiles analysis.

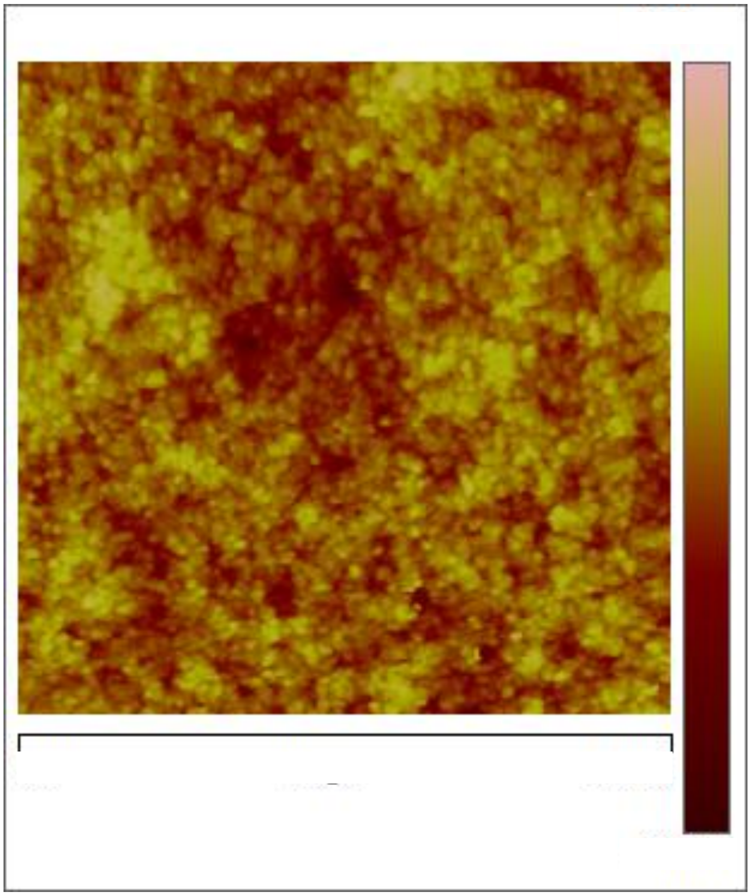

Figure 4.10 AFM image of TiO_2 coated with N3 dye.

The significant observation from Table 4.1 is that the photocurrent of the Type II cell increased significantly over that of the Type I or Type III cells. We attribute the increase in photocurrentover the Type I cell to extra photons captured due to back-scattering of light by capping layer. The AFM image of the capping layer presented in Figure 4.9, shows the silica/polymer nanoparticles which lie on top of the dye-coated TiO_2. The particles have a size distribution of 250-350 nm, consistent with our DSL data, and aggregate well with a local surface roughness of 8.1 nm. The morphology of the dye-coated TiO_2 was captured by the AFM image presented in Figure 4.10. It shows a pore size of 15-20 nanometers before the applicationof the capping layer.

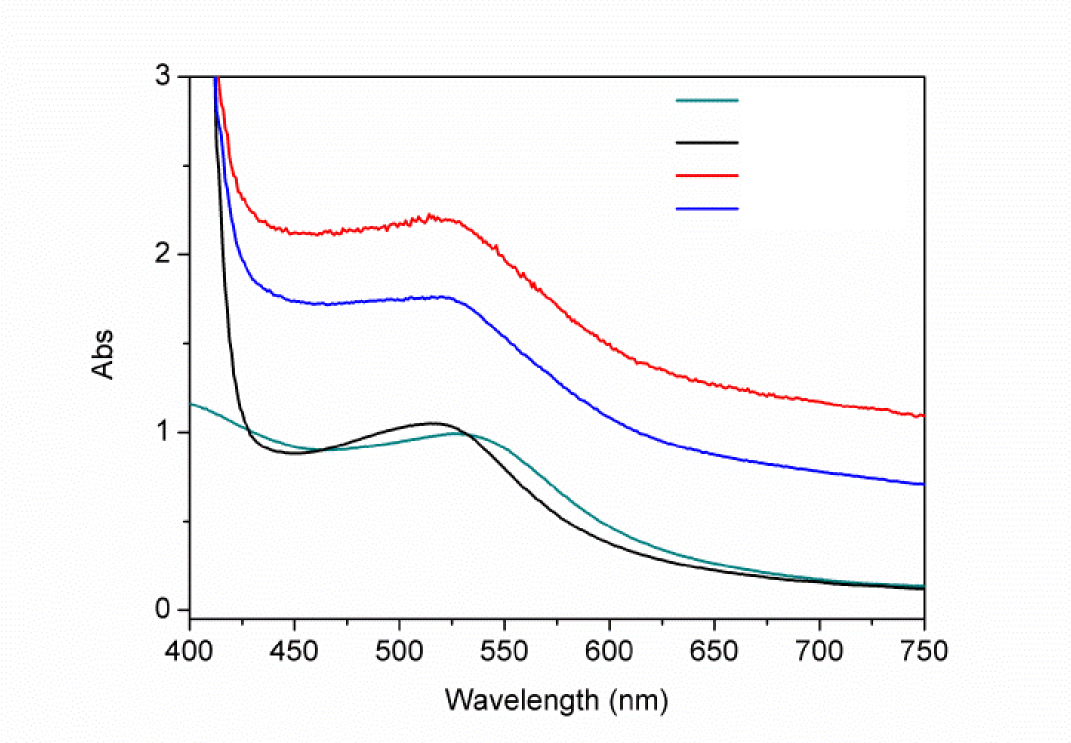

Figure 4.11 Absorption spectra of N3 dye coated TiO_2 on FTO and three types of solar cell without gold electrode.

To support our hypothesis of the light scattering mechanism of the silica/polymer nanoparticles, we measured the absorbance of the different devices using UV-Vis spectroscopy. Figure 4.11 presents the absorbance of the three types of ss-DSSC prior to the deposition of the gold electrode. An additional cell, with only the dye-coated TiO_2 on FTO glass, is shown as reference. The N3 dye coated-TiO_2 reference cell has an absorption peak at 535 nm. In comparison, the Type-I cell demonstrates a strong absorption peak at 425 nm, as is consistent with the presence of the triphenylamine units in spiro-MeOTAD. As the pure spiro-MeOTAD film is transparent to visible light, there are no additional peaks beyond 425nm for the Type-I cell. In addition, the broadening and blue shift of the peak at 520 nm is consistent with the formation of spiro-MeOTAD$^+$ under air[38]. The Type II and Type III cells also had a green light peak synonymous with the presence of N3 dyes; however the absorbance is markedly enhanced overall due to the light scattering by the large nanoparticles within the capping layer. Compared to Type III cell, the Type II cell showed better absorbance as is consistent with its higher loading of silica/polymer nanocomposites.

As additional evidence, we present Figure 4.12 that displays the incident photon-to-current conversion efficiency (IPCE) spectra for the three types of ss-DSSC. In the spectral region from 450 nm to 550 nm, the Type-II cell exhibited a higher IPCE values than either the Type-I or the Type-III cell. Moreover, in the near IR region, between 660 nm and 700 nm, the Type-II cell showed an additional small peak because of light scattering. The ICPE, absorption spectra, and J-V curves all present data that are consistent with the increase in back-scattering with thickness of the silica/polymer nanoparticle capping layer.

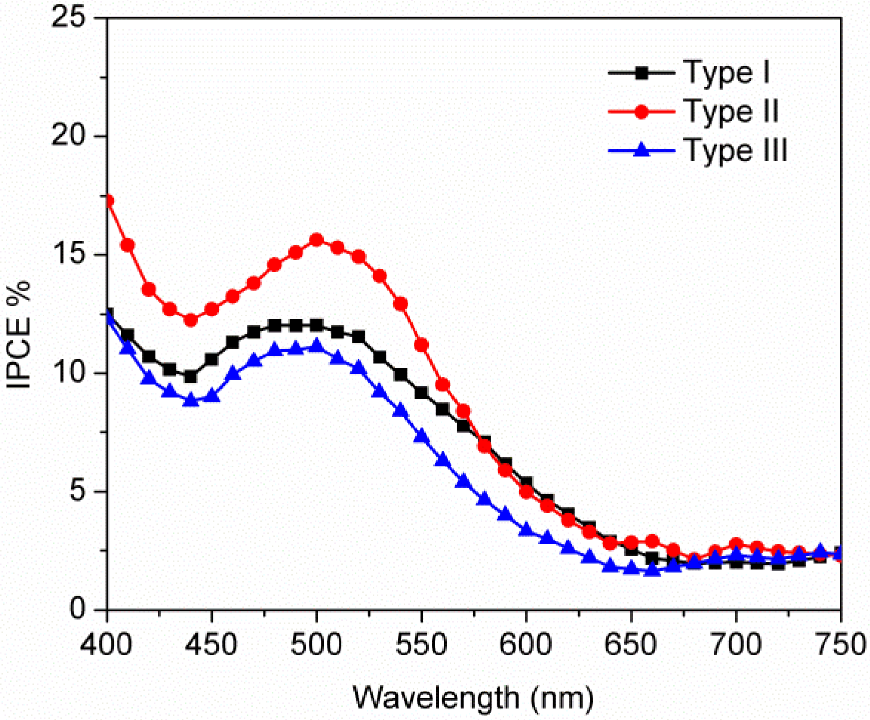

Figure 4.12 IPCE spectra of for the three types of ss-DSSC investgated.

There is a 20 mV reduction in V_{OC} of Type II compared to Type I. Is it well known in DSSCs, that decreases in open-circuit voltage can arise due to charge recombination[39,40]. Open-circuit voltage decay (OCVD) is a useful tool to collect information on charge recombination rates and electron lifetimes in DSSC[41]. A cell is subjected to a steady illumination which is then interrupted, and a potentiostat is used to monitor the decay of V_{OC} after the interruption. The decay of the V_{OC} reveals the rate of decrease of electron density in TiO_2 semi-conductor, which is largely attributed to charge recombination. The electron lifetime (τ) is defined as the reciprocal of the derivative of the decay curves normalized by the voltage. In general, longer electron lifetime relates to slower charge recombination in DSSC[41]. In Figure 4.13, τ is plotted versus V_{OC} for Type I and Type II cells. At a given V_{OC} especially below 480 mV, the results suggested faster charge recombination from TiO_2 to hole conductor in Type II than in Type I.

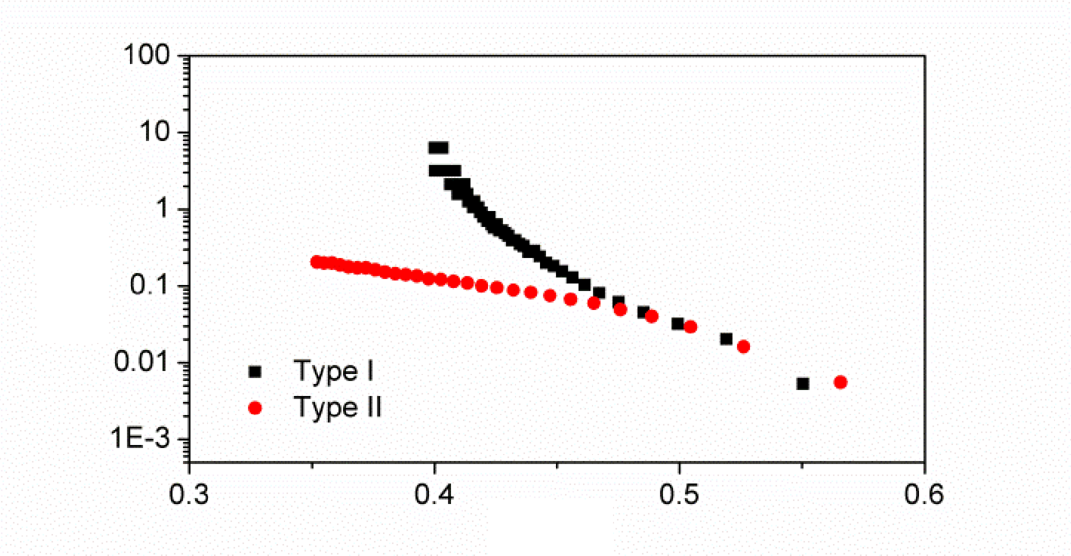

Figure 4.13 Electron lifetime(τ) derived from corresponding OCVD measurements as a function of V_{OC}.

Conclusions:

We successfully grafted poly (triphenylamine) onto the surface of silica nanoparticles using surface-initiated nitroxide mediated polymerization (SI-NMP). The solar cell of an electrolyte comprised of hole-conducting silica/polymer nanocomposite and spiro-MeOTAD was investigated. We assembled an ss-DSSC using only half of the typical load of spiro-MeOTAD, which achieved a power conversion efficiency higher than a pure spiro-MeOTAD-based ss-DSSC with a 26% improvement in photocurrent. We present IPCE and absorption data which supports our thesis that the enhanced photo-current is due to the back-scattering of light from the capping layer formed from the silica/polymer nanoparticles. To our knowledge, this is the first demonstration of enhanceperformance due to the use of aconductive light scattering layer. Unfortunately, the cell's efficiency was somewhat limited by the poor conductivity of silica/polymer composites, which resulted in a lower FF in the current-voltage curves. Ongoing research will focus on functionalizing triphenylamine with different groups to adjust the HOMO level, with the goal of aligning the energy level of different components in the solar cell, making the charge transport more efficiently.

Experimental

4.4.1 Materials

Aerosil 200 silica nanoparticle was a gift from Degussa. Fluorine doped Tin Oxide (FTO) Glass purchased from Hartford was pretreated by Alconox, distilled water, acetone and UV-ozone before use. Spiro-MeOTAD was purchased from Lumtech. TiO_2 paste (Ti-Nanoxide T) was from Solaronix. Gold used as evaporation source for counter electrode was from Kurt J. Lesker. All other chemicals were purchased from Sigma Aldrich and were used as receive unless mentioned otherwise.

4.4.2 Instruments

All Fourier transform infrared spectroscopy (FTIR) spectra were acquired from a Mattson Galaxy 300 spectrometer purged with dry nitrogen, with the signal averaging 128 scans. All IR samples were dried, ground and mixed with KBr and then pressed into pellets. Thermogravimetric analyses (TGA) were obtained in air using a Perkin-Elmer TGA 7. The heating rate is 10 °C/min, and samples were held at 120 °C for 30 min before running. Differential scanning calorimetry (DSC) measurements were carried out using a TA DSC Q100 with a heating/cooling rate of 10 °C/min under nitrogen. Absorption spectra were obtained from Varian Carey Model 50 UV-Vis Spectrophotometer. The molecular weights of polymers were determined by gel permeation chromatography (GPC) at 35 °C using two PLgel 10-lm mixed-B columns in series with THF as the eluting solvent. X-ray photoelectron spectroscopy (XPS) analysis was carried out in aPerkin Elmer Phi 5600 ESCA systemwith a magnesium Ka X-ray source. Dynamic light scattering (DLS) study was carried out on Malvern Zetasizer Nanoseries ZEN3600 instrument at 30 °C. Morphology of silica/polymer film was captured by Veeco Dimension 3100 scanning probe microscope. The cross-sectional structure of solar cell was determined by a Hitachi S-4700 II field-emission scanningelectron microscope (FESEM). The samples were soaked in liquid nitrogen before fracturing.

Current-voltage measurements and open circuit voltage decay measurements of ss-DSSC wereperformed using a Xe Arc Lamp and CHI-650D Electrochemical work station. An AM 1.5 solar filter and neutral density filter were used to simulate sunlight at 100 mW cm-2. A Horiba Jobin Yvon MicroHR was used for monochromatic light.

4.4.3 Synthesis

Synthesis of poly 4-vinyl-triphenylamine (P4VTPA): The recipe of free polymer followed a procedure of polystyrene by NMP[22]. In our case the monomer, 4-vinyl-triphenylamine and initiator were dissolved in dry, freshly distilled diglyme or toluene and polymerized in a Schlenk flask at 110 °C under nitrogen. After polymerized over 36 hours, the polymers were precipitated from acetone first and reprecipitated three times from THF/acetone. A Soxhlet extraction was used for further purification. The free polymer was dried by vacuum under 80°C at least 6 hours before any measurements.

Synthesis of silica/polymer nanocomposites: A surface-initiated NMP of 4-vinyl-triphenylamine here was carried out with silica initiator. The silica initiator and surface-initiated polymerization was prepared according to a literature procedure[20]. To a Schlenk flask equipped with a magnetic stirrer, was added silica initiator, monomer, and distilled toluene as solvent. The mixture was ultrasonicated for 5 min to make particles dispersed well in solvent. After three cycles of freeze-pump-thaw, the Schlenk flask was filled with nitrogen at room temperature and the polymerization started at 110 °C with rapid stirring. The polymerization was stopped after 48 hours. Then the silica nanoparticles were extensively washed-centrifuged by toluene and acetone for several times in order to removing the excess monomer and free polymer. The silica/polymer nanocomposites were finally dried by vacuum under 80oC at least 6 hours before any measurements.

4.4.4 Solar cell fabrication and preparation

Devices of ss-DSSC were fabricated according to a procedure[29]. Briefly, a pre-cleaned FTO glass was put on a hot plate with a temperature of 500°C for 30 min before any deposition. A 200nm thickness of TiO_2 compact layer on FTO was formed by home-made spray-pyrolysis set-up using air as carrier gasand titanium di-isopropoxide bis (acetylacetonate) as precursor. A 2.5 µm thickness of mesoporous TiO_2 film was deposited by doctor-blading TiO_2 pastes with scotch tape as spacer. The thickness was measured by profilometer and confirmed by cross-section SEM image. After baking the TiO_2 paste with a programmable heating procedure up to 450°C, we let the substrate cooling down to 80 °C before soaking into a 0.3mM N3 dye ethanol solution. The dye soaking took about 16 hours at least, followed by rinsing with ethanol and acetonitrile. A chlorobenzene solution of spiro-MeOTAD or mixture of spiro-MeOTAD and silica/polymer were used for spin-coating on dye-coated TiO_2 substrates. The concentration of hole conductors was 120mg/mL in total with additives of lithium bis(trifluoromethylsulfonyl) imide (LiTFSI) solution (26 µL/mL, LiTFSI pre dissolved in acetonitrile with a concentration of 170 mg/mL) and 4-tert butylpyridine (4-tBP) (12 µL/mL).A 36 µL electrolyte solution firstly stood on the substrate for one minute and then was spin-coated with 2000 rpm for 30 seconds in air. The cell was stored under dark overnight before depositing the gold electrode. A 30 nm thickness of gold was applied by thermal evaporation as back contact.

REFERENCES

REFERENCES

(1) Liu, G.; Xun, S. D.; Vukmirovic, N.; Song, X. Y.; Olalde-Velasco, P.; Zheng, H. H.; Battaglia, V. S.; Wang, L. W.; Yang, W. L.: Polymers with Tailored Electronic Structure for High Capacity Lithium Battery Electrodes. *Adv Mater* **2011**, *23*, 4679.

(2) Fan, B. H.; Mei, X. G.; Sun, K.; Ouyang, J. Y.: Conducting polymer/carbon nanotube composite as counter electrode of dye-sensitized solar cells. *Appl Phys Lett* **2008**, *93*.

(3) Sanchez, C.; Belleville, P.; Popall, M.; Nicole, L.: Applications of advanced hybrid organic-inorganic nanomaterials: from laboratory to market. *Chem Soc Rev* **2011**, *40*, 696-753.

(4) Chaudhuri, R. G.; Paria, S.: Core/Shell Nanoparticles: Classes, Properties, Synthesis Mechanisms, Characterization, and Applications. *Chem Rev* **2012**, *112*, 2373-2433.

(5) Zou, H.; Wu, S. S.; Shen, J.: Polymer/silica nanocomposites: Preparation, characterization, properties, and applications. *Chem Rev* **2008**, *108*, 3893-3957.

(6) Mandal, T. K.; Fleming, M. S.; Walt, D. R.: Preparation of polymer coated gold nanoparticles by surface-confined living radical polymerization at ambient temperature. *Nano Lett* **2002**, *2*, 3-7.

(7) Weaver, J.; Zakeri, R.; Aouadi, S.; Kohli, P.: Synthesis and characterization of quantum dot-polymer composites. *J Mater Chem* **2009**, *19*, 3198-3206.

(8) Nussbaumer, R. J.; Caseri, W. R.; Smith, P.; Tervoort, T.: Polymer-TiO2 nanocomposites: A route towards visually transparent broadband UV filters and high refractive index materials. *Macromol Mater Eng* **2003**, *288*, 44-49.

(9) Burke, N. A. D.; Stover, H. D. H.; Dawson, F. P.: Magnetic nanocomposites: Preparation and characterization of polymer-coated iron nanoparticles. *Chem Mater* **2002**, *14*, 4752-4761.

(10) McCarthy, G. P.; Armes, S. P.; Greaves, S. J.; Watts, J. F.: Synthesis and characterization of carboxylic acid functionalized polypyrrole silica microparticles using a 3-substituted pyrrole comonomer. *Langmuir* **1997**, *13*, 3686-3692.

(11) Gill, M.; Armes, S. P.; Fairhurst, D.; Emmett, S. N.; Idzorek, G.; Pigott, T.: Particle-Size Distributions of Polyaniline Silica Colloidal Composites. *Langmuir* **1992**, *8*, 2178-2182.

(12) Jang, J. S.; Ja, J.; Lim, B.: Synthesis and characterization of monodisperse silica-polyaniline core-shell nanoparticles. *Chem Commun* **2006**, 1622-1624.

(13) Han, M. G.; Armes, S. P.: Synthesis of poly(3,4-ethylenedioxythiophene)/silica colloidal nanocomposites. *Langmuir* **2003**, *19*, 4523-4526.

(14) Kim, J. B.; Bruening, M. L.; Baker, G. L.: Surface-initiated atom transfer radical polymerization on gold at ambient temperature. *J Am Chem Soc* **2000**, *122*, 7616-7617.

(15) Kim, J. B.; Huang, W. X.; Bruening, M. L.; Baker, G. L.: Synthesis of triblock copolymer brushes by surface-initiated atom transfer radical polymerization. *Macromolecules* **2002**, *35*, 5410-5416.

(16) Bao, Z. Y.; Bruening, M. L.; Baker, G. L.: Control of the density of polymer brushes prepared by surface-initiated atom transfer radical polymerization. *Macromolecules* **2006**, *39*, 5251-5258.

(17) Bao, Z. Y.; Bruening, M. L.; Baker, G. L.: Rapid growth of polymer brushes from immobilized initiators. *J Am Chem Soc* **2006**, *128*, 9056-9060.

(18) Pyun, J.; Jia, S. J.; Kowalewski, T.; Patterson, G. D.; Matyjaszewski, K.: Synthesis and characterization of organic/inorganic hybrid nanoparticles: Kinetics of surface-initiated atom transfer radical polymerization and morphology of hybrid nanoparticle ultrathin films. *Macromolecules* **2003**, *36*, 5094-5104.

(19) Bombalski, L.; Min, K.; Dong, H. C.; Tang, C. B.; Matyjaszewski, K.: Preparation of well-defined hybrid materials by ATRP in miniemulsion. *Macromolecules* **2007**, *40*, 7429-7432.

(20) Bartholome, C.; Beyou, E.; Bourgeat-Lami, E.; Chaumont, P.; Lefebvre, F.; Zydowicz, N.: Nitroxide-mediated polymerization of styrene initiated from the surface of silica nanoparticles. In situ generation and grafting of alkoxyamine initiators. *Macromolecules* **2005**, *38*, 1099-1106.

(21) Konn, C.; Morel, F.; Beyou, E.; Chaumont, P.; Bourgeat-Lami, E.: Nitroxide-mediated polymerization of styrene initiated from the surface of laponite clay platelets. *Macromolecules* **2007**, *40*, 7464-7472.

(22) Hawker, C. J.; Barclay, G. G.; Orellana, A.; Dao, J.; Devonport, W.: Initiating systems for nitroxide-mediated "living" free radical polymerizations: Synthesis and evaluation. *Macromolecules* **1996**, *29*, 5245-5254.

(23) Hawker, C. J.; Bosman, A. W.; Harth, E.: New polymer synthesis by nitroxide mediated living radical polymerizations. *Chem Rev* **2001**, *101*, 3661-3688.

(24) Kuwabara, Y.; Ogawa, H.; Inada, H.; Noma, N.; Shirota, Y.: Thermally Stable Multilayered Organic Electroluminescent Devices Using Novel Starburst Molecules, 4,4',4''-Tri(N-Carbazolyl)Triphenylamine (Tcta) and 4,4',4''-Tris(3-Methylphenylphenyl-Amino)Triphenylamine (M-Mtdata), as Hole-Transport Materials. *Adv Mater* **1994**, *6*, 677-679.

(25) Yasuda, T.; Shinohara, Y.; Matsuda, T.; Han, L.; Ishi-i, T.: Improved power conversion efficiency of bulk-heterojunction organic solar cells using a benzothiadiazole-triphenylamine polymer. *J Mater Chem* **2012**, *22*, 2539-2544.

(26) Bach, U.; Lupo, D.; Comte, P.; Moser, J. E.; Weissortel, F.; Salbeck, J.; Spreitzer, H.; Gratzel, M.: Solid-state dye-sensitized mesoporous TiO2 solar cells with high photon-to-electron conversion efficiencies. *Nature* **1998**, *395*, 583-585.

(27) Hsu, C. Y.; Chen, Y. C.; Lin, R. Y. Y.; Ho, K. C.; Lin, J. T.: Solid-state dye-sensitized solar cells based on spirofluorene (spiro-OMeTAD) and arylamines as hole transporting materials. *Phys Chem Chem Phys* **2012**, *14*, 14099-14109.

(28) Burschka, J.; Dualeh, A.; Kessler, F.; Baranoff, E.; Cevey-Ha, N. L.; Yi, C. Y.; Nazeeruddin, M. K.; Gratzel, M.: Tris(2-(1H-pyrazol-1-yl)pyridine)cobalt(III) as p-Type Dopant for Organic Semiconductors and Its Application in Highly Efficient Solid-State Dye-Sensitized Solar Cells. *J Am Chem Soc* **2011**, *133*, 18042-18045.

(29) Snaith, H. J.; Humphry-Baker, R.; Chen, P.; Cesar, I.; Zakeeruddin, S. M.; Gratzel, M.: Charge collection and pore filling in solid-state dye-sensitized solar cells. *Nanotechnology* **2008**, *19*.

(30) Xia, H. J.; He, J. T.; Xu, B.; Wen, S. P.; Li, Y. W.; Tian, W. J.: A facile convergent procedure for the preparation of triphenylamine-based dendrimers with truxene cores (vol 64, pg 5736, 2008). *Tetrahedron* **2008**, *64*, 7837-7838.

(31) Grimaldi, S.; Finet, J. P.; Le Moigne, F.; Zeghdaoui, A.; Tordo, P.; Benoit, D.; Fontanille, M.; Gnanou, Y.: Acyclic beta-phosphonylated nitroxides: A new

series of counter-radicals for "living"/controlled free radical polymerization. *Macromolecules* **2000**, *33*, 1141-1147.

(32) Bailly, B.; Donnenwirth, A. C.; Bartholome, C.; Beyou, E.; Bourgeat-Lami, E.: Silica-polystyrene nanocomposite particles synthesized by nitroxide-mediated polymerization and their encapsulation through miniemulsion polymerization. *J Nanomater* **2006**.

(33) Laruelle, G.; Parvole, J.; Francois, J.; Billon, L.: Block copolymer grafted-silica particles: a core/double shell hybrid inorganic/organic material. *Polymer* **2004**, *45*, 5013-5020.

(34) Ding, I. K.; Tetreault, N.; Brillet, J.; Hardin, B. E.; Smith, E. H.; Rosenthal, S. J.; Sauvage, F.; Gratzel, M.; McGehee, M. D.: Pore-Filling of Spiro-OMeTAD in Solid-State Dye Sensitized Solar Cells: Quantification, Mechanism, and Consequences for Device Performance. *Adv Funct Mater* **2009**, *19*, 2431-2436.

(35) Kim, H. S.; Lee, C. R.; Jang, I. H.; Kang, W.; Park, N. G.: Effect of Overlayer Thickness of Hole Transport Material on Photovoltaic Performance in Solid-Sate Dye-Sensitized Solar Cell. *B Korean Chem Soc* **2012**, *33*, 670-674.

(36) Barea, E. M.; Garcia-Belmonte, G.; Sommer, M.; Huttner, S.; Bolink, H. J.; Thelakkat, M.: Determination of charge carrier mobility of hole transporting polytriarylamine-based diodes. *Thin Solid Films* **2010**, *518*, 3351-3354.

(37) Poplavskyy, D.; Nelson, J.: Nondispersive hole transport in amorphous films of methoxy-spirofluorene-arylamine organic compound. *J Appl Phys* **2003**, *93*, 341-346.

(38) Cappel, U. B.; Daeneke, T.; Bach, U.: Oxygen-Induced Doping of Spiro-MeOTAD in Solid-State Dye-Sensitized Solar Cells and Its Impact on Device Performance. *Nano Lett* **2012**, *12*, 4925-4931.

(39) Haque, S. A.; Tachibana, Y.; Willis, R. L.; Moser, J. E.; Gratzel, M.; Klug, D. R.; Durrant, J. R.: Parameters influencing charge recombination kinetics in dye-sensitized nanocrystalline titanium dioxide films. *J Phys Chem B* **2000**, *104*, 538-547.

(40) Haque, S. A.; Palomares, E.; Cho, B. M.; Green, A. N. M.; Hirata, N.; Klug, D. R.; Durrant, J. R.: Charge separation versus recombination in dye-sensitized nanocrystalline solar cells: the minimization of kinetic redundancy. *J Am Chem Soc* **2005**, *127*, 3456-3462.

(41) Zaban, A.; Greenshtein, M.; Bisquert, J.: Determination of the electron lifetime in nanocrystalline dye solar cells by open-circuit voltage decay measurements. *Chemphyschem* **2003**, *4*, 859-864.

Chapter 5: Efficiency enhancement of ss-DSSC: heat-assisted infiltration of spiro-MeOTAD into TiO_2

Introduction:

Solid-state dye sensitized solar cells (ss-DSSC) suffer from incomplete pore-filling of the hole conductor into the mesoporous TiO_2[1-5], which leads to poor dye-regeneration and inhibits cell performance[6]. In this chapter, a simple strategy is presented which effectively increases the pore-filling fraction (PFF). Heating the cell during the fabrication process lowers the electrolyte viscosity and surface tension, enabling an 86% increase in cell efficiency and an 8 fold increasing of photocurrent over cells without heat treatment. We relate the enhancement in cell performance not only to the PFF of TiO_2 by spiro-MeOTAD, but also to morphological and thickness changes in the spiro-MeOTAD capping layer. In the introduction, we discuss limitations and challenges of ss-DSSC and describe our investigation of pore filling problem in ss-DSSC.

Ss-DSSCs using spiro-MeOTAD as the hole transport material (HTM) have achieved a cell efficiency of over 7%[7-11]. Compared to I^-/I^{3-} liquid electrolytes, the solid state HTM could avoids the problems of solvent leakage and evaporation. The solid-state cells have the potential for greater stability and longer cell lifetime, making them more suitable for use on buildings and other outdoor applications. However, ss-DSSCs are currently limited by poorer photocurrent due to the higher internal resistance of the hole-conducting polymer as measured against the ionic conductivity of the liquid cells. Alternatives to spiro-MeOTAD, such as polymers[12,13] or oligomers[1,14] with higher hole mobility, have been applied toss-DSSC, but their performance does not rival that of spiro-MeOTAD based ss-DSSC because the larger size of these polymer or oligomer structures inhibits their penetration into mesoporous TiO_2 structure, as depicted in Figure 4.1. Indeed it is not only charge mobility but also interfacial contact resistance that limits performance of ss-DSSC. When only limited amounts of HTM penetrate into the mesoporousTiO_2 there are gaps between the dye-coated $TiO_2$and the conductive polymer that result in poor contact between dye molecules and spiro-MeOTAD, inhibiting dye regeneration[2,6].

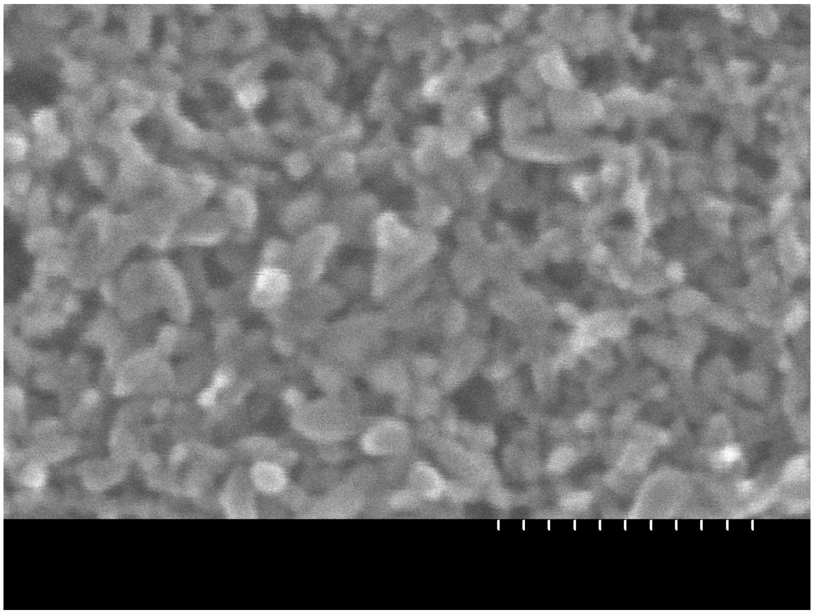

Figure 5.1 SEM image of mesoporous TiO_2 structure formed by sintering Ti-nanooxide_T paste.

Gratzel[1,2] and his coworkers were the first to study the pore-filling of spiro-MeOTAD and its related to the efficiency of ss-DSSC. By probing SEM cross-sectional image (Figure 5.2a) and photo-induced absorption spectroscopy[2,6], they suggested that both the device performance and conductivity went down with a thicker film device (Figure 5.2b). Balancing light absorption against spiro-MeOTAD penetration, they obtained a maximum cell efficiency with a 2-3 µm thickness of TiO_2 which had been treated with an amphiphilic dye that made the spiro-MeOTAD 'wet' the TiO_2 pore[8,9,15]. They found that for a 7µm thick TiO_2 layer, a large portion of the dye-coated TiO_2 close to the FTO was not filled by spiro-MeOTAD. By optimizing the spin-coating procedure, they were able to get the spiro-MeOTAD to filled 57% of the TiO_2 pore structure. In this manner they produced a 7 µm thick ss-DSSC with an incident photon-to-current efficiency (IPCE) of approximately 60%[2].

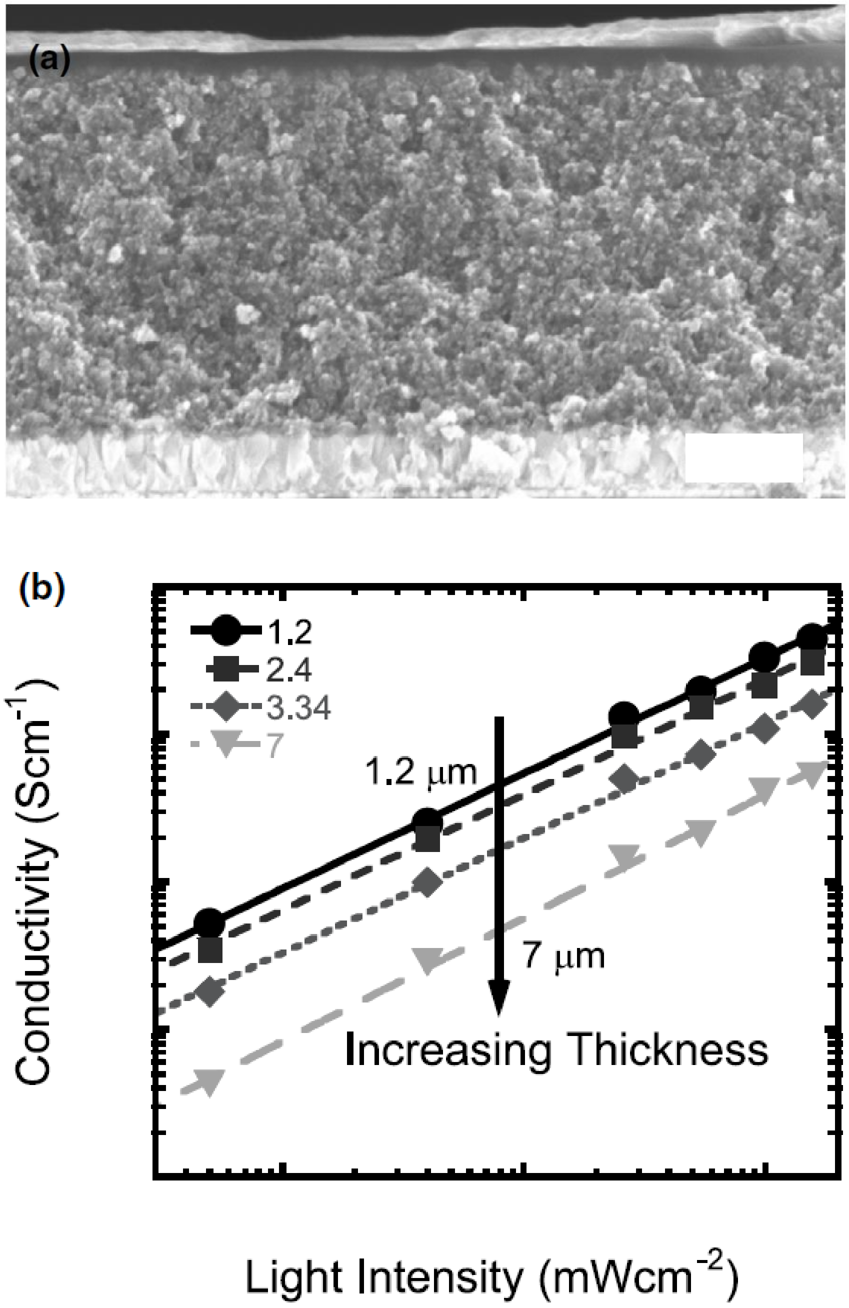

Figure 5.2 (a) cross-sectional SEM image of a 2 μm thick ss-DSSC; (b) Conductivity vs light intensity for devices comprised of mesoporous TiO_2 ranging from 1.2 to 7 μm thickness (see legend) with spiro-MeOTAD.

Subsequently, McGehee's group[3,4,16] extensively studied the PFF in mesoporous TiO_2 films with spiro-MeOTAD, quantitatively determined the PFF using X-ray photoelectron spectroscopy (XPS) depth profiling in conjunction with UV-vis absorption spectroscopy. They showed that as the PFF of spiro-MeOTAD increased from 26% to 65%, the cell efficiency increased by nearly 300% (see Figure 5.3). Moreover they determined that when the spiro-MeOTAD PFF reached 65%, the electron diffusion length was approximately 7 μm[4]. This suggested that the TiO_2 thickness, typically (2-3 μm), could be doubled without addition diffusive losses, which would potentially enhance the photocurrent of the ss-DSSC by increasing the photonic capture rate. Very recently, Snaith's group determined the PFF via optical reflectometry, which does not require any assumptions on materials properties, and re-estimated the PFF of ss-DSSC's at about 80%[5].

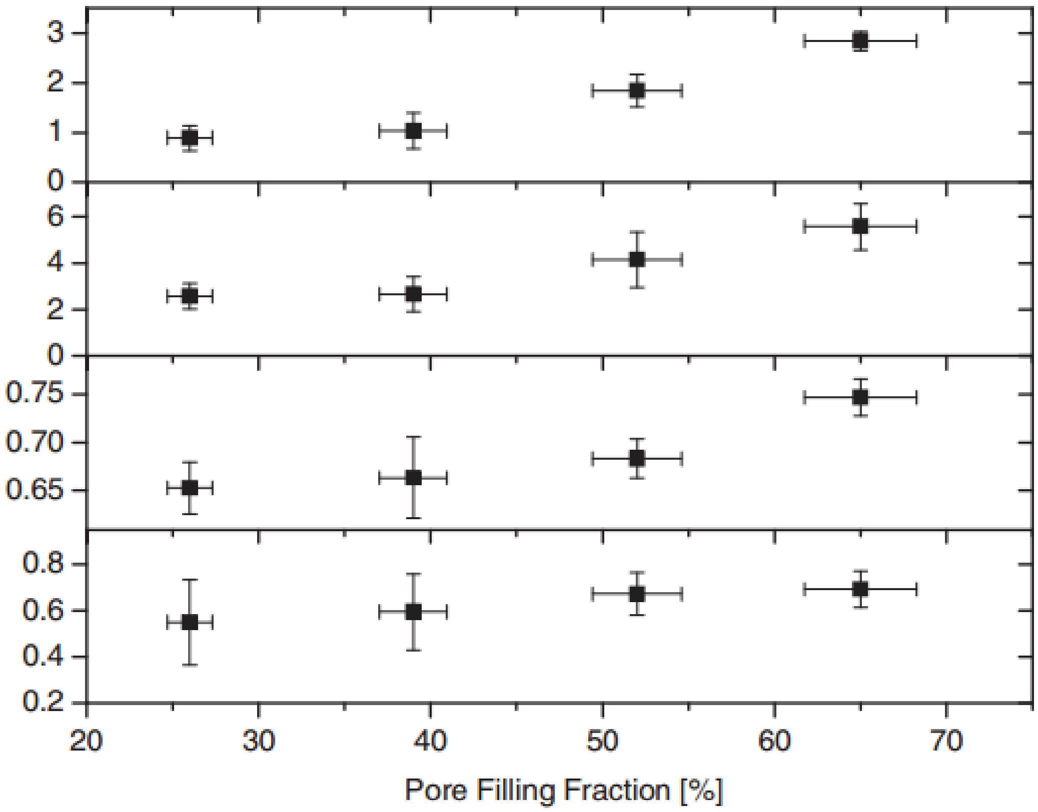

Figure 5.3 Power conversion efficiency, J_{SC}, V_{OC} and fill factor (FF) for a 2 µm thick ss-DSSC versus pore filling fraction of spiro-MeOTAD.

One approach increasing the PFF is to change the surface properties of the TiO_2 pores so that the spiro-MeOTAD will easily pass through the 'wet' surface. Using an amphiphilic dye such as C220 dye[10] or Z907 dye[8], whose structures are depicted in Figure 5.4, enhance the hydrophobicity of the TiO_2 surface, and improves the infiltration of the spiro-MeOTAD because of the strong hydrophobic-hydrophobic interaction between the chlorobenzene solution of spiro-MeOTAD and longer alky chain from the dye. Another approach to optimize the pore filling is to tune the deposition parameters of spiro-MeOTAD, such as the spin-coating rate, the concentration of spiro-MeOTAD[3] during the spin-coating process, or to explore doctor-blading instead of spin-coating[16].

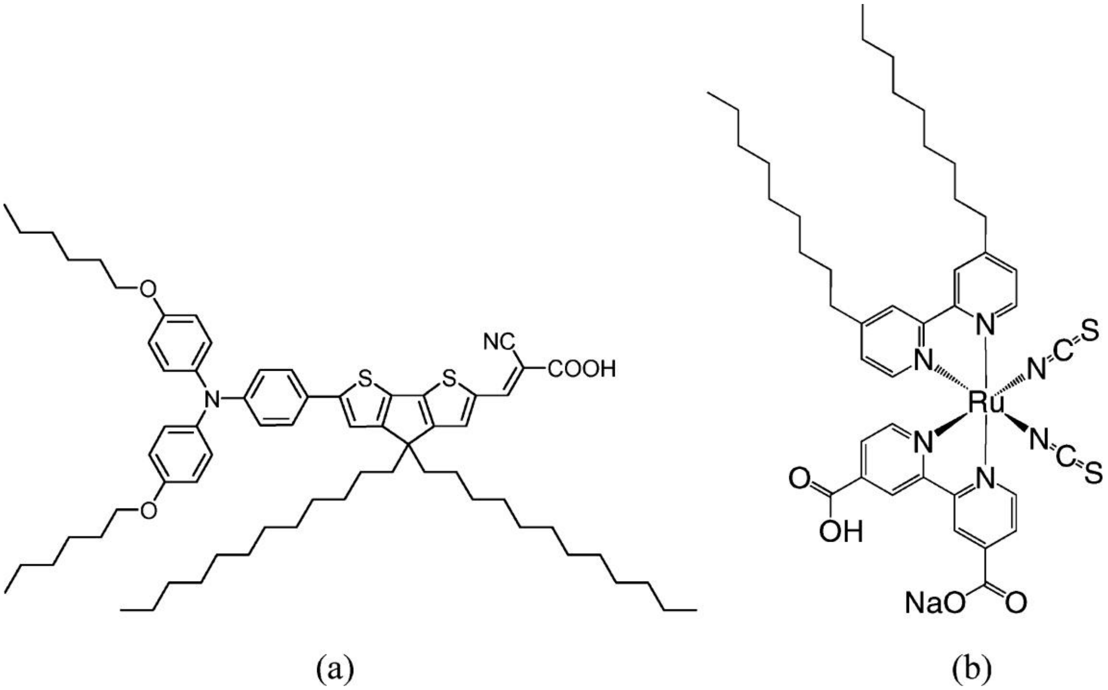

Figure 5.4 The molecular structures of C220 (a) and Z907 (b) dyes.

Very recently, it was suggested that HTMs with low melting point (T_m) and low glass transition temperature (T_g) could replace spiro-MeOTAD, as these materials would provided opportunity to increase the PFF in a melting infiltration process instead of spin-coating. Motivated by these ideas, Sellinger et al. designed new organic HTMs (AS 37 and AS 44) with low T_m and a 2 fold higher solubility which allow facile interpenetration into the TiO_2 pore structure[17]. Using a Z907 dye as the light absorber, the AS 37 and AS 44 based ss-DSSC reached efficiencies of 3%, rivaling that of conventional spiro-MeOTAD cells. Indeed, the reduced size of the HTM, its excellent solubility and low T_m and T_g, a 6 μm-thick ss-DSSC performed better than a comparable spiro-MeOTAD cell.

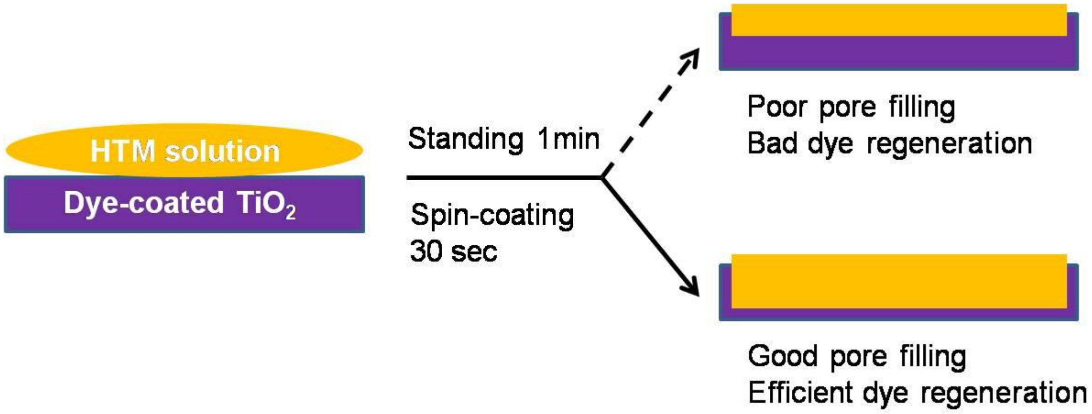

Scheme 5.1 Illustration of HTM pore-filling in ss-DSSC

In contrast to these previous methods, we present a simple heat-assisting method to induce the spiro-MeOTAD into the TiO_2pores.We obtain a marked increase in cell performance, especially the photocurrent, after the heat treatment. We attribute the improved performance to more efficient dye regeneration (scheme 5.1). This simple strategy reduces the surface tension of the HTM solution in the TiO_2 pores by elevating the temperature of both the HTM solution and deposition substrate. We calculate the PFF and conduct an SEM analysis that reveals a uniform spiro-MeOTAD thin layer coating the TiO_2.This thin layer serves as a blocking layer, preventing a short-circuit between the gold electrode and TiO_2, which can lead to charge recombination. This observation is consistent with the observed increase in open circuit voltage in the ss-DSSC after heat treatment.

5.2 Results and Discussions:

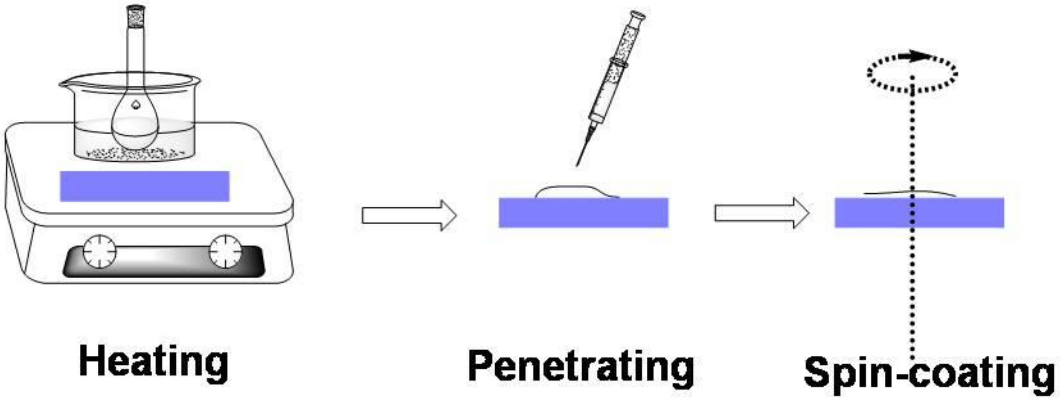

Scheme 5.2 A schematic representation of the heat-assisted procedure for the penetration of spiro-MeOTAD (chlorobenzene solution heated in flask) into the dye-coated TiO_2 substrate (blue slides) in ss-DSSC.

The ss-DSSC was assembled using the following optimized procedure[2]. Briefly, we first deposit a compact TiO_2 layer and mesoporous TiO_2 film in a soaking dye solution. After drying the soaking solution from the dye-coated TiO_2 substrate, both the substrate and spiro-MeOTAD solution are heated to 70 ℃ and the pre-heated solution is quickly applied to the warmed substrate for the spin-coating set (depicted in scheme 5.2). After the gold electrode is thermal-deposited on top of the electrolyte, the device is ready for J-V measurement. Following this heat treatment procedure on both the TiO_2 substrate and the HTM solution, we obtain ss-DSSCs with efficiencies of 1.3 %, a Jsc, of 3.4 mA/cm^2, a V_{oc} of 0.74 V, and a FF of 0.52. Without the heat treatment, we obtain cells with a typical efficiency of 0.17% and an extremely low J_{sc} of 0.66 mA/cm^2 (seen in Figure 5.5). This low current density maybe due to the small size of TiO_2 pores (Ti-Nanoxide T, purchased from Solaronix), which inhibits the spiro-MeOTAD from entering the pores. This type of TiO_2 paste had a particle size around 13 nm and typical pore sizes of 10-15 nm after sintering to the film (see Figure 5.7a). After sintering at 450 ℃, the paste reduces to aTiO_2 film with a thickness of 3-4 μm (Figure 5.7b). The typical pore size of this film was smaller than the 20-25 nm size of conventional TiO_2 films, but exhibited a very high transparency. We conjecture that the smaller particle size increases the transparency because there is less light scattering. In addition the smaller pore size increases surface are, permitting a greater density of dye molecules and hence a higher photocurrent[18]. We believe that the heat-assisting method will reduce both the viscosity and surface tension of the casting solution (Figure 5.6), leading to a more effective infiltration of the spiro-MeOTAD into the TiO_2 pores, even with the smaller pore size. Without the heat treatment, the cell has insufficient spiro-MeOTAD for dye regeneration.

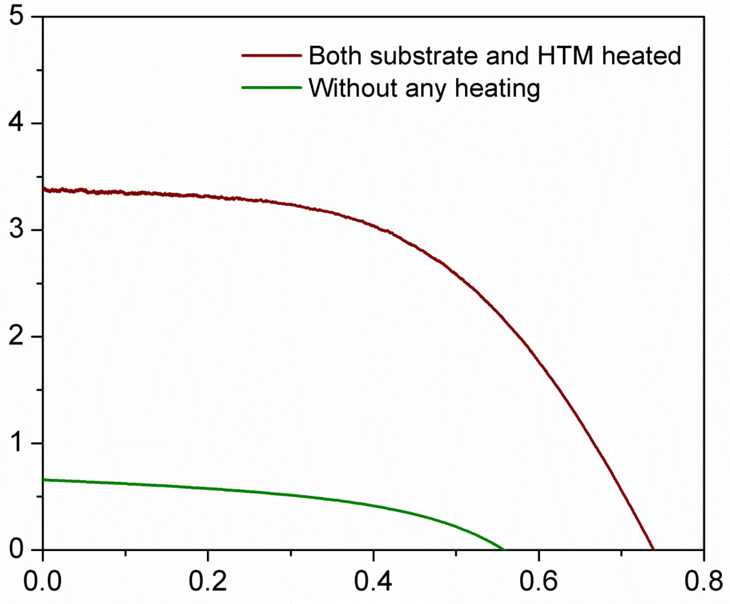

Figure 5.5 J-V curves of ss-DSSC fabricated with (red curve) and without (green curve) the heat-assisted method.

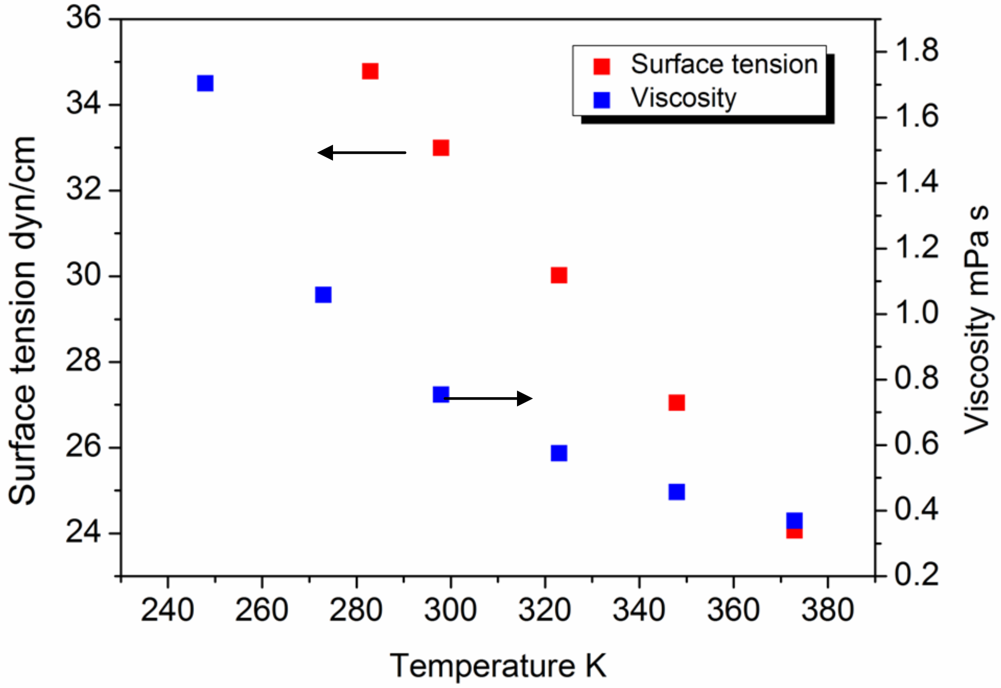

Figure 5.6 Temperature dependence of the surface tension and viscosity of chlorobenzene.

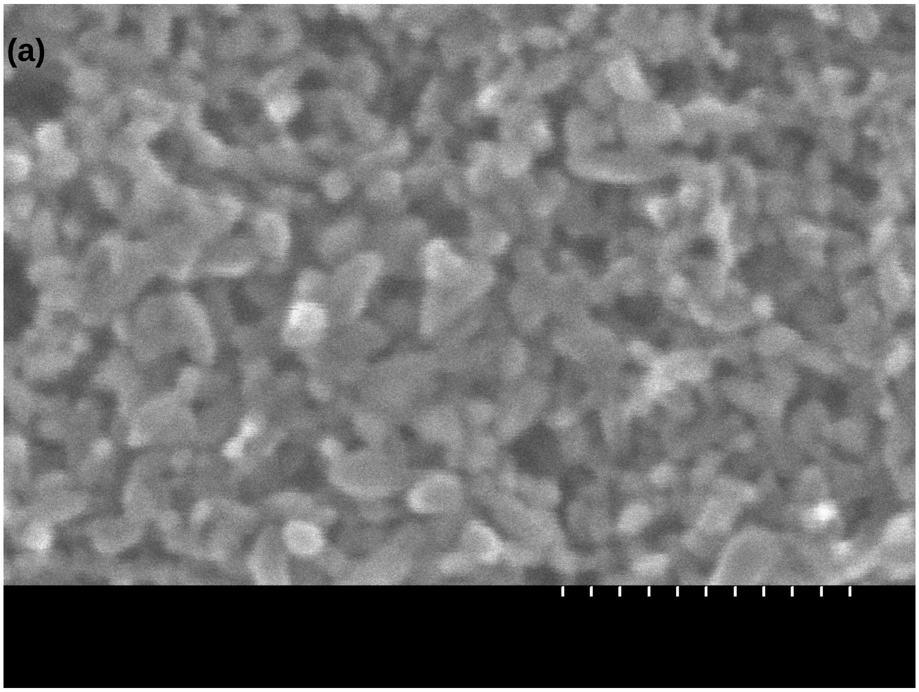

Figure 5.7 SEM image of (a) mesoporousTiO_2 (Ti-Nanoxide T) and (b) cross sectional structure of thess-DSSC

To investigate the influence of the heat treatment on the spiro-MeOTAD penetration, we first study the “wetting” behavior of the room temperature TiO_2 substrate. We drop spiro-MeOTAD solution on the substrate, and measure the dynamic contact angle as a function of temperature. With or without heating, the initial contact angle was 17° when the droplet first touched the TiO_2 surface (see Figures 5.8a and 5.8b). As the solution began to infiltrate into the pores, the contact angle decreased and quickly saturated. After only 30 seconds, the contact angle decreased to 4° with heat treatment, while without the heat treatment the contact angle saturated at 6° (see Figure 5.8c). In particular, the initial variation of the contact angle was quite rapid, requiring just 2-3 seconds, and was very sensitive to temperature. The heated solution saturated more quickly, taking a shorter time to absorb into the TiO_2 pores as compared to the non-heat treated solution. We conclude that the reduction in surface tension of the solution and viscosity (seen in Figure 5.6), is sufficient to increase the permeation of the spiro-MeOTAD into the porous TiO_2 substrate.

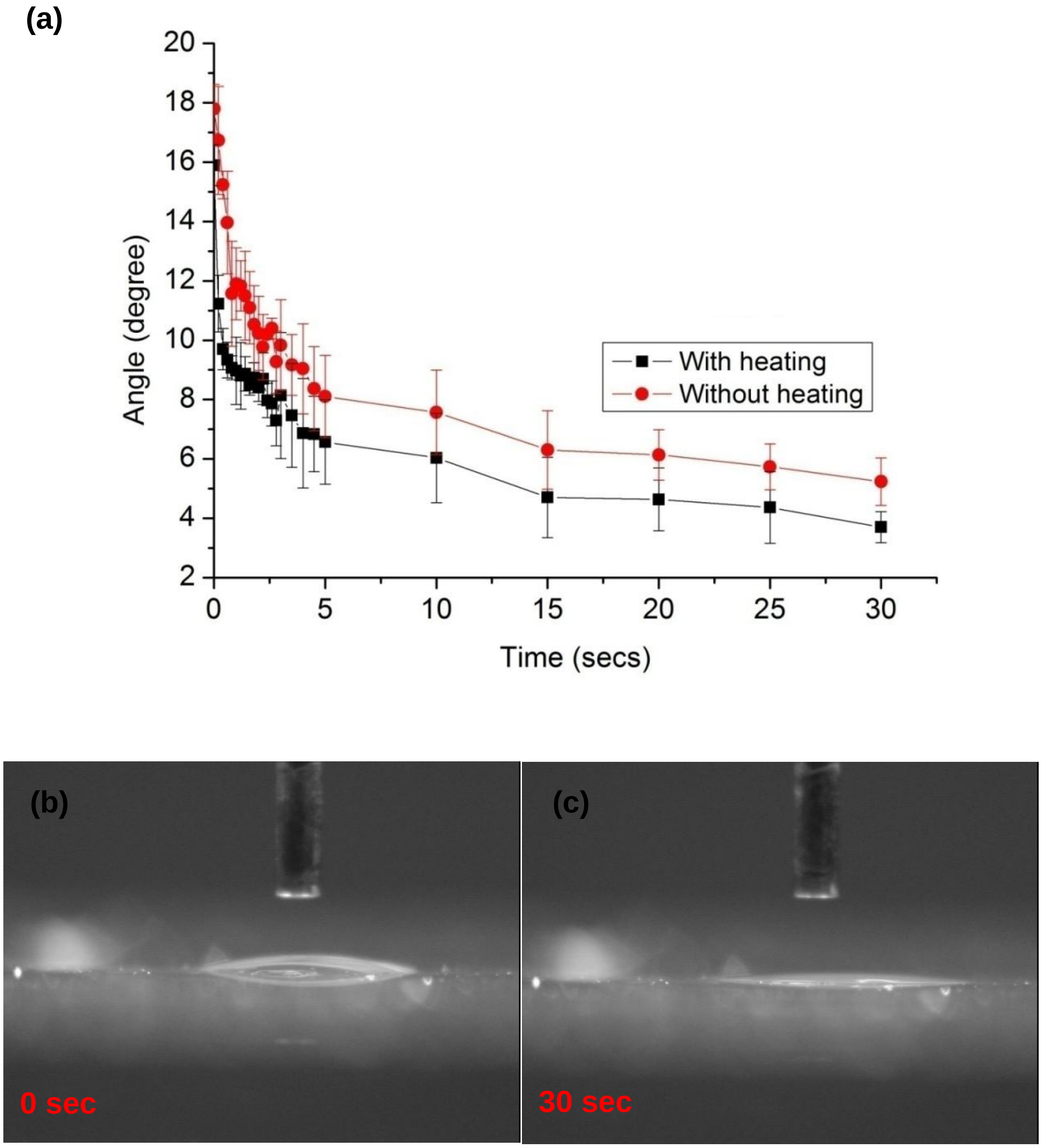

Figure 5.8 Dynamic contact angle measurements of spiro-MeOTAD solution on TiO_2 substrate with heat treatment (black) and without heat treatment (red). (a) The variation of the contact angle is monitored for the first 30 seconds after the droplet touches the TiO_2 substrate. (Inset for the first 2 seconds). (b) the initial stage t=0 s and (c) the final stage t= 30 s.

The morphology of the HTM capping layer on the outer surface of the TiO_2 also has a significant impact on the ss-DSSC performance[3,19]. A uniform capping layer minimizes the chance of short-circuit by direct contact between the TiO_2 and the gold electrode. To examine the uniformity of the HTM capping layer, we compared three different heat treatments: 1) both substrate and HTM solution heated, 2) only HTM solution heated, 3) without any heating. The concentration of HTM solution (spiro-MeOTAD in chlorobenzene) was 9 wt% and 15 wt%, respectively. The corresponding ss-DSSC performance is summarized in Figure 5.9 and Table 5.1.

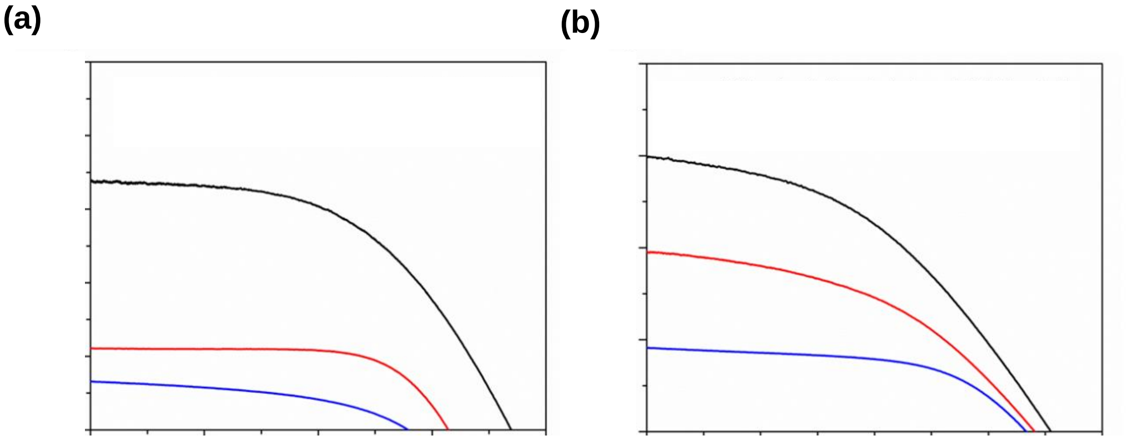

Figure 5.9 J-V curves of ss-DSSC manufactured under different heat treatments and with solution concentrations. a) 9 wt% and b) 15 wt% spiro-MeOTAD in chlorobenzene solution.

Table 5.1 Summary of ss-DSSC performance with different deposited condition.

Condition		J_{sc}(mA/cm^2)	V_{oc}(V)	FF	η(%)
9 wt%	Substrate & HTM heated	3.4	0.74	0.52	1.3
	Only HTM heated	1.1	0.63	0.69	0.48
	No heating	0.66	0.56	0.45	0.17
15 wt%	Substrate & HTM heated	3.0	0.71	0.43	0.92
	Only HTM heated	2.0	0.68	0.43	0.58
	No heating	0.91	0.67	0.56	0.34

With low concentration of HTM solution (9 wt%), the cell efficiency reached the highest value of 1.3 % (Table 5.1) when both substrate and HTM solution were heat-treated. If only the HTM solution is pre-heat but the TiO_2 substrate is left a room temperature, the resulting cell has half the efficiency with a lower J_{sc} of 1.1 mA/cm^2. When neither the solution nor the substrate is pre-heated we obtain a cell with an extremely low current and efficiency. This impact of heat-treatment upon cell performance is not found in the literature; moreover we have replicated this phenomenon in 12 different cells, thereby establishing its reproducibility.

With the scanning electron microscope (SEM), we obtained images that show the morphology of the capping layer varies with the different heat treatments. The most uniform film formed after pre-heating both the substrate and HTM solution prior to spin-coating (Figure 5.10a). When only the HTM solution is pre-heated, the capping layer exhibited a few pinholes (Figure 5.10b). Without pre-heat of either solution or substrate, there was almost no spiro-MeOTAD covering on the TiO_2 surface (Figure 5.10c). Figure 5.11, presents the results of the atomic force microscopy (AFM) imaging of the spiro-MeOTAD capping layer, confirming the results from the SEM images. In this experiment the pre-heated or non-pre-heated HTM solution was placed on the TiO_2 substrate for 60 seconds before the spin-coating, affording enough time for the HTM solution to penetrate into the pores. Because of the pre-heating of the substrate and HTM solution, the chlorobenzene solvent evaporated during the soaking period, which concentrated the HTM solution. After 60 seconds, the heated solution cooled down to room temperature but was more concentrated and viscous. The more concentrated, less viscous solution formed with the pre-heated sample form a more uniform capping layer even with only 9 % spiro-MeOTAD solution. In contrast, the un-heated solution with low concentration of HTM polymer and high viscosity could was unable to generate a capping layer at all.

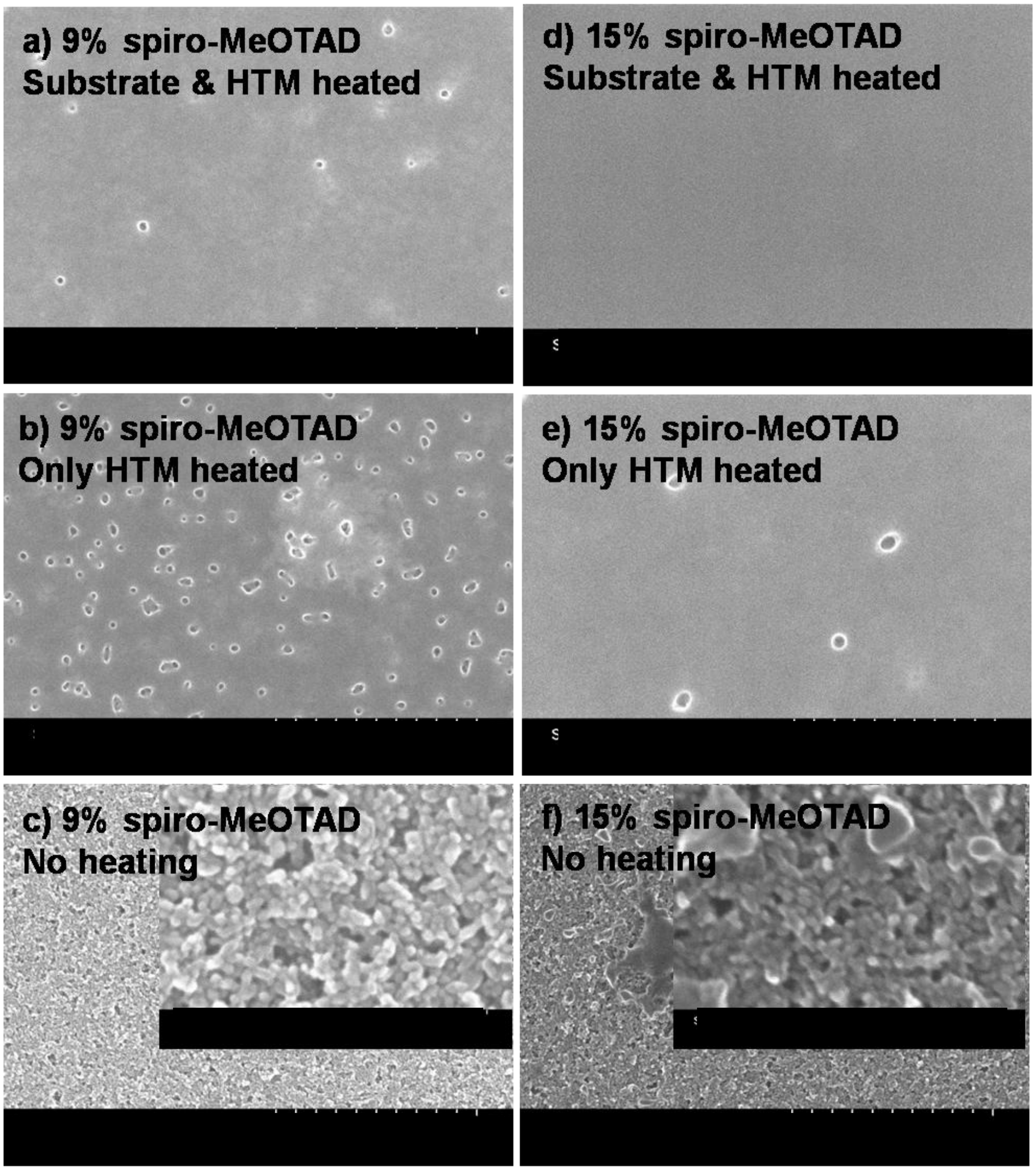

Figure 5.10 Morphology of spiro-MeOTAD capping layer deposited on TiO_2 film after spin-coating under various conditions. 9 wt% spiro-MeOTAD used for spin-coating with a) both substrate and HTM solution pre-heated; b) only HTM solution pre-heated; and c) no pre-heating. 15 wt% spiro-MeOTAD used for spin-coating with d) both substrate and HTM solution pre-heated; e) only HTM solution pre-heated; and f) no pre-heating.

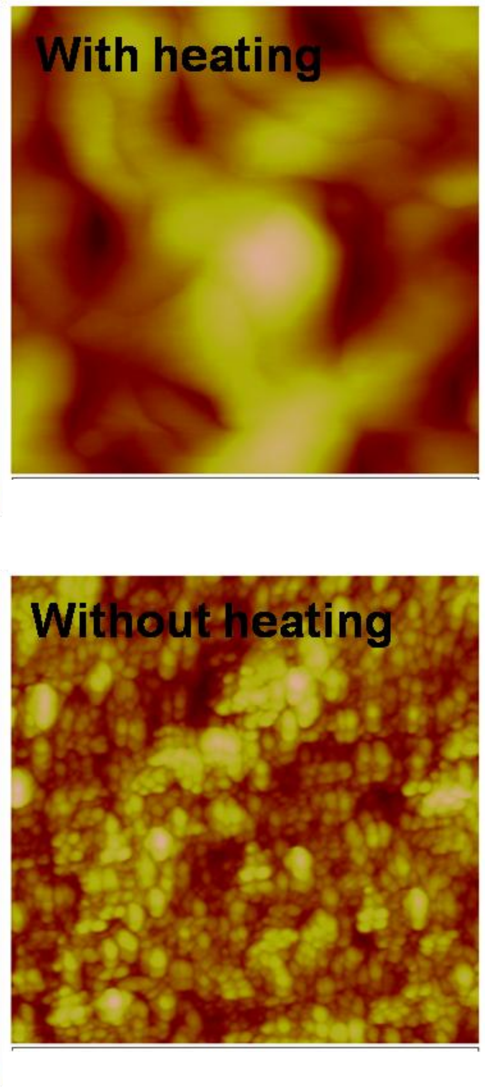

Figure 5.11 AFM study of spiro-MeOTAD capping layer on TiO_2. (Up: both substrate and HTM solution pre- heated; Bottom: without any pre-heating)

To maximize the infiltration of spiro-MeOTAD into the TiO_2 substrate, we also tried spin-coating a high concentrated HTM solution with 15 wt% spiro-MeOTAD in chlorobenzene. We observed the same morphology these of 9 wt%

spiro-MeOTAD (Figure 5.10). The high concentration of spiro-MeOTAD yielded a more viscose solution, and under equivalent pre-heating conditions the capping layer formed from the high concentration solution displayed even fewer defects than that formed from the low concentration solution. However, the improved capping layer did not improve cell performance, but generated a noticeable reduction in the FF. The FF is strongly influenced by the cell's bulk resistance and we conclude that a thick, uniform capping layer leads to a larger internal resistance. To confirm this, we monitored the thickness of capping layer for different deposited condition via both SEM imaging and profilometer. The results are summarized in the Table 5.2. Without any heating, both the 9% and 15% HTM solution could not form any capping layer covering on the TiO_2. This observation is consistent with previous morphology study presented in Figure 5.10c and Figure 5.10f. When pre-heating only the HTM solution, the 9% HTM solution produced a 130 nm thick capping layer while the 15% HTM solution produced a 680 nm thick capping layer. With pre-heating of both the substrate and the HTM solution the 9% HTM solution produced a 340 nm thick capping layer while the 15% HTM solution yielded a 950 nm thick layer. The 340 nm thick HTM capping layer gave an optimal trade-off between the internal resistance and short-circuit insulation, providing the optimal performance.

Table 5.2 Summary of capping layer thickness under various deposited condition

9% spiro-MeOTAD	capping layer thickness(nm)	15% spiro-MeOTAD	capping layer thickness(nm)
both substrate and HTM heated	340 nm	both substrate and HTM heated	950 nm
only HTM heated	130 nm	only HTM heated	680 nm
without any heating	N.A	without any heating	N.A

Several studies[2,3] have related the PFF to the dye regeneration and cell performance in ss-DSSC. They approximate the PFF from the following formula:

$$PFF = \frac{V_{spiro(TiO_2)}}{V_{TiO_2} \times \Phi_{TiO_2}} = \frac{V_{spiro(TiO_2)}}{A \times t_{TiO_2} \times \Phi_{TiO_2}} \qquad （1）$$

Where Φ_{TiO2}, the porosity of mesoporous structure, is approximately 60%, $t_{spiro(cap)}$ is the thickness of spiro-MeOTAD capping layer, A denotes the spin-coated area, t_{TiO2} denotes the thickness of the TiO_2, about 4 μm, while $V_{spiro(TiO2)}$, the volume of spiro-MeOTAD in TiO_2 pores, is given by the formula:

$$V_{spiro(TiO_2)} = \frac{m_{spiro(TiO_2)}}{\rho_{spiro}} = \frac{m_{total} - m_{spiro(cap)}}{\rho_{spiro}} \qquad （2）$$

in which ρ_{spiro} denotes the density of the spiro-MeOTAD[5], approximately 1.02g/cm^3. Here the total weight, m_{total}, of spiro-MeOTAD is proportional to the absorbance, Abs_{spiro}, of the spiro-MeOTAD:

$$m_{total} \propto Abs_{spiro} \qquad (3)$$

while the weight of the spiro-MeOTAD in the capping layer is given by:

$$m_{spiro(cap)} = \rho_{spiro} \times V_{spiro(cap)} = \rho_{spiro} \times A \times t_{spiro(cap)} \qquad (4)$$

Table 5.3 Capping layer thickness, PFF and cell performance from under the various deposited conditions. The PFF is estimated from equations (1)-(4).

	9% spiro-MeOTAD		15% spiro-MeOTAD	
Condition	Substrate & HTM heated	No heating	Substrate & HTM heated	No heating
Thickness (nm)	340	N.A.	950	N.A.
PFF (%)	86%	48%	77%	64%
J_{SC}(mA/cm^2)	3.4	0.66	3.0	0.91
η(%)	1.3	0.17	0.92	0.34

We apply the equations (1)-(4) to determine the PFF for the cases of a uniform capping layer or no capping layer. The results are summarized in Table 5.3. For cells manufactured with pre-heating of only the HTM solution, the volume of the capping area was hard to estimate because of the pin-holes. We observe a strong, positive correlation between the PFF and the cell efficiency. The cell with the 86% PFF, has the highest current and efficiency, despite the use of a lower concentration of HTM in the solution. The high concentration HTM solution achieved only a 77% PFF and a lower cell efficiency. However, cells assembled without heat treatment, weather at low or high concentration of HTM solution, had low PFF. This analysis supports our thesis that heat treatment leads to superior infiltration of spiro-MeOTAD into the TiO_2 substrate, yielding a higher PFF and higher overall cell performance, even at lower HMT loads.

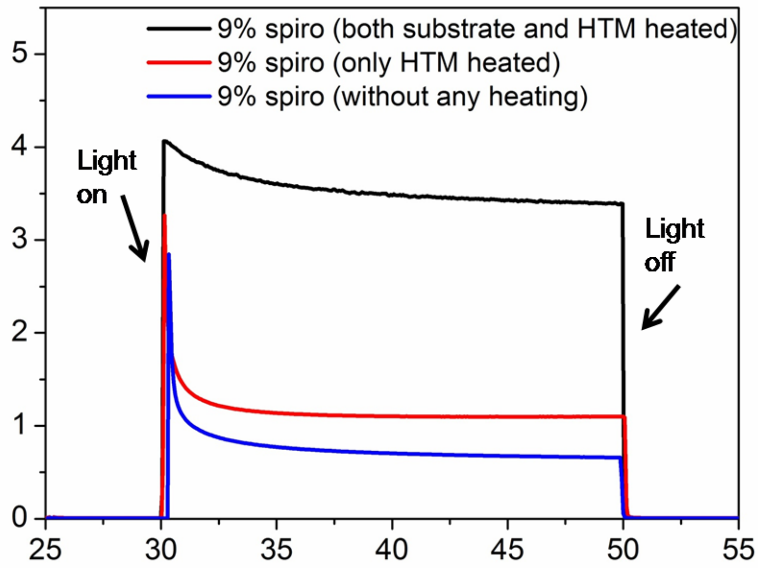

Figure 5.12 Plots of current transients of ss-DSSCs employing different heat treatments with 9 wt% spiro-MeOTAD solution under 1 sun illumination.

An ‘over-shooting’ of photocurrent was also observed in Figure 5.12. With only HTM heated or without any heating, the steady-state current density was significantly lower than the initial-state current density. We attributed it to incomplete poor filling by the spiro-MeOTAD, and some dye molecules could only 'fire' once as they were not getting regenerate effectively. This similar mass transport problem have been reported previously[20,21]. We’ve also thought this ‘over-shooting’ was due to ‘short-circuit’ because of less uniform capping layer. However, if both spiro-MeOTAD solution and substrate had been heated, this phenomenon turned attenuated (black curve in Figure 5.12). We concluded that our heating treatment could effectively eliminate this sort of instantaneous current density. Pore filling of hole conductor in TiO_2 is one of the most dominant factor to cell performance.

Conclusion:

In this chapter, we presented a new, simple method to effectively infiltrate spiro-MeOTAD into the TiO_2 porous substrate. Before spin-coating the HTM solution, both the TiO_2 substrate and the HTM solution are pre-heated, reducing the surface tension and viscosity of casting solution, while concentrating the HTM polymer by evaporating a portion of the solvent. Following the drop casting of the hot solution on the warm substrate, we observed the formation of a more uniform capping layer on the outer surface of the TiO_2 substrate as compared to the capping layer formed from the process with either a partial pre-heating or no heat treatment. An analysis of in-situ performance data indicates that a uniform capping layer minimizes the current loss due to direct contact between counter electrode and photoanode, TiO_2.A low concentration HTM solution (9 wt% spiro-MeOTAD) applying in this study formed a thinner capping layer than the high concentration solution (15 wt% spiro-MeOTAD). The thinner capping layer offers a lower internal resistance while producing a higher FF. For independent corroboration, the PFF was determined from ex-situ data, which confirmed that the highest PFF was achieved from the heat-treated solution with a moderate amount of HTM. We conclude that the heat treatment procedure yields the highest PFF with a thin and uniform capping layer, at a relatively low level of HTM concentration. Also by conducting current transient measurements, we confirm that heating treatment enable to eliminate ‘over-shooting’ of photocurrent from mass transport problem. The heat treatment strategy is a simple, cost effective means to obtain an optimized distribution of the HTM within the TiO_2 substrate. For future work we will investigate whether melting infiltration can replace spin-coating as a means to infiltrate a low T_m solid electrolyte in the absence of liquid solvent.

Experimental:

5.4.1 Materials

Fluorine doped Tin Oxide (FTO) Glass purchased from Hartford was pretreated by Alconox, distilled water, acetone and UV-ozone before use. Spiro-MeOTAD was purchased from Lumtech. TiO_2 paste (Ti-Nanoxide T) was from Solaronix. Gold used as evaporation source for counter electrode was from Kurt J. Lesker. All other chemicals were purchased from Sigma Aldrich and were used as receive unless mentioned otherwise.

5.4.2 Instruments

The capping layer on TiO_2wasimaged by a Hitachi S-4700 II field-emission scanning electron microscope (FESEM). The cross-sectional structure of solar cell was determined by Carl Zeiss Auriga Dual Column FIB SEM. The morphology of capping layer was captured by Veeco Dimension 3100 scanning probe microscope. Contact angles were measured using a VCA 2000 Video Contact Angle Surface Analysis system. Absorption spectra were obtained from Varian Carey Model 50 UV-Vis Spectrophotometer. Current-voltage measurements and open circuit voltage decay measurements of ss-DSSC were performed using a Xe Arc Lamp and CHI-650D Electrochemical work station. An AM 1.5 solar filter and neutral density filter were used to simulate sunlight at 100 mW cm^{-2}. A mask with an area of 0.25 cm^2 was used.

3.4.3 Solar cell fabrication and preparation

Devices of ss-DSSC were fabricated according to a procedure[2]. Briefly, a pre-cleaned FTO glass was put on a hot plate with a temperature of 500°C for 30 min before any deposition. A 200nm thickness of TiO_2 compact layer on FTO was formed by home-made spray-pyrolysis set-up using air as carrier gas and titanium di-isopropoxidebis (acetylacetonate) as precursor. A 2.5 µm thickness of mesoporous TiO_2 film was deposited by doctor-blading TiO_2 pastes with scotch tape as spacer. The thickness was measured by profilometer and confirmed by cross-section SEM image. After baking the TiO_2 paste with a programmable heating procedure up to 450°C, we let the substrate cooling down to 80 °C before soaking into a 0.3mM N3 dye ethanol solution. The dye soaking took about 16 hours at least, followed by rinsing with ethanol and acetonitrile. A heated chlorobenzene solution of spiro-MeOTAD was used for spin-coating on heated dye-coated TiO_2 substrates. The concentration of hole conductors was 9 wt% or 15 wt% in total with additives of lithium bis(trifluoromethylsulfonyl)imide (LiTFSI) and 4-tert butylpyridine (4-tBP). A 36 µL electrolyte solution firstly stood on the substrate for one minute and then was spin-coated with 2000 rpm for 30 seconds in air. The cell was stored under dark overnight before depositing the gold electrode. A 30 nm thickness of gold was applied by thermal evaporation as back contact.

REFERENCES

REFERENCES

(1) Schmidt-Mende, L.; Gratzel, M.: TiO2 pore-filling and its effect on the efficiency of solid-state dye-sensitized solar cells. *Thin Solid Films* **2006**, *500*, 296-301.

(2) Snaith, H. J.; Humphry-Baker, R.; Chen, P.; Cesar, I.; Zakeeruddin, S. M.; Gratzel, M.: Charge collection and pore filling in solid-state dye-sensitized solar cells. *Nanotechnology* **2008**, *19*.

(3) Ding, I. K.; Tetreault, N.; Brillet, J.; Hardin, B. E.; Smith, E. H.; Rosenthal, S. J.; Sauvage, F.; Gratzel, M.; McGehee, M. D.: Pore-Filling of Spiro-OMeTAD in Solid-State Dye Sensitized Solar Cells: Quantification, Mechanism, and Consequences for Device Performance. *Adv Funct Mater* **2009**, *19*, 2431-2436.

(4) Melas-Kyriazi, J.; Ding, I. K.; Marchioro, A.; Punzi, A.; Hardin, B. E.; Burkhard, G. F.; Tetreault, N.; Gratzel, M.; Moser, J. E.; McGehee, M. D.: The Effect of Hole Transport Material Pore Filling on Photovoltaic Performance in Solid-State Dye-Sensitized Solar Cells. *Adv Energy Mater* **2011**, *1*, 407-414.

(5) Docampo, P.; Hey, A.; Guldin, S.; Gunning, R.; Steiner, U.; Snaith, H. J.: Pore Filling of Spiro-OMeTAD in Solid-State Dye-Sensitized Solar Cells Determined Via Optical Reflectometry. *Adv Funct Mater* **2012**, *22*, 5010-5019.

(6) Cappel, U. B.; Gibson, E. A.; Hagfeldt, A.; Boschloo, G.: Dye Regeneration by Spiro-MeOTAD in Solid State Dye-Sensitized Solar Cells Studied by Photoinduced Absorption Spectroscopy and Spectroelectrochemistry. *J Phys Chem C* **2009**, *113*, 6275-6281.

(7) Bach, U.; Lupo, D.; Comte, P.; Moser, J. E.; Weissortel, F.; Salbeck, J.; Spreitzer, H.; Gratzel, M.: Solid-state dye-sensitized mesoporous TiO2 solar cells with high photon-to-electron conversion efficiencies. *Nature* **1998**, *395*, 583-585.

(8) Schmidt-Mende, L.; Kroeze, J. E.; Durrant, J. R.; Nazeeruddin, M. K.; Gratzel, M.: Effect of hydrocarbon chain length of amphiphilic ruthenium dyes on solid-state dye-sensitized photovoltaics. *Nano Lett* **2005**, *5*, 1315-1320.

(9) Schmidt-Mende, L.; Zakeeruddin, S. M.; Gratzel, M.: Efficiency improvement in solid-state-dye-sensitized photovoltaics with an amphiphilic Ruthenium-dye. *Appl Phys Lett* **2005**, *86*.

(10) Cai, N.; Moon, S. J.; Cevey-Ha, L.; Moehl, T.; Humphry-Baker, R.; Wang, P.; Zakeeruddin, S. M.; Gratzel, M.: An Organic D-pi-A Dye for Record Efficiency Solid-State Sensitized Heterojunction Solar Cells. *Nano Lett* **2011**, *11*, 1452-1456.

(11) Burschka, J.; Dualeh, A.; Kessler, F.; Baranoff, E.; Cevey-Ha, N. L.; Yi, C. Y.; Nazeeruddin, M. K.; Gratzel, M.: Tris(2-(1H-pyrazol-1-yl)pyridine)cobalt(III) as p-Type Dopant for Organic Semiconductors and Its Application in Highly Efficient Solid-State Dye-Sensitized Solar Cells. *J Am Chem Soc* **2011**, *133*, 18042-18045.

(12) Haque, S. A.; Park, T.; Xu, C.; Koops, S.; Schulte, N.; Potter, R. J.; Holmes, A. B.; Durrant, J. R.: Interface engineering for solid-state dye-sensitized nanocrystalline solar cells: The use of ion-solvating hole-transporting polymers. *Adv Funct Mater* **2004**, *14*, 435-440.

(13) Lechmann, M. C.; Kessler, D.; Gutmann, J. S.: Functional Templates for Hybrid Materials with Orthogonal Functionality. *Langmuir* **2009**, *25*, 10202-10208.

(14) Kroeze, J. E.; Hirata, N.; Schmidt-Mende, L.; Orizu, C.; Ogier, S. D.; Carr, K.; Gratzel, M.; Durrant, J. R.: Parameters influencing charge separation in solid-state dye-sensitized solar cells using novel hole conductors. *Adv Funct Mater* **2006**, *16*, 1832-1838.

(15) Olson, C.; Veldman, D.; Bakker, K.; Lenzmann, F.: Characterization of the Pore Filling of Solid State Dye Sensitized Solar Cells with Photoinduced Absorption Spectroscopy. *International Journal of Photoenergy* **2011**, *2011*.

(16) Ding, I. K.; Melas-Kyriazi, J.; Cevey-Ha, N. L.; Chittibabu, K. G.; Zakeeruddin, S. M.; Gratzel, M.; McGehee, M. D.: Deposition of hole-transport materials in solid-state dye-sensitized solar cells by doctor-blading. *Org Electron* **2010**, *11*, 1217-1222.

(17) Leijtens, T.; Ding, I. K.; Giovenzana, T.; Bloking, J. T.; McGehee, M. D.; Sellinger, A.: Hole Transport Materials with Low Glass Transition Temperatures and High Solubility for Application in Solid-State Dye-Sensitized Solar Cells. *Acs Nano* **2012**, *6*, 1455-1462.

(18) Jeong, N. C.; Farha, O. K.; Hupp, J. T.: A Convenient Route to High Area, Nanoparticulate TiO2 Photoelectrodes Suitable for High-Efficiency Energy Conversion in Dye-Sensitized Solar Cells. *Langmuir* **2011**, *27*, 1996-1999.

(19) Kim, H. S.; Lee, C. R.; Jang, I. H.; Kang, W.; Park, N. G.: Effect of Overlayer Thickness of Hole Transport Material on Photovoltaic Performance in Solid-Sate Dye-Sensitized Solar Cell. *B Korean Chem Soc* **2012**, *33*, 670-674.

(20) Nelson, J. J.; Amick, T. J.; Elliott, C. M.: Mass Transport of Polypyridyl Cobalt Complexes in Dye-Sensitized Solar Cells with Mesoporous TiO2 Photoanodes. *J Phys Chem C* **2008**, *112*, 18255-18263.

(21) Klahr, B. M.; Hamann, T. W.: Performance Enhancement and Limitations of Cobalt Bipyridyl Redox Shuttles in Dye-Sensitized Solar Cells. *J Phys Chem C* **2009**, *113*, 14040-14045.

Chapter 6: Summary and Future work

6.1 Summary

Dye sensitized solar cell (DSSC) is a new photovoltaic technology with potential to economically harvest and efficient converting photons to electricity. Compared to liquid-based DSSC, A full solid state dye sensitized solar cell (ss-DSSC) enables to avoid solvent leaking and evaporation during cell fabrication and operation, which will effectively elongate the cell life time.

In this dissertation, we describe how to boost light absorption, enhance the cell fill factor and increase pore filling fraction of hole conductor.

Firstly, we found that the cell performance improved after the ss-DSSC was illuminated under open-circuit conditions. After twenty minute short-circuit illumination the FF increased 36%, resulting in a 25% increasing of cell efficiency. We deduced that LiTFSI triggers a photo-oxidation of spiro-MeOTAD under short wave length light, and that dye is required to trigger the oxidation under longer wave-length light. We also inferred that the counter anion, TFSI serves to stabilize the spiro-MeOTAD$^+$.

Secondly, we successfully grafted poly (triphenylamine) onto the surface of silica nanoparticles. The solar cell of an electrolyte comprised of hole-conducting silica/polymer nanocomposite and spiro-MeOTAD was investigated. We assembled an ss-DSSC using only half of the typical load of spiro-MeOTAD, which achieved a power conversion efficiency higher than a pure spiro-MeOTAD-based ss-DSSC with a 26% improvement in photocurrent. We present IPCE and absorption data which supports our thesis that the enhanced photo-current is due to the back-scattering of light from the capping layer formed from the silica/polymer nanoparticles.

Eventually, we used heat-assisted technique effectively infiltrate spiro-MeOTAD into the TiO_2 porous substrate. We conclude that the heat treatment procedure yields the highest pore filling fraction with a thin and uniform capping layer, at a relatively low level of HTM concentration. Also by conducting current transient measurements, we confirm that heating treatment enable to eliminate ‘over-shooting’ of photocurrent from mass transport problem.

6.2 Future work

At the moment this thesis is being finished, one new world-record efficiency for ss-DSSC has been over 12%[1]. This is still below the desired level around 15%-20% efficiency required for industry manufacturing. The efficiency of ss-DSSC suffered from complete pore filling and expense of hole conductor.

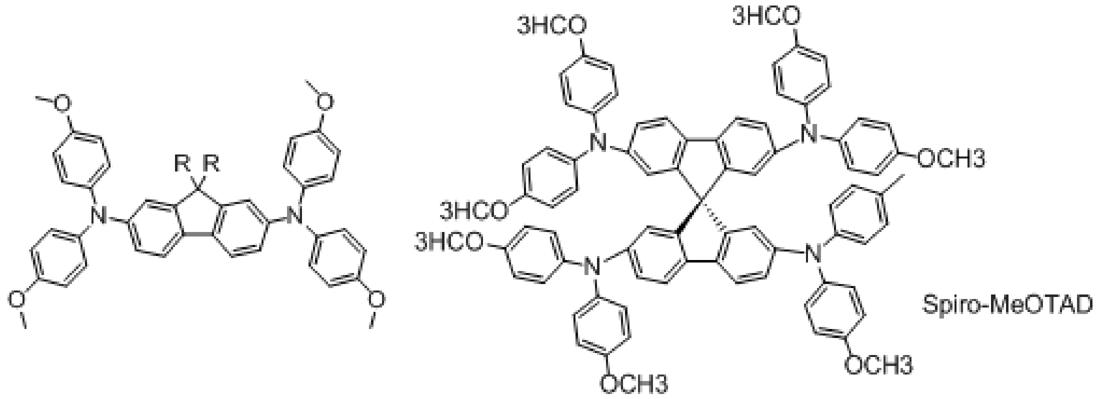

Figure 6.1 New class of hole conductors (Left) and Spiro-MeOTAD (Right).

Spiro-MeOTAD (Figure 6.1 right) is expensive and difficult to introduce into mesoporous TiO_2 because of its higher melting point. So far, spin-coating has been the only effective way for applying the electrolyte, which waste too much material and lead an incomplete penetration. In our group, we start to look for a low melting and low glass transition temperature hole conductor and then using melting infiltration instead of spin-coating. McGehee's group[2] already tried to cut half of Spiro-MeOTAD tailed with alky-chain, but still the materials cannot reach the requirements for melting infiltration. We synthesized new hole conductor by adding branched alky chain or longer chain (Fig 6.1, Left) to low the T_m and T_g. The electrochemical, photophysical properties are similar as Spiro-MeOTAD with an extremely lower Tm and T_g summarized in Table 6.1. We started to use novel hole conductor to make solar cell. The efficiency cannot compete with

Spiro-MeOTAD so far and need to optimize its performance with varied condition. Especially, improving the hole mobility of new materials is the key.

Table 6.1 Summary of electrochemical, photophysical and thermal properties of the hole conductors

R group	T_m	T_g	uv-vis (max)	HOMO (eV)	LUMO (eV)	Eg (eV)
Hexyl	107°C	41°C	392nm	-4.97	-2.03	2.94
n-octyl	90°C	26°C	393nm	-4.96	-2.02	2.94
2-ethyl hexyl	N.A	20°C	385nm	-4.95	-1.96	2.99
Decyl	74°C	13°C	393nm	-4.98	-2.04	2.94
Dodecyl	58°C	2°C	392nm	-4.99	-2.05	2.94
SpiroMeOTAD	245°C	123°C	392nm	-5.03	-2.1	2.93

REFERENCES

REFERENCES

(1) Noh, J. H.; Im, S. H.; Heo, J. H.; Mandal, T. N.; Seok, S. I.: Chemical Management for Colorful, Efficient, and Stable Inorganic–Organic Hybrid Nanostructured Solar Cells. *Nano Lett* **2013**, *13*, 1764-1769.

(2) Leijtens, T.; Ding, I. K.; Giovenzana, T.; Bloking, J. T.; McGehee, M. D.; Sellinger, A.: Hole Transport Materials with Low Glass Transition Temperatures and High Solubility for Application in Solid-State Dye-Sensitized Solar Cells. *Acs Nano* **2012**, *6*, 1455-1462.